

# Identifying Reaction Pathways and their Environments

Methods and Applications

**Maronsson, Jon Bergmann**

*Publication date:*
2012

*Document Version*
Publisher's PDF, also known as Version of record

# Identifying Reaction Pathways and their Environments

Methods and Applications

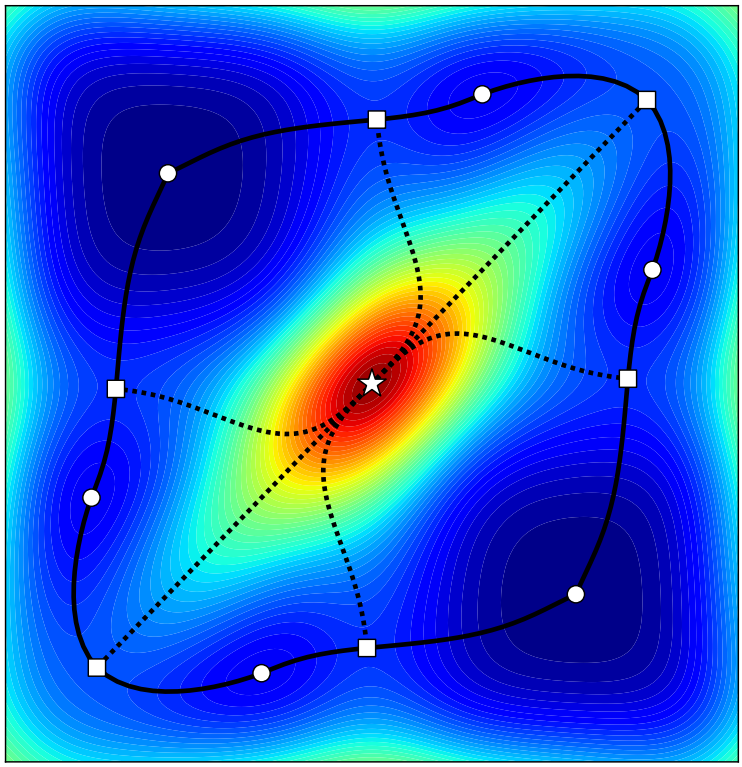

by

**Jón Bergmann Maronsson**

# Preface

This thesis is submitted in candidacy for the Ph.D. degree from the Technical University of Denmark (DTU). The work was been carried out between November 2008 and February 2012 at the Risø DTU campus, formerly the Risø National Laboratory for Sustainable Energy, DTU; the Center for Atomic-scale Materias Design (CAMD) and with external stays at the Science Institute of the University of Iceland. The project was supervised by Senior Scientist Tejs Vegge, Head of Section at the Department of Energy Conversion and Storage at the Technical University of Denmark and co-supervised by Professor Hannes Jónsson, Vice-Director of the Chemistry Division of the Science Institute of the University of Iceland. The work was financially supported by DTU and CAMD, as well as the Nordic Center of Excellence on Hydrogen Storage Materials, the European Graduate School for Sustainable Energy Technologies - The Molecular Approach and Catalysis for Sustainable Energy (CASE).

At the end of my Ph.D. project, I would like to express my thanks to the many people who made my project possible and my stay in Denmark an enjoyable one.

First of all are my supervisors, Tejs Vegge and Hannes Jónsson. Tejs' ever positive attitude, always seeing the positive side in all situations served as an incredible inspiration to me both with regards to the project and life in general. Every meeting of ours would leave me in a better place. Hannes' involvement was essential to the project. He is such a fountain of knowledge with regards to all aspects of my project. I enjoyed our discussion of the sciences tremendously.

Then come my co-workers at DTU and Risø who are literally too many to appropriately thank each one. The members of Tejs Vegge's group who have come and gone. My office buddies at DTU and those down the hall. I thank you all for the interesting and entertaining discussions throughout my stay. My trusty team of proofreaders and fellow group members warrant special thanks: Jakob, Steen, Jón Steinar and Peter. Cake will be served.

Special thanks go to my lunch buddy and right-hand man Elvar and his posse of Icelanders. As well as to Daði for introducing me to the cinematic pleasures of The Room. Dúndri, Bobbý, Hulda, Óli, Habbý, Biggi, KM&P, Tim, Macho, Little Billy and Yury all made significant efforts to keep my sanity intact. My friends, parents, grandmothers and seemingly endless amount of siblings have a special place in my heart for tolerating long bouts of my stays abroad.

And finally my aptly named buddy in chemistry and life, Ester, I love you!

Kgs. Lyngby, Denmark, February 29th 2012,

*Jón Bergmann Maronsson*

# Abstract

Finding the mechanisms and estimating the rate of chemical reactions is an essential part of modern research of atomic scale systems. In this thesis, the application of well established methods for reaction rates and paths to important systems for hydrogen storage is considered before developing extensions to further identify the reaction environment for a more accurate rate.

Complex borohydrides are materials of high hydrogen storage capacity and high thermodynamic stability (too high for hydrogen storage). In an effort to gain insight into the structural transitions of two such materials, $Ca(BH_4)_2$ and $Mg(BH_4)_2$, experiments on low temperature rotational dynamics were performed. The work presented here revolved around assisting in the data analysis by performing density functional theory calculations on the possible dynamical events. For the $Mg(BH_4)_2$, in good agreement with the experiments, $C_2$-type rotations occur at lower temperature than $C_3$-type rotations and approximately 15% of the $BH_4$ units activate at a lower temperature than the rest. For the $Ca(BH_4)_2$, in addition to the rotational dynamics, an unidentified event was detected which, according to the calculations was most likely due to $H_2$-interstitial defects. In good agreement with the experiments, $C_3$-type rotations activate at lower temperature than $C_2$-type rotations.

In order to investigate the environment of reaction pathways, a method for finding the ridge between first order saddle points on a multidimensional surface was developed. Information about the ridge can be used to test the validity of the harmonic approximation to transition state theory for reaction rates, in particular to verify that second order saddle points - maxima along the ridge - are high enough compared to the first order saddle points. Furthermore, corrections to the harmonic approximation can be estimated by direct evaluation of the configuration integral along the ridge. New minima along the ridge can also be identified during the path optimisation, thereby revealing additional transition mechanisms. The method is based on modifying the gradient of a set of points along a path connecting the saddle points to iteratively converge to the ridge. At each iteration during the optimisation, the gradient is inverted along an unstable eigenmode perpendicular to the path, locally mapping the ridge to a minimum energy path which can be located using various techniques. The method was applied to Al adatom diffusion on the Al(100) surface to find the ridge between 2-, 3- and 4-atom concerted displacement and hop mechanisms for diffusion. Significant corrections were offered for the 3- and 4-atom concerted displacements. The method offers a simple-to-use way to check the validity of reaction rates but has the potential to offer more accurate rates on its own by representing the transition state with the ridge.

# Resumé

Forståelse af reaktionshastigheder er en essentiel del af moderne forskning på atomar skala. I denne afhandling beskrives anvendelsen af veletablerede metoder til beskrivelse af vigtige hydrogenlagrings-systemer. Herefter videreudvikles metoderne for at kunne opnå en bedre beskrivelse af reaktionsvejsomgivelserne, for herigennem at bestemme reaktionshastigheden med større nøjagtighed.

Komplekse borohydrider er materialer med en høj hydrogenlagrings-kapacitet og er yderligere meget termodynamisk stabile (for stabile til hydrogen lagring). For at få bedre indsigt i de strukturelle overgange i to sådanne materialer, $Ca(BH_4)_2$ og $Mg(BH_4)_2$, blev der udført lav-temperatur rotationsdynamik eksperimenter. Arbejdet der præsenteres her omhandler assistance i forbindelse med dataanalyse, ved hjælp af tæthedsfunktionalteori-beregninger, på de mulige dynamiske hændelser. For $Mg(BH_4)_2$, var der god overensstemmelse med eksperimenter. $C_2$-type rotationer observeres ved lavere temperaturer end $C_3$-type rotationer og cirka 15% af $BH_4$-enhederne aktiveres ved lavere temperaturer end resten. For $Ca(BH_4)_2$ observeredes, udover rotationsdynamikken, en uidentificeret hændelse, som ifølge beregningerne sandsynligvis skyldes $H_2$-interstitielle defekter. I god overensstemmelse med eksperimenter, aktiveres $C_3$-type rotationer ved lavere temperaturer end $C_2$-type rotationer.

For at undersøge reaktionsvejes omgivelser, blev der udviklet en metode til at finde højderyggen mellem førsteordens saddelpunkter på en multidimensional overflade. Information om højderyggen kan bruges til at verificere den harmoniske approksimation brugt i forbindelse med transition-state-teorien anvendt til bestemmelse af reaktionshastigheder, specielt i forbindelse med verificeringen af at andenordens saddelpunkter, maksima langs højderyggen, er beliggende højere sammenlignet med førsteordens saddelpunkter. Yderligere kan korrektioner til den harmoniske approksimation estimeres ved direkte evaluering af det konfigurative integerale langs højderyggen. Nye minima langs højderyggen kan også identificeres sideløbende med reaktionsvejs-optimeringen, og derigennem kan yderligere transitions-mekanismer afsløres. Metoden er baseret på modifikation af gradienten, for et sæt af punkter langs reaktionsvejen der forbinder saddelpunkterne, så den iterativt konvergerer mod højderyggen. Ved hver iteration under optimeringen, inverteres gradienten langs en ustabil egentilstand vinkelret på reaktionsvejen. Dette afbilder effektivt højderyggen mod en minimum reaktionsvej, som kan findes med flere forskellige kendte teknikker. Metoden blev anvendt til at studere Al adatom diffusion på Al(100) overfladen, for at finde højderyggen mellem en samlet bevægelse af 2, 3 eller 4 atomer, samt hoppemekanismer i forbindelse med diffusion. Der var signifikante korrektioner for samlet bevægelse af 3 og 4 atomer. Højderyg-metoden er en enkel metode som kan anvendes til at verificere reaktionshastigheder, men har potentialet for at bestemme mere nøjagtige hastigheder i sig selv, ved at repræsentere transition-state med højderyggen.

# Contents

**Preface** ii

**Abstract** iii

**Resumé** iv

**I Introduction** 1

**1 Introduction** 3
1.1 Stationary Points . . . 3
1.2 Atomic Simulations . . . 4
1.3 Mobile Energy Solutions . . . 5
1.4 Summary . . . 6
1.5 Chapter Outline . . . 7

**II Theoretical Methods** 9

**2 Traversing Potential Energy Surfaces** 11
2.1 The Schrödinger Equation . . . 11
2.2 The Born-Oppenheimer Approximation . . . 12
2.3 Quantum Calculations . . . 13
2.3.1 The Electronic Structure Problem . . . 13
2.3.2 Density Functional Theory . . . 14
2.4 Analytical Potential Energy Surfaces . . . 17
2.5 Forces . . . 18
2.6 Locating Minima . . . 19
2.7 The Hessian Matrix . . . 19
2.8 Saddle Points . . . 20
2.9 Steepest Descent Paths . . . 21

**3 Transition State Theory** 23
3.1 Motivation . . . 23
3.1.1 The Time-scale Problem . . . 23

3.2 The Basics . . . 24
3.2.1 Assumptions . . . 24
3.2.2 The Transition State . . . 25
3.3 Reaction Rates . . . 25
3.3.1 Optimisation of the Rate . . . 26
3.3.2 Harmonic Transition State Theory . . . 27

**4 First Order Saddle Point Methods** **31**
4.1 Introduction . . . 31
4.2 The Dimer Method . . . 31
4.3 The Nudged Elastic Band Method . . . 35

**III Research Topics** **41**

**5 Metal Borohydrides** **43**
5.1 Introduction . . . 43
5.2 Tetragonal Symmetry . . . 44
5.3 Calcium Borohydride [$\beta$-$Ca(BH_4)_2$] . . . 45
5.4 Magnesium Borohydride [$\beta-Mg(BH_4)_2$] . . . 48
5.5 Summary . . . 51

**6 Ridge Mapping** **53**
6.1 Introduction . . . 53
6.2 Ridge Mapping . . . 53
6.2.1 Numerical Instabilities . . . 56
6.3 Energy Ridge Mapping . . . 58
6.3.1 Beyond Harmonicity . . . 59
6.4 Corner Cutting . . . 60
6.4.1 Minimise corner cutting . . . 60

**7 Self Diffusion of Aluminium** **63**
7.1 Introduction . . . 63
7.2 Energy Ridges . . . 64

**8 Coupled Hydrogen Defects in Perovskites** **69**
8.1 Introduction . . . 69
8.2 Results and Discussion . . . 70
8.2.1 Calculational Parameters . . . 70
8.2.2 Searching for Diffusional Mechanisms . . . 70
8.2.3 DFT Ridge Calculations . . . 70
8.2.4 Summary . . . 73

**9 Summary** **75**
9.1 Outlook . . . 76

**Bibliography** **79**

## IV Publications 87

**A Hydrogen Rotational and Translational Diffusion in Calcium Borohydride from Quasielastic Neutron Scattering and DFT Calculations** **89**

**B Hindered Rotational Energy Barriers of $BH_4^-$ Tetrahedra in $\beta$-$Mg(BH_4)_2$ from Quasielastic Neutron Scattering and DFT Calculations** **99**

**C A method for finding the ridge between saddle points applied to rare event rate estimates** **111**

# Part I

# Introduction

Chapter 1

# Introduction

## 1.1 Stationary Points

The border between mathematics, physics and chemistry is often times obscure and the methods developed for one, may very well benefit the others. This relationship is obvious for mathematical methods that get adopted for physics and chemistry but the reverse is also possible (for example the Davidson method for eigenvalue and eigenvector calculation [1]). Common to all the aforementioned, and other, fields, is some form of functional analysis where the study of stationary points[1] is generally of great interest. For systems of limited dimensionality, finding stationary points is no more complex than solving a root problem for the function's derivative. However, once systems grow beyond a few dimensions, solving the root problem becomes infeasible. Furthermore, the lack of a global analytical function makes it impossible to simply solve for the roots. This is, generally, the case in simulations on the atomic scale, which is the main subject of this thesis. While the methods discussed here are developed in that field, applying them to purely mathematical problems and within other fields is merely a question of interest and implementation, thus they are presented as general as possible in order to appeal to a wider audience.

Locating extrema using local information, i.e. the gradient, is a well known technique [2], whereas the gradient is simply followed in the appropriate direction (positive for maxima and negative for minima) until it vanishes.[2] Finding other stationary points is less obvious and classifying them depends on the second order derivatives (or even higher in special cases[3]) Finding such points

[1] Points where the first derivative is zero.

[2] Global extrema are, conversely, extremely difficult to find using only local information and guaranteeing that a given extremum is a global one is nearly impossible. [3] See [4–10] for such efforts.

[3] For example the Monkey Saddle `http://mathworld.wolfram.com/MonkeySaddle.html`

without explicitly evaluating higher order derivatives is an important subject within atomic simulations, since their calculation is very costly when using non-analytical models to describe the atomic interaction.

## 1.2 Atomic Simulations

The focus of this thesis is the application and improvement of theoretical methods to calculational reaction rate chemistry. The underlying methods that allow this are numerous and their discovery span ages in time, from Newton's equations of motion [11] up to modern day methods for solving Schödinger's equation [12] for quantum systems [13–15], from the discovery of calculus and vector math to modern methods for solving eigenvalue problems [16].

Simulations of atomic systems are an integral part of modern atomic scale research, whether it be to investigate specific electronic structure properties (e.g. [17]), performing atomic dynamics (e.g. [18]), investigating macroscopic properties (e.g. [19]) or simply finding stable structures (e.g. [20]). Simulations are commonly employed in the analysis of interesting material properties (see for example catalytic properties [21]), the screening of candidate materials — to eliminate the need to synthesize as many unsuccessful materials — for various processes (see for example hydrogen storage [20]) and further collaboration and comparison with experiments (see for example stability research of ammines [22]).

Reaction chemistry, generally, happens on a timescale of microseconds which is, essentially, eternity when seen from the vantage point of the fast moving atomic vibrations, which happen on a timescale of femtoseconds. Bridging this gap is an important research subject which remains open, despite noble efforts (some of which are described in chapter 3) that have moved the field a long way by introducing statistical methods that are able to exploit the timescale difference to treat the events independently of each other [23–28].

### The Significance of Stationary Points in Atomic Simulations

The potential energy of atomic systems can be evaluated as a function of the atomic coordinates [12, 29, 30]. The most important features of such mappings are generally considered to be the minima which represent stable configurations of the atoms. The transition between minima is then considered to be a chemical reaction. These can range, for example, from rotations of specific groups with minimal impact on the properties of the material (as seen in chapter 5) and motion of water molecules in liquid water, where the chemistry remains unchanged, to adsorption and the breaking of strong chemical bonds. In understanding the transition in question, the path of least resistance (or minimum energy path) is an essential concept, since the highest point along it defines the potential energy that must be overcome and the path itself is a good indicator of the reaction

pathway. The top point is a non-extremal stationary point (in this case, a first order saddle point) and information about the frequency of a given transition (the reaction rate) can be inferred from from it and its surroundings, which is of central importance in chemistry [26, 27]. The surroundings of a first order saddle point are considered its immediate environment, but care must also be taken that any neighbouring higher order saddle points are sufficiently far away in potential energy and space. This latter criteria for the surroundings is often disregarded, especially in systems for which the approximations in question generally perform well. Part of the reason for this is the lack of a simple-to-use method for mapping the surroundings and neighbouring saddle points. In this thesis an effort is made to bridge that gap (chapter 6).

## 1.3 Mobile Energy Solutions

Being able to transport energy in a compact and safe way is a major concern of modern society. Offering alternatives to fossil fuels is essential and thus, a highly active field of research is the design of novel materials for energy conversion, energy storage and catalysis. If energy storage is taken as an example, given appropriate energy densities and stability, kinetics are essential. Reaction rates are used, either directly or indirectly, to investigate all of these factors, naturally with particular emphasis on kinetics.

#### Fossil Fuels

Ancient lifeforms, chemically packed with the Sun's energy and compressed over millions of years by the weight of the Earth's crust, have served mankind cheap and readily available energy for millennia as fossil fuels [31]. When only considered as an energy carrier, fossil fuels are superb. So superb, in fact, that any current alternative mobile storage medium is neither competitive with regards to energy density nor price. This is, of course, not the whole story as the production of fossil fuels has been expected to reach its peak for some time [32]. Once this peak has been reached, the increasing demand of the ever expanding population, would quickly overwhelm the production capabilities and, more importantly, the Earth's reserves. Fossil fuels will not be an option. Furthermore, the ongoing climate change is an unacceptable side product of burning carbon rich fossils [33].

Finding a viable alternative is one of the most important research subjects of the late 20th and early 21st centuries.

#### Energy Trapping

Fossil fuels serve both as energy sources and carriers. If they are to be replaced alternatives must be found for both. Sustainable ways to capture the Sun's energy tend to do so intermittently, e.g. solar panels can not be kept in direct

sunlight during the night and at times the weather is still during which, windmills are of little use. The problem is then to regulate the energy, to store excess when it is produced and to distribute it when none is produced. This is where the fossil fuels serve(d) as energy carriers.

### Hydrogen as an Alternative

Out of all the elements, hydrogen is the lightest and its chemical bonds hold a remarkable amount of energy. Its abundance in on Earth and its non-harmful by-products (water and oxygen), make it a great candidate for a mobile energy store.

Directly storing hydrogen as a gas requires a very large volume or high pressure while storing it as a liquid requires cooling and/or pressurised tanks. Neither is a very compelling solution for use in, for example, the average car. Such solutions have, nevertheless, been deployed for example in buses where it is easy to fit huge tanks.

Another way of storing hydrogen is in metal hydrides, where the hydrogen is either trapped in the metal's lattice or chemically bound within the metal. These storage solutions tend to have more reasonable volumetric densities (at a reasonable cost of the gravimetric density) but often require excessive operating conditions for loading/unloading [34].

The reasons for the low volumetric capacity of the pure hydrogen solutions is simple, the tank is too big. But understanding the underlying reasons for the high stability is an ongoing research topic. An essential piece in that puzzle is understanding the kinetics of the material, how the hydrogen moves and how/why/when the material deforms. Such knowledge can then be used to create better materials with more appropriate properties.

### Fuel Cells

Once hydrogen has been stored and retrieved it is generally used in fuel cells to produce electricity without combustion. Currently this process depends on rare and expensive elements, such as platinum, to catalyse the reaction. This dependence on low-availability materials can very well become a bottleneck for the implementation of the so-called hydrogen economy. Investigating catalytic activity and designing cheap, efficient, catalysts is highly dependant on understanding the kinetics and the catalytical pathways involved.

## 1.4 Summary

Most of the challenges the hydrogen economy faces are limited by kinetics in some way or other. Catalysis and storage currently being the most important ones.

Near saddle points is encoded information about kinetics which is highly useful in designing and implementing the future. Helping to understand the problems of the past and discovering novel materials for the future.

## 1.5 Chapter Outline

The publications (part IV) will not be retold but rather summarised and, where applicable, expanded on in their respective chapters. Reading the thesis first is recommended, then reading the papers for further detail and context.

**Part I : Introduction**

A general introduction and a guide to the contents of the thesis.

**Part II : Theoretical Methods**

Methods and concepts that are important to the work presented in this thesis are discussed. This part is not intended as an exhaustive resource for the methods in question but more as an introduction, sufficient to understand the thesis. For more in-detail discussion of individual methods, refer to their respective citations. Basic understanding of vector mathematics, calculus and atomic physics is assumed.

**Chapter 2 : Traversing Potential Energy Surfaces** Dynamics of atomic scale systems are discussed. The concept of a potential energy surface and its creation and interesting features are addressed.

**Chapter 3 : Transition State Theory** Reaction rates in theoretical chemistry are non-trivial. In this chapter the transition state theory for calculating reaction rates is discussed along with its harmonic approximation.

**Chapter 4 : First Order Saddle Point Methods** Methods for locating saddle points are discussed in detail.

**Part III : Research Topics**

The original work of the thesis is presented.

**Chapter 5 : Metal Borohydrides** A brief overview of the theoretical aspects of papers A and B, as well as the nature of the collaboration between theory and experiments in the context of limited availability of experimental results.

**Chapter 6 : Ridge Mapping** The methodology of paper C is presented in a more general context than in the paper itself. A more detailed look at numerical instabilities in ridge calculations is presented along with an outlook as to minimising said instabilities without sacrificing the accuracy of the ridge determination.

**Chapter 7 : Self Diffusion of Aluminium** A look at the self-diffusion of Al on the Al(100) surface is summarised from paper C. The results mainly focus on the failures of the harmonic approximation to transition state theory and how to correct for the errors encountered.

**Chapter 8 : Coupled Hydrogen Defects in Perovskites** A brief look at DFT ridge calculations of coupled hydrogen defects in a $SrTiO_3$ perovskite system.

**Part IV : Publications**

The publications relevant for this thesis.

# Part II

# Theoretical Methods

Chapter 2

# Traversing Potential Energy Surfaces

*This chapter introduces the idea of potential energy surfaces (PESes) and discusses their creation, interesting features and exploration.*

## 2.1 The Schrödinger Equation

A central theme in atomic simulations is the solution of the Schrödinger equation [12], which is the quantum analogue of Newton's equations of motion [11], governing the motion of the electrons and nuclei, as well as any other observables. For a non-relativistic system of $N = N_e + N_n$ particles ($N_e$ electrons and $N_n$ nuclei), the time independant Schrödinger equation,

$$\widehat{H}\Psi = E\Psi, \tag{2.1}$$

must be solved in order to calculate the total energy of the system, $E$, and the wave function, $\Psi \equiv \Psi(\mathbf{r}_1, \mathbf{r}_2, \ldots, \mathbf{r}_{N_e}, \mathbf{R}_1, \mathbf{R}_2, \ldots, \mathbf{R}_{N_n})$, which depends on the spatial coordinates of each electron, $\mathbf{r}_i$, and each nucleus, $\mathbf{R}_i$, using the total energy operator (more commonly referred to as the Hamiltonian),

$$\widehat{H} = \sum_i^N \widehat{T}_i + \widehat{V}. \tag{2.2}$$

Similar to classical systems the Hamiltonian encompasses both kinetic energy, $\widehat{T}_i = -\nabla_i^2/2$, [1] and potential energy, $\widehat{V} = V(\mathbf{R}, \mathbf{r})$, represented in position space, which will be used exclusively in this thesis. Though it may look innocent, solving the Schrödinger equation, which is a second order partial derivative problem, is a daunting task and in most cases significant approximations must be made. Efforts to solve the Schrödinger equation are discussed in section 2.3.

[1] In atomic units

## 2.2 The Born-Oppenheimer Approximation

In order to simplify — and in many cases, make possible — quantum calculations of large atomic systems, the difference in weight of the electrons and the nuclei[2] is exploited by performing the calculations in two steps. First, while the nuclei are kept motionless by excluding their kinetic operator from the Hamiltonian (equation (2.2)), the electronic wavefunction and energy are determined, followed by a calculation for the motion of the nuclei. The assumption is, essentially, that for any motion of the nuclei, the electrons will move instantly and relax to their ground state to accommodate. This is commonly known as the Born-Oppenheimer approximation [29].

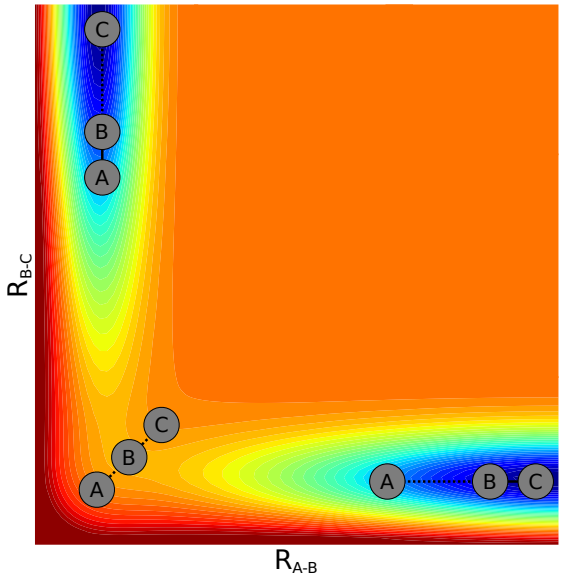


**Figure 2.1:** A schematic example potential energy surface. The axes are functions of nuclear positions, showing the distance between atoms A and B on the one hand and B and C on the other. The red areas indicate high potential energy and the blue ones low potential energy. The reaction shown is a classical example of a 2 atom molecule getting hit by a third atom. Then passing over a potential energy barrier and forming a different 2 atom molecule. In order to pass over the barrier, the incoming molecule must have sufficient kinetic energy.

This decoupling allows for a mapping of the potential energy as a function of the nuclear coordinates (commonly referred to as the potential energy surface or PES), as opposed to the continuum of PESes which exist should the motion

[2] ∼4 orders of magnitude for hydrogen and more for the heavier elements.

of the nuclei and electrons be determined simultaneously. PESes are, generally, not known *a priori* and much effort is spent on traversing them to discover interesting features, such as minima, which represent stable atomic structures, or, as we shall see below, reaction pathways.

All the work carried out in this thesis employs the Born-Oppenheimer approximation.

## 2.3 Quantum Calculations

With increased computing power and, in particular, advances in parallel algorithms, it is now possible to calculate a range of physical properties for materials at the atomic level without the use of any experimental parameters. Such *ab initio* methods are generally attempts at solving or approximating the Schrödinger equation (section 2.1) for the ground state[3]. Multiple strategies exist and choosing one generally involves considering the trade-off between accuracy and computational effort. The one used in this thesis is the Density Functional Theory, where the many-electron problem is *exactly* divided into multiple one-electron problems.

### 2.3.1 The Electronic Structure Problem

Solving the Schrödinger equation (section 2.1) is not a menial task, as it is a second order partial derivative equation in multiple dimensions that can only be solved exactly for very small systems. Due to the high dimensionality of the wavefunction, simply storing it for a medium-to-large system is physically impossible.[4]

The Born-Oppenheimer approximation (section 2.2) allows for the separation of the Hamiltonian to an electronic part and a nuclear part. Thus, the positions of the nuclei, $\mathbf{R}_I$, only enter the calculations as parameters. A full quantum treatment will not be discussed here as the goal is to build a PES.

A non-relativistic system of $N_e$ electrons (and $N_n$ nuclei) is described by the time independent Schrödinger equation [12], whose Hamiltonian (equation (2.2)) is

$$\widehat{H} = -\frac{1}{2}\sum_{i}^{N_e}\nabla_i^2 + \sum_{i}^{N_e}\sum_{j>i}^{N_e}\frac{1}{|\mathbf{r}_i - \mathbf{r}_j|} + \sum_{i}^{N_e}\sum_{I}^{N_n}\frac{1}{|\mathbf{r}_i - \mathbf{R}_I|} + \widehat{V}_{\text{env}}, \tag{2.3}$$

which consists of four terms when written out in full. First there is the kinetic energy of the electrons, $\widehat{T}_{\text{e}} = -2^{-1}\sum_i^{N_e}\nabla_i^2$, then the electron-electron interac-

[3] Non-ground state calculations are not considered in this thesis.

[4] Consider a system of only 16 electrons (e.g. an oxygen molecule), sampled on a grid of 10 points in each direction. Since each electron has 3 degrees of freedom the number of gridpoints will be $10^{16\times 3} = 10^{48}$. Compared with the estimated amount of atoms in/on the Earth, $\sim 10^{50}$, the amount of gridpoints is impossible to store, even for a modest system. This problem is commonly referred to as the exponential wall [30].

tion, $\widehat{U}_{\text{ee}} = \sum_i^{N_e} \sum_{j>i}^{N_e} (|\mathbf{r}_i - \mathbf{r}_j|)^{-1}$, followed by the electron-nuclei interaction, $\sum_i^{N_e} \sum_I^{N_n} (|\mathbf{r}_i - \mathbf{R}_I|)^{-1}$, and finally any further environmental influence (e.g. an applied electric field) is represented by a single term, $\widehat{V}_{\text{env}}$. The last two terms are often bundled into a single external term,

$$V_{\text{ext}} = \sum_i^{N_e} \sum_I^{N_n} \frac{1}{|\mathbf{r}_i - \mathbf{R}_I|} + V_{\text{env}}, \tag{2.4}$$

since these are system dependant, while $\widehat{T}_{\text{e}}$ and $\widehat{U}_{\text{ee}}$ can be considered universal.

### 2.3.2 Density Functional Theory

One of the most popular and common techniques for solving the electronic structure problem is the Density Functional Theory (DFT) which can exactly (in theory) solve the Schrödinger equation. However, in practice, approximations must be made for all but the most simple systems. Nevertheless, DFT has produced many interesting and good results and is now a well established formalism that is continually being reviewed and improved. Furthermore, the *ab initio* nature of DFT makes it a great companion to experimental research, not only for comparison and prediction of interesting materials but also to assist and expand upon data analysis.

The success of DFT yielded one of its founders, Walter Kohn, the Nobel Prize in chemistry in 1998, for the development of the density functional theory [30] along with John Pople for his development of computational methods in quantum chemistry [35].

#### The Hohenberg-Kohn Theorems

The earliest mention of a DFT type method were made by Thomas [36] and Fermi [37] but the heart of DFT lies in the Hohenberg-Kohn theorem, which reformulates the electronic structure problem to depend on the 3 dimensional, ground state, electron density, $\rho_0(\mathbf{r})$, instead of the $3N$ dimensional wavefunction, $\Psi(\mathbf{r}_1, \mathbf{r}_2, \ldots, \mathbf{r}_N)$. According to the first Hohenberg-Kohn theorem [13], any external term, $V_{\text{ext}}$, in equation (2.3) yields a different electron density from any non-identical $V'_{\text{ext}}$ up to trivial additive constant, for the ground state. In other words: there is a one-to-one correspondence between the wavefunction and the electron density of the ground state and all observables that depend on the wavefunction can, thus, be extracted from the ground state density. This allows a re-formulation of the Schrödinger equation, with the energy as a functional of the electron density,

$$E[\rho_0] = \langle \Psi[\rho_0] | \widehat{H} | \Psi[\rho_0] \rangle. \tag{2.5}$$

Furthermore, the second Hohenberg-Kohn theorem [13] adds a variational [38, 39] way to discover the true ground state density and ground state energy,

$$E_0 = \min_{\rho} E[\rho]. \tag{2.6}$$

This work alone is still missing key elements in order to efficiently solve for the wavefunction and energy, namely the wavefunction to density mapping is not known.

### The Kohn-Sham Equations

Counter-intuatively re-introducing wave functions was the solution proposed by Walter Kohn and Lui Jeu Sham in 1965 [40]. Inspired by Hartree's work nearly four decades earlier [41], multiple non-interacting single particle wave functions, $\phi_i(\mathbf{r}_i)$, took the place of the many-body wave function (or electron density), such that

$$\rho(\mathbf{r}) = \sum_{i=1}^{N_e} \left|\phi_i(\mathbf{r}_i)\right|^2, \tag{2.7}$$

where each electron would be subject to an effective potential, $v(\mathbf{r})$, due to all the particles in the system (including itself, the nuclei and any external factors). Solving for $\phi_i$ and $\epsilon_i$ (the Kohn-Sham energies) using multiple Schrödinger type equations (commonly referred to as the Kohn-Sham equations),

$$\left\{-\frac{1}{2}\nabla^2 + v(\mathbf{r})\right\}\phi_i(\mathbf{r}_i) = \epsilon_i\phi_i(\mathbf{r}_i), \tag{2.8}$$

can be done iteratively in a variational manner, from an initial guess for the electron density.

Constructing the effective potential becomes the main problem here, since an exact $v(\mathbf{r})$ yields an exact solution to the whole electronic structure problem. The external potential, $\widehat{V}_{\text{ext}}$, from equation (2.4) enters unchanged as it contains only static information. Conversely, the electron-electron interaction, $\widehat{U}_{\text{ee}}$, enters in a changed form. In fact, it is introduced as two terms, one for interaction with the electron density as a whole, commonly referred to as the hartree potential ($v_{\text{H}}(\mathbf{r})$) and a second one for many-electron and Pauli-exclusion effects, $v_{\text{XC}}(\mathbf{r})$, the so-called exchange-correlation potential,

$$v(\mathbf{r}) = V_{\text{ext}}(\mathbf{r}) + v_{\text{H}}(\mathbf{r}) + v_{\text{XC}}(\mathbf{r}). \tag{2.9}$$

The hartree potential is an integral over the electron density,

$$v_{\text{H}}(\mathbf{r}) = \int \frac{\rho(\mathbf{r}')}{|\mathbf{r} - \mathbf{r}'|} d^3\mathbf{r}', \tag{2.10}$$

and the exchange-correlation potential is of the form,

$$v_{\mathrm{XC}}(\mathbf{r}) = \frac{\partial E_{XC}[\rho(\mathbf{r})]}{\partial \rho(\mathbf{r})}. \tag{2.11}$$

Thus far the formalism is exact, however, all the difficult parts, $E_{\mathrm{XC}}[\rho(\mathbf{r})]$, have yet to be discussed.

### The Exchange-Correlation Functional

The Kohn-Sham equations are in principle exact, however, the exchange-correlation functional, $E_{\mathrm{XC}}[\rho(\mathbf{r})]$, is generally not known and has to be approximated. The accuracy of this approximation is a major factor in determining the accuracy of DFT as a whole. A detailed discussion of Exchange-Correlation functionals is material enough for a whole chapter, thus only the basic approximations will be discussed here.

The Local Density Approximation (LDA) [40] treats exchange-correlation as if it were a homogeneous electron gas.

$$E_{\mathrm{XC}}^{\mathrm{LDA}}[\rho(\mathbf{r})] = \int \epsilon_{\mathrm{XC}}^{\mathrm{hom.}}[\rho(\mathbf{r})]\rho(\mathbf{r})d^3\mathbf{r}, \tag{2.12}$$

where $\epsilon_{\mathrm{XC}}^{\mathrm{hom.}} = \epsilon_{\mathrm{X}}^{\mathrm{hom.}} + \epsilon_{\mathrm{C}}^{\mathrm{hom.}}$ is the exchange-correlation density. The exchange part is known exactly,

$$\epsilon_{\mathrm{X}}^{\mathrm{hom.}}(\mathbf{r}) = -\frac{3}{4}\sqrt[3]{\frac{3}{\pi}} \int \sqrt[3]{\rho^4(\mathbf{r})}. \tag{2.13}$$

The correlation part, however, is not known but has been tabulated using accurate Quantum Monte-Carlo simulations [42]. The LDA favors systems with slowly changing densities, such as solid systems, and has been successfully used in one form or another for a long time. Molecules are, however, not described as well by LDA and binding energies tend to be overestimated [43, 44]. A better description of molecules can be attained with the use of the generalised gradient approximation (GGA) [45, 46], which is similar to LDA but the gradient of the electron density is also taken into account,

$$E_{\mathrm{XC}}^{\mathrm{GGA}}[\rho(\mathbf{r})] = \int \epsilon_{\mathrm{XC}}^{\mathrm{hom.}}[\rho(\mathbf{r}), |\nabla\rho(\mathbf{r})|]\rho(\mathbf{r})d^3\mathbf{r} \tag{2.14}$$

Multiple other exchange-correlation functional types exist, each with different strong suits, some fitted to empirical data[5] [47] in order to increase accuracy by sacrificing their physical intuition, while others are hybrids of previous functionals [48–51], aimed at improving the accuracy at the cost of computational time.

[5] putting into question their *ab initio* nature.

### Implementation

The Kohn-Sham equations must be solved numerically. Multiple schemes and packages exist for solving this task. The ones used in this thesis are Dacapo[6] [15] and GPAW[7] [14].

**Dacapo** expands the wave functions in plane-waves and uses pseudopotentials [52] to represent areas near the ionic cores.

**GPAW** is a real space based implementation of the projector augmented wave (PAW) [53] methodology. Being expanded on real space grids, better parallelisation can be achieved at the cost of less consistent energies and forces, due to the so-called eggbox effect.[54]

In this thesis the GGA functional developed by Perdew and Wang in 1991 is used for DFT generated PESes in chapter 5 [55]. And in chapter 8, the typical RPBE [15] GGA functional was used. More advanced functionals may exist but here the application to DFT was meant to be as general as possible in order to properly test the methods being developed. As for other parameters, the reader is referred to the specific sections and papers.

## 2.4 Analytical Potential Energy Surfaces

For very large systems or when timing is a factor, it is possible to employ classical potential functions for calculating the potential energy and gradient. Such potential functions are tailor made for a given bond and generally give poor physical insight when used on a different system.

Most common are pair-potentials[8], where each atom in the system feels an interaction with every other atom up to a cut-off radius, and this interaction can be tuned by empirical parameters. Such potentials are very helpful during the development of methods and two such, EMT [57] and EAM [58] were extensively used for testing the novel method presented in chapter 6 and paper C. Furthermore, if tuning the parameters of the potential well enough is possible, the potential can be used to perform calculations that are infeasible for quantum methods, such as long term molecular dynamics of large systems (see for example [59]).

### Embedded Atom Model

The Embedded Atom Model (EAM) [58] operates under the principle that an atom's energy is a functional of the system's electron density. Its basic formula

[6] `https://wiki.fysik.dtu.dk/dacapo/dacapo`
[7] `https://wiki.fysik.dtu.dk/gpaw/`
[8] Many-body potentials are also possible (see for example [56])

for the energy of atom $i$ is

$$E_i = F_\alpha \left( \sum_{i \neq j} \rho_\beta(|\mathbf{R}_i - \mathbf{R}_j|) \right) + \frac{1}{2} \sum_{i \neq j} \phi_{\alpha\beta}(|\mathbf{R}_i - \mathbf{R}_j|), \tag{2.15}$$

where $\phi_{\alpha\beta}$ is a short-range pairwise-potential function, $\rho_\beta$ is the contribution to the electron charge density from atom $j$ of type $\beta$ at $\mathbf{R}_i$ and $F_\alpha$ is an embedding function that represents the energy required to place atom $i$ of type $\alpha$ into the electron cloud.

EAM has been parametrised very well, e.g. for Al surfaces using DFT data [60] and used successfully in studies of the self-diffusional mechanisms on the Al(100) surface [61]

Extensive use was made of potential functions in this thesis. Simple and quick test cases using EMT [62] — which operates under similar approximations as EAM — served to produce PESes that could be visualised in two dimensions, while still retaining the properties of truly multidimensional systems in chapter 6. While more extensive tests were carried out in chapter 7 on systems that are known to be described well with analytical PESes, i.c. EAM.

## 2.5 Forces

Since the PES, $E(\mathbf{R})$, is generally not known *a priori*, traversing it is difficult without a guide. Such a guide exists in the form of the gradient, $\nabla E(\mathbf{R})$, in which information about the increase/decrease of the function (here: PES) is encoded. The gradient points towards the direction of greatest increase, however, in atomic simulations such areas are, commonly, of little interest. Most of the time, systems are at, or near, stable structures, which are represented by minima on the PES. Defining a force that, similarly to real world forces, points the system towards areas of lowest potential energy, is straight forwards as the negative gradient,

$$\mathbf{F}(\mathbf{R}) = -\nabla E(\mathbf{R}). \tag{2.16}$$

The gradient is not directly available from DFT calculations, as for other non-analytical PESes. Fortunately, for such variational calculations, a force theorem has been developed, stating that $\partial E/\partial\lambda$ can be evaluated for a continuous parameter $\lambda$ on which the wavefunction, $\Psi(\lambda)$, depends implicitly,

$$\frac{\partial E}{\partial \lambda} = \langle \frac{\partial \Psi}{\partial \lambda} | \widehat{H} | \Psi \rangle + \langle \Psi | \frac{\partial \widehat{H}}{\partial \lambda} | \Psi \rangle + \langle \Psi | \widehat{H} | \frac{\partial \Psi}{\partial \lambda} \rangle. \tag{2.17}$$

Utilising the orthogonality of the wavefunction and the fact that the hamiltonian is hermitian, the first and last terms are zero,

$$\frac{\partial E}{\partial \lambda} = \langle \Psi | \frac{\partial \widehat{H}}{\partial \lambda} | \Psi \rangle. \tag{2.18}$$

Once the electronic wave function has been constructed, which is the most time consuming part, the gradient can be calculated.

For DFT, and any other Born-Oppenheimer calculations, $\lambda$ can be the nuclear coordinates. Since the forces depend on the variational determination of the wave function (or electron density), their accuracy cannot be guaranteed and they tend to have numerical noise [54] which must be considered when using the forces.

The theorem has been proved independently by multiple authors [63, 64] but is generally attributed to Richard Feynman [65] and Hans Hellmann [66], as the Hellmann-Feynman Theorem.

## 2.6 Locating Minima

Searching for minima[9] is an important subject as they represent stable structures on PESes. Using the available local information, the energy and the force, it is possible to follow the force with an appropriate step size until the gradient is zero, at which time a stationary point has been reached. Generally this point will be a minimum but classifying non-minima will be discussed below.

Multiple techniques exist for performing these minimisations[10] in as few iterations as possible. Some are as simple as adjusting the step size to simulate velocity, while others detect changes in this fictional velocity and adjust accordingly [2, 67]. Still other methods build up information about the curvature and assume a quadratic environment [68].

## 2.7 The Hessian Matrix

For a real function $f$ of $n$ variables, $\mathbf{x} = (x_1, x_2, \ldots, x_n)$, there exists an $n \times n$ matrix, H, which contains all the second partial derivatives,

$$\mathrm{H} = \begin{bmatrix} \frac{\partial^2 f}{\partial x_1^2} & \frac{\partial^2 f}{\partial x_1 \partial x_2} & \cdots & \frac{\partial^2 f}{\partial x_1 \partial x_n} \\ \frac{\partial^2 f}{\partial x_2 \partial x_1} & \frac{\partial^2 f}{\partial x_2^2} & \cdots & \frac{\partial^2 f}{\partial x_2 \partial x_n} \\ \vdots & \vdots & \ddots & \vdots \\ \frac{\partial^2 f}{\partial x_n \partial x_1} & \frac{\partial^2 f}{\partial x_n \partial x_2} & \cdots & \frac{\partial^2 f}{\partial x_n^2} \end{bmatrix}. \tag{2.19}$$

The second derivative of a function represents, in particular, information about its local curvature, or how rapidly the first derivative changes. Classification of stationary points (and implicitly critical points) relies on the eigenvalues of H, $\lambda_i$,

[9] Or equivalently maxima but due to the context of atomic simulations the discussion will be on minima.

[10] Also often referred to as optimisations

- Minimum if all $\lambda_i > 0$
- Maximum if all $\lambda_i < 0$
- Saddle Point if some but not all $\lambda_i < 0$
- Otherwise higher order derivatives are needed for classification

H is named after the German mathematician Ludwig Otto Hesse and is commonly referred to as the Hessian matrix, or Hessian for short [69].

In the context of atomic simulations, $n$ is generally 3 times the number of atoms in the system, as each one has 3 independent degrees of freedom and the function in question is often the potential energy of the system. In most modern software packages both the potential energy and force are readily available while the second order derivatives are, generally, not available without explicit and, often, costly calculations.

## 2.8 Saddle Points

Saddle points are stationary points, i.e. with zero gradient, on a multidimensional function, $f(\mathbf{R})$, that are neither maxima nor minima.

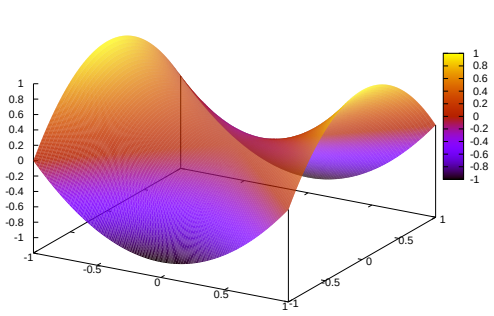


(a) 2D saddle point, $f(x = 0, y = 0) = x^2 - y^2$. A minimum is the $x$-direction and a maximum in the $y$-direction

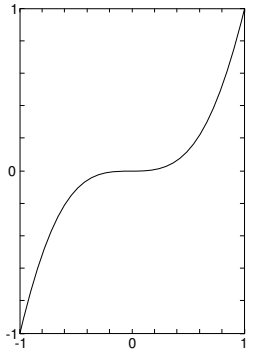


(b) 1D saddle point, $f(x = 0) = x^3$. Neither a maximum nor a minimum but the gradient is vanishing.

**Figure 2.2:** Examples of first order saddle points.

A common view of a saddle (point) can be found in figure 2.2(a), as the function $f(x, y) = x^2 - y^2$ which near $(x, y) = (0, 0)$ resembles a saddle, used when riding horses, curving upwards in one direction (along the horse) and downwards in the other (perpendicular to the horse). This image of a saddle point lacks a few elements to tell their whole story but acts as a good general case. On functions of higher dimensionality than 2, different orders of saddle points are possible. The order of the saddle point is decided by the amount of degrees of freedom that are not at a minimum, or the non-positive eigenvalues of the Hessian. As such, figure 2.2(a) shows a first order saddle point on a two dimensional function. In this thesis, saddle points of order $N$ will be indicated by $\mathrm{SP}_N$ from here on.

The Hessian at the SP displayed in figure 2.2(a) has one negative eigenvalue, however, a saddle point with one or more vanishing eigenvalues is also possible, such as the 1D example $f(x = 0) = x^3$, seen in figure 2.2(b). In this thesis, saddle points generally have strictly negative eigenvalues.

Locating SPs in multiple dimensions is a non-trivial task as only a limited number of steepest decent paths lead to each one while the majority lead to minima. A number of schemes for locating $\mathrm{SP}_1$s have been suggested (see [70] for a review), out of which two popular ones are discussed in chapter 4: The Dimer method and the Nudged Elastic Band method. Furthermore, an extension to these methods for finding higher order SPs is presented in chapter 6.

In the context of atomic simulations, SPs are important in describing reactions and reaction rates.

## 2.9 Steepest Descent Paths

Steepest Descent Paths (SDPs) are paths on a multidimensional function, $f$, for which there is no perpendicular gradient component,

$$\nabla \mathbf{f} - (\nabla \mathbf{f} \cdot \hat{\boldsymbol{\tau}})\hat{\boldsymbol{\tau}} = \mathbf{0}, \tag{2.20}$$

where $\hat{\boldsymbol{\tau}}$ is the tangent to the path. They can be created by following the negative gradient until it vanishes. SDPs can begin anywhere, apart from points with a vanishing gradient, but, generally, end at minima (most common) or SPs. Two sorts of SDPs are of particular interest for the work presented in this thesis, both of which are discussed below.

### Minimum Energy Paths

The Minimum Energy Path (MEP) is a collection of two specific SDPs, used in the context of theoretical reaction chemistry and represents a likely reaction path on the PES. It connects two minima through a $\mathrm{SP}_1$, where each SDP begins [71], with an infinitesimal displacement along the path.

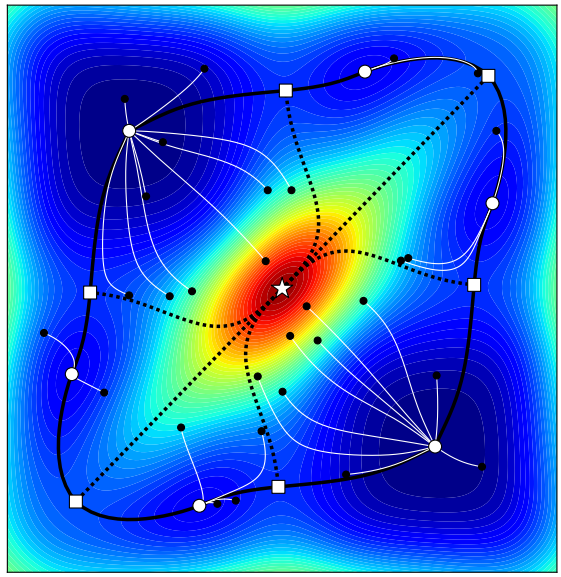

**Figure 2.3:** Examples of steepest descent paths. The white symbols represent stationary points, the circles are minima, the squares are $SP_1$s and the star is a $SP_2$. The black circles are starting points for random SDPs (the white lines). The black lines are specific SDPs, the dotted ones are ridges while the solid ones are MEPs.

### Ridges

Similar to MEPs, ridges are collections of specific SDPs, but with their starting points at a $SP_2$s and their end points in $SP_1$s. Of course, MEPs do not exist near $SP_2$s, and the analogue ends there as the criterion for a ridge demands a negative eigenvalue in the reduced Hessian, perpendicular to the path.

Chapter 3

# Transition State Theory

*Transition State Theory (TST) is a formalism dedicated to providing reaction rates in a purely theoretical setting where running dynamical trajectories of the required length is infeasible. This chapter briefly describes the theory and its most popular implementation.*

## 3.1 Motivation

### 3.1.1 The Time-scale Problem

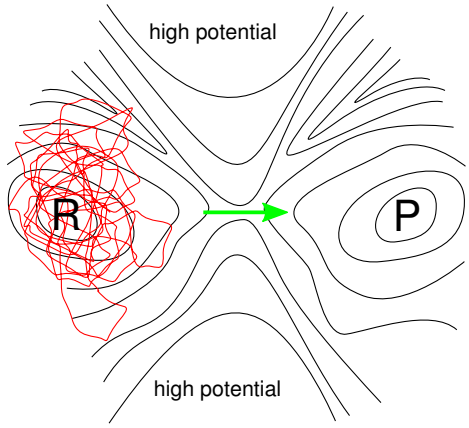


**Figure 3.1:** The time-scale problem. The system will mostly spend time near the minimum of the reactants basin (R), the red trajectory, while the reactions of interest, green arrow, happen only rarely.

In atomistic simulations there is a often a clear separation of timescales

between the most interesting events. With local vibration of the atoms being very fast, typically on the order of $10^{14}$ Hz [72], while non-local reordering of atoms, motion between minima on the PES, often considered as rare-events, typically occur on the order of $10^{3}$ Hz for a system with a "typical" energy barrier of 0.5 eV. Depending on the temperature of the system, a tremendous amount of calculations (on the order of $10^{10}$) would have to be performed to have a reasonable probability of seeing each rare-event while also fully modelling the details of the atomic vibrations.

Even though performing dynamics long enough to describe both types of events, is technically possible, e.g. by minimising vibrations to allow for longer timesteps [73, 74] or modifying the PES [75], the key to long-timescale dynamics still lies outside the reach of such methods as they spend most of their time performing dynamics that are not of particular interest for transitions between states. This is true, in particular, for calculations that rely on costly, but accurate, quantum calculations and/or large systems.

In the problem lies also the solution, when there is such a clear separation of time-scales, it is possible to treat the problem with statistical methods. Essentially dealing with the vibrational areas of the PES (the basins) by averaging over them and seperately locating ares of transitions.

## 3.2 The Basics

### 3.2.1 Assumptions

There are four main assumptions made within TST, which vary in severity.

**Born-Oppenheimer** The Hamiltonian of the system can be separated, resulting in a single PES for the trajectories.

**Classical Dynamics** No tunnelling or other quantum effects — apart from those offered by the calculational method of the PES — are taken into account in the original formulation of TST. The motion of the system is governed by classical dynamics. Quantum effects are included in extensions to TST (see for example [76–78]) but this is not relevant to the work presented in this thesis and will not be discussed further.

**Thermal Equilibrium** The system will spend considerable time in each basin of the PES, long enough for a Boltzmann distribution for system can be employed. For systems with large energy barriers in comparison with the thermal energy [1], this assumption holds well but for smaller barriers or high temperatures it breaks down as thermal equilibrium becomes difficult to achieve and the separation of timescales is lost

[1] A rule of thumb is that $E_{\mathrm{b}} > 5k_{\mathrm{B}}T$ [79]

**No Re-Crossings** Once the system has left a basin, it does not return for a significant amount of time (long enough to thermalise in the new basin). This assumption is the most serious and efforts to minimise its effects are discussed below.

### 3.2.2 The Transition State

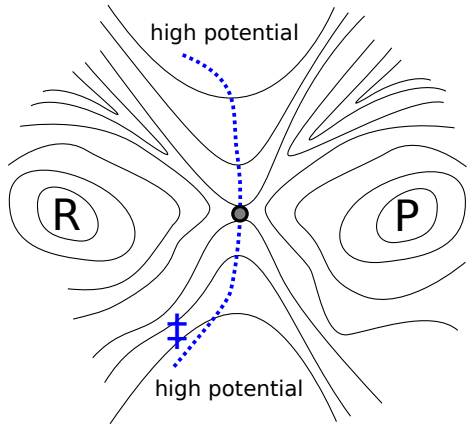


**Figure 3.2:** The transition state, ‡. Representing a bottlenck region through wich all reactive trajectories (going from reactants, R, to products, P) must go. The grey circle is a $SP_1$.

When dividing the phase space (position and momentum) into two areas, reactants (R) and products (P), a hypersurface separating the two emerges. This hypersurface is referred to as the transition state (‡)[2] and represents a bottleneck region with regards to the free energy, which each reactive trajectory crosses on its way from R to P. Commonly, momentum is disregarded in the definition of the phase space, which is then $3N$ dimensional (for a system of $N$ particles), within which the ‡ is a $3N-1$ dimensional subspace.

## 3.3 Reaction Rates

Considering a canonical ensemble[3], the probability that a system in thermal equilibrium, i.e. described by a Boltzmann distribution, is in a given state $S$ is

[2]The double dagger, ‡, is a conventional symbol for the transition state
[3]The number of particles and volume is constant and there is a well defined temperature.

dependant on its configurational integral [4],

$$Z_S = \int_S e^{-E(\mathbf{R})/k_\mathrm{B}T} d\mathbf{R} \tag{3.1}$$

For a hyperplanar, ‡, the reaction rate, $k_\mathrm{TST}$, is defined as the probability of being in the ‡ subspace of R,

$$P_\ddagger = \frac{Z_\ddagger}{Z_\mathrm{R}}, \tag{3.2}$$

thermally averaged over R, with velocity away from R,

$$k_\mathrm{TST} = \frac{1}{2}|\mathbf{v}_\perp| P_\ddagger, \tag{3.3}$$

where $\mathbf{v}_\perp$ is the velocity component perpendicular to the ‡ and the factor 1/2 comes from the fact that only half of the trajectories will be moving away from R. Due to the different dimensionality of the ‡ and R, $P_\ddagger$ is not strictly a probability as it has the unit $\mathrm{m}^{-1}$ but looking at it as such aids general understanding of the rate's definition.

The velocity at each point $\mathbf{R}$ can be taken from a Maxwell distribution,

$$\langle|\mathbf{v}|\rangle = \sqrt{\frac{2kT}{\pi\mu}}, \tag{3.4}$$

where $\mu$ is the effective mass of the transition. The rate then becomes

$$k_\mathrm{TST} = \sqrt{\frac{kT}{2\pi m}} \frac{Z_\ddagger}{Z_\mathrm{R}}. \tag{3.5}$$

### 3.3.1 Optimisation of the Rate

Choosing a good ‡ is essential for the accuracy of TST. A trajectory that crosses the ‡ more than once will result in a reaction rate that is higher than the exact rate. Either it ended again in R or crossed the ‡ multiple times on its way to P. Thus the ‡ can act as a variational parameter for the TST rate, [80–82]

$$k_\mathrm{TST} \geq k_\mathrm{exact}. \tag{3.6}$$

Should optimising the ‡ be infeasible or insufficient, a different approach can be taken to bring $k_\mathrm{TST}$ closer to the exact rate by estimating the error and correcting for it with a multiplication factor $\kappa_\mathrm{D} \in (0, 1]$,

$$k_\mathrm{exact} = \kappa_\mathrm{D}\ k_\mathrm{TST}. \tag{3.7}$$

[4] The continuous classical analogue to the discrete partition function.

By starting dynamical trajectories from the ‡, which must still be reasonably good, and counting the recrossings while tracking which basin the trajectories end in, a ratio between reactive trajectories and non-reactive ones can be calculated [83],

$$\kappa_{\mathrm{D}} = \lim_{n\to\infty} \frac{n_{\mathrm{react.}}}{n}, \tag{3.8}$$

where $n$ is the total amount of trajectories, started from $\mathbf{R} \in ‡$, and $n_{\mathrm{react.}}$ is the number of trajectories that end in P. More recent schemes (see for example [82, 84, 85]) work in the same spirit, albeit slightly more rigorous. The scheme presented in equation (3.8), nevertheless, captures the essence of dynamical corrections.

### 3.3.2 Harmonic Transition State Theory

To actually calculate the partition functions can be a tedious task and finding a good transition state is a non-trivial one, if possible (see for example [86]). Fortunately, for many systems (e.g. solid state materials), the transition state can be approximated and the configuration integrals simplified.

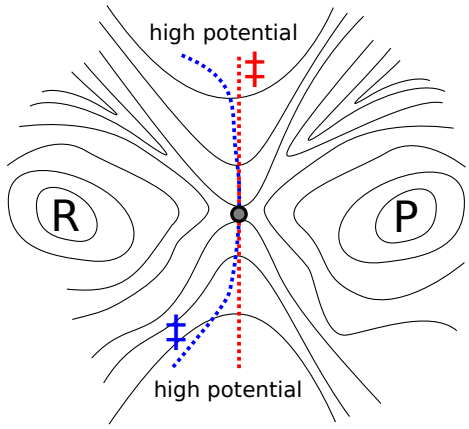


**Figure 3.3:** The transition state, (blue ‡), and the harmonic transition state (red ‡). The grey circle is a $SP_1$.

Between any two basins there exists a $SP_1$, which represents the lowest possible potential energy that the system must overcome in order for a transition to occur. Exploiting this, the ‡ can be chosen as a hyperplane in which the $SP_1$ resides and whose normal is the eigenmode that corresponds with the lowest eigenvalue of the Hessian. This greatly simplifies the definition of the ‡. Furthermore, in order to simplify the calculation of the partition functions, the PES

near both ‡, $E_\ddagger$, and R, $E_\mathrm{R}$, are represented by second degree Taylor expansions,

$$E_\mathrm{R}(\mathbf{q}_\mathrm{R}) \approx E(\mathbf{R}_\mathrm{min}) + \frac{1}{2}\sum_i^{3N} k_{\mathrm{R},i} q_{\mathrm{R},i}^2, \tag{3.9}$$

$$E_\ddagger(\mathbf{q}_\ddagger) \approx E(\mathbf{R}_{\mathrm{SP}_1}) + \frac{1}{2}\sum_i^{3N-1} k_{\ddagger,i} q_{\ddagger,i}^2, \tag{3.10}$$

where $\mathbf{q}_{[\ddagger,\mathrm{R}]}$ are the eigenvectors of the Hessian, $q_{[\ddagger,\mathrm{R}],i}$ is the displacement along eigenvector $i$, $k_{[\ddagger,\mathrm{R}],i}$ are the corresponding Taylor coefficients, all for the ‡ and R respectively, and $E(\mathbf{R}_{[\mathrm{SP}_1,\mathrm{min}]})$ are the energies at the $\mathrm{SP}_1$ and the minimum of the R basin, respectively. Since the central points of the expansions are stationary, the first derivatives vanish from the expression, leaving only constants along with the second order terms.

Due to the format of the energy approximations, the configurational integrals become trivial Gaussian integrals,

$$\int_{-\infty}^{\infty} e^{-k_i q_i^2/2k_\mathrm{B}T} dq_i = \sqrt{\frac{2\pi k_\mathrm{B}T}{k_i}}. \tag{3.11}$$

The reaction rate then reduces to

$$k_\mathrm{HTST} = \sqrt{\frac{k_\mathrm{B}T}{2\pi\mu}} \frac{e^{-E(\mathbf{R}_{\mathrm{SP}_1})/k_\mathrm{B}T} \prod_i^{3N-1} \sqrt{\frac{2\pi k_\mathrm{B}T}{k_{\ddagger,i}}}}{e^{-E(\mathbf{R}_\mathrm{min})/k_\mathrm{B}T} \prod_i^{3N} \sqrt{\frac{2\pi k_\mathrm{B}T}{k_{\mathrm{min},i}}}}. \tag{3.12}$$

Most of the $k_\mathrm{B}T$ and $2\pi$ parameters cancel each other, leaving only one set by means of the different dimensionality of ‡ and R. Rearrangement of equation (3.12), along with the multiplication of $\mu^{3N}$ on both sides of the fraction, yields,

$$k_\mathrm{HTST} = (2\pi)^{-1} \frac{\prod_i^{3N} \sqrt{\frac{k_{\mathrm{min},i}}{\mu}}}{\prod_i^{3N-1} \sqrt{\frac{k_{\ddagger,i}}{\mu}}} e^{-(E(\mathbf{R}_{\mathrm{SP}_1}) - E(\mathbf{R}_\mathrm{min}))/k_\mathrm{B}T}. \tag{3.13}$$

Now it is possible to insert the respective vibrational frequencies,

$$\nu_* = \sqrt{\frac{k_*}{\mu}} (2\pi)^{-1}, \tag{3.14}$$

into equation (3.13),

$$k_\mathrm{HTST} = \frac{\prod_i^{3N} \nu_{\mathrm{min},i}}{\prod_i^{3N-1} \nu_{\ddagger,i}} e^{-(E(\mathbf{R}_{\mathrm{SP}_1}) - E(\mathbf{R}_\mathrm{min}))/k_\mathrm{B}T}, \tag{3.15}$$

for a rate that depends only on the vibrational frequencies and energies at the $\mathrm{SP}_1$ and minimum as well as the temperature. This form of the rate agrees

with the empirically observed temperature dependence of the rate originally expressed by Arrhenius [87, 88]. The potential energy barrier is addressed in the exponent while the entropical effects are addressed in the so-called prefactor.

Chapter 4

# First Order Saddle Point Methods

*This chapters discusses in some detail two methods for locating first order saddle points, which serve as the springboard for the higher order saddle point methods in chapter 6.*

## 4.1 Introduction

Finding first order saddle points ($SP_1$s) is a non-trivial task in multiple dimensions, when only local information is available and computational resources are limited, such that calculation of the Hessian matrix is infeasible. Nevertheless, multiple methods exist for finding $SP_1$s and can, generally, be divided into two distinct categories.

1. General methods which can locate a nearby $SP_1$, requiring only a point with a non-zero gradient as input.
2. More specific methods that require two minima as input to find the MEP and a $SP_1$ ($SP_1$s) between them.

The latter category is well suited for use within computational chemistry and such methods have been successfully used to describe reaction paths between two stable structures (see for example [89]). The first category has a more broad use as it is not constrained to find specific $SP_1$s, however, the downside is that there is no guarantee that the found $SP_1$ will be of interest.

## 4.2 The Dimer Method

The Dimer algorithm [61] is in essence a method for finding the eigenmode corresponding to the lowest eigenvalue of the Hessian, while performing no direct calculations of the second derivatives [75]. This information is then used to

locate $SP_1$s which are defined by a negative eigenvalue in the Hessian and its corresponding eigenmode.

Given only an initial point, $\mathbf{R}$, on a multidimensional function, $E(\mathbf{R})$, the goal is to, iteratively, locate a nearby $SP_1$, using no direct calculation of the Hessian, i.e. using only the function's values and its gradient, $\nabla E(\mathbf{R})$. Indirect information about the Hessian is, however, used in the form of an estimate of the eigenmode corresponding to its lowest eigenvalue (the minimum mode). By using the minimum mode, $\hat{\mathbf{e}}$, it is possible to locally transform $SP_1$s to minima while using conventional techniques to move up-hill and locate the $SP_1$.

The dimer method can be split into three independent phases.

1. Estimating the minimum mode.
2. Transforming the gradient to make $SP_1$ appear as minima.
3. Translating the point according to the transformed gradient.

Only the first of the phases is unique to the dimer algorithm. A setup phase, which typically includes randomly displacing $\mathbf{R}$ [90] is also required if the search starts from a minimum (or any other stationary point).

### Minimum Mode Estimate

Estimating the second derivative of $E$ along a given unit vector, $\hat{\mathbf{s}}$, at point $\mathbf{R}$ can be done numerically, using finite differences. For the occasion, a pair of points (the dimer), $[\mathbf{R}_\mathrm{A}, \mathbf{R}_\mathrm{B}]$, are chosen, close to current point $\mathbf{R}_0$, such that

$$\mathbf{R}_\mathrm{A} = \mathbf{R}_0 + \Delta_\mathrm{D}\hat{\mathbf{s}} \quad \text{and} \quad \mathbf{R}_\mathrm{B} = \mathbf{R}_0 - \Delta_\mathrm{D}\hat{\mathbf{s}}, \tag{4.1}$$

where $\Delta_\mathrm{D}$ is a predefined constant to determine the length of the dimer and the separation in the finite difference estimate and as such should be kept as low as possible. Using only the function's values, the second derivative (or curvature), $C_\mathbf{s}$, becomes

$$C_\mathbf{s}(\mathbf{R}_0) \equiv \left.\frac{\partial^2 E}{\partial \hat{\mathbf{s}}^2}\right|_{\mathbf{R}_0} \approx \frac{E(\mathbf{R}_\mathrm{A}) + E(\mathbf{R}_\mathrm{B}) - 2E(\mathbf{R}_0)}{\Delta_\mathrm{D}^2}, \tag{4.2}$$

where $E_\mathrm{x} \equiv E(\mathbf{R}_\mathrm{x})$. As the gradient points away from each minimum, it is convenient to define a force, $\mathbf{F}$ that points towards minima instead, for use in the iterative minima search, $\mathbf{F}_\mathrm{x} \equiv -\nabla E(\mathbf{R}_\mathrm{x})$, where $x$ represents any subscript of $\mathbf{R}$. Should the gradient be readily available, as it often is, equation (4.2) can be rewritten to depend on it instead,

$$C_\mathbf{s}(\mathbf{R}_0) \approx \frac{(\mathbf{F}_\mathrm{B} - \mathbf{F}_\mathrm{A}) \cdot \hat{\mathbf{s}}}{\Delta_\mathrm{D}}. \tag{4.3}$$

Rotating $\hat{\mathbf{s}}$ around $\mathbf{R}_0$, according to the rotational force (as seen in figure 4.1),

$$\mathbf{F}^{\circlearrowleft} = (\mathbf{F}_\mathrm{A} - \mathbf{F}_\mathrm{B}) - ((\mathbf{F}_\mathrm{A} - \mathbf{F}_\mathrm{B}) \cdot \hat{\mathbf{s}})\hat{\mathbf{s}}, \tag{4.4}$$

until $C_{\mathbf{s}}$ is minimized yields an estimate for, both, the lowest eigenvalue, $C_{\min} = C_{\mathbf{s}}$, of the Hessian and its corresponding eigenmode, the minimum mode, $\hat{\boldsymbol{\epsilon}} = \hat{\mathbf{s}}_{\min}$. The rotation happens in a plane spanned by $\hat{\mathbf{s}}$ and $\mathbf{F}^{\circlearrowleft}/|\mathbf{F}^{\circlearrowleft}|$ A number of rotational schemes can be employed, such as a finite difference conjugate gradient method [61] and, as described in [91], by expanding the curvature, exactly, as a Fourier series. Both of these schemes require extra calculations to figure out the optimal angle of rotation but the latter is better suited when the accuracy and/or consistency of the force cannot be guaranteed [91], e.g. when doing DFT calculations.

Often $\mathbf{F}_0$ is calculated to get a more accurate translational force. This can be taken advantage of in order to cut down the amount of computations. Assuming a quadratic behaviour near the dimer, the gradient at either of the dimer's endpoints can be extrapolated from the other endpoint and the central point [92],

$$\mathbf{F}_{\mathrm{B}} = 2\mathbf{F}_0 - \mathbf{F}_{\mathrm{A}}, \tag{4.5}$$

with $\mathbf{F}_{\mathrm{B}}$ being the extrapolated force. Since $\mathbf{F}_0$ is static and does not require additional calculations during the iterative rotation, performing this extrapolation yields significant calculational reductions, up to a factor of half.

Further extrapolations are possible, if multiple rotations are performed (which is often not the case). Between rotational iterations, it is possible to use the previous calculations of an end point to extrapolate the rotated values for the next iteration [93]. These, however, yield much less reductions than the extrapolation in equation (4.5).

### Gradient Transformation

Once a minimum mode estimate is available for the current point, $\mathbf{R}_0$, it is possible to transform the force so that any $\mathrm{SP}_1$ appears as a minimum with regards to the force. As discussed in section 2.8, $\mathrm{SP}_1$s are stationary (with zero gradient) and the Hessian has one and only one negative eigenvalue. The goal is, thus, to maximize the function's value along the minimum mode while minimizing it along all other eigenmodes. This can be achieved, simply, by inverting any force components along the minimum mode,

$$\mathbf{F}_0^{\mathrm{t}} = \mathbf{F}_0 - 2(\mathbf{F}_0 \cdot \hat{\boldsymbol{\epsilon}})\hat{\boldsymbol{\epsilon}}, \tag{4.6}$$

shown in figure 4.2. In cases were the dimer aligns itself with a contour of the potential in a convex region (where the Hessian has only positive eigenvalues), it is possible that a lot of time will be spent there. In order to circumvent this, a different force transformation,

$$\mathbf{F}_0^{\mathrm{t}} = -(\mathbf{F}_0 \cdot \hat{\boldsymbol{\epsilon}})\hat{\boldsymbol{\epsilon}}, \tag{4.7}$$

is often used in these regions. This latter transformation simply inverts the force along the minimum mode while ignoring any other components. This along with

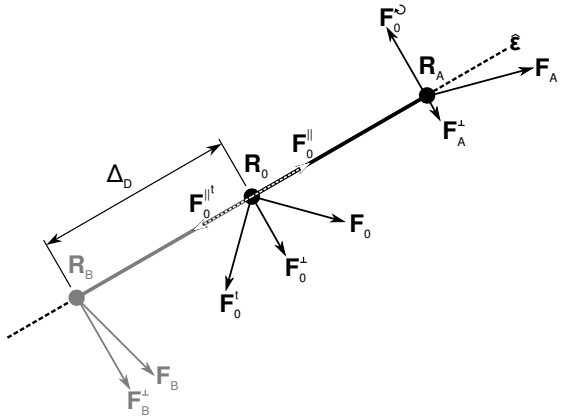


**Figure 4.1:** A schematic overview of the force components acting within the dimer method. $\mathbf{R}_\mathrm{A}$ and $\mathbf{R}_0$ are the positions of the dimer images with the greyed out $\mathbf{R}_\mathrm{B}$ as the virtual image (equation (4.5)). Each force component is labeled with super- and subscripts as follow: 0, A and B in subscripts refer to at which point they are calculated, $\perp$ and $\parallel$ in superscripts refer to the specific component of the full force (perpendicular and parallel to the minimum mode estimate, respectively), t in a superscript refers to the transformed force (equation (4.6)), $\circlearrowleft$ refers to the rotational force (equation (4.4)) and no superscript refers to the gradient force. $\Delta_\mathrm{D}$ is the distance between dimer points (equation (4.1) and $\hat{\boldsymbol{\epsilon}}$ is the current minimum mode estimate (or $\hat{\mathbf{s}}$ during rotation).

a fixed, artificially large, step size should yield less iterations spent near minima and more near $\mathrm{SP}_1$s [61].

### Iterative Translation

After the force has been transformed such that $\mathrm{SP}_1$s appear as minima — $\mathrm{SP}_1$s, however, remain unchanged with regards to the function's value — it is possible to use conventional algorithms for finding minima as long as they support a systematic increase in the function's value. A finitie difference method was suggested in the original implementation [61] while more recent papers [93] have used other methods, such as the L-BFGS algorithm [68].

### Usage in Atomic Simulations

The Dimer method was developed within the context of atomic simulations, where the function in question is the PES and the variables the spatial degrees of freedom of each atom in the system.

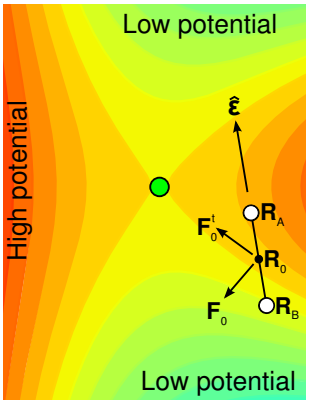


**Figure 4.2:** The translational scheme of the dimer method. $\mathbf{R}_\mathrm{A}$ and $\mathbf{R}_\mathrm{B}$ are the positions of the dimer images with the $\mathbf{R}_0$ as the central image (equation (4.1)). $\hat{\boldsymbol{\epsilon}}$ is the minimum mode (or direction of lowest curvature) $\mathbf{F}_0$ is the gradient force acting on the central image and $\mathbf{F}_0^\mathrm{t}$ is the transformed, effective force (equation (4.6)). The green circle is the $\mathrm{SP}_1$ under investigation. (This figure is adapted from Figure 4 in [61])

Multiple scenarios can be envisioned where the Dimer method brightly shines, two of which will be briefly discussed.

1. Consider a method that is not able to fully converge to a $\mathrm{SP}_1$, such as the Double Nudged Elastic Band, which yields a configuration close to the $\mathrm{SP}_1$ and a reasonably good estimate of the minimum mode. In such a situation the Dimer will quickly, and at low computational cost, find the $\mathrm{SP}_1$ exactly [94].

2. As discussed in section 3.1.1, performing long time-scale dynamics is difficult. The dimer can be used to map all relevant $\mathrm{SP}_1$s leading out of a basin[1], then using HTST (section 3.3.2) to find the reaction rates for each $\mathrm{SP}_1$, it is possible to construct a probability table of possible events. Using this table of events within the Kinetic Monte Carlo formalism [95], it is possible to traverse the PES in an accelerated manner [96].

### Performance

Since the Dimer heavily depends on finite difference methods, inaccurate gradients can, thus, render the method useless. When used with classical potentials, this is not a problem, but when used with quantum mechanical forces, such as those provided by DFT, care must be taken to converge the electronic structure well [54] and/or to a larger than normal $\Delta_\mathrm{D}$.

## 4.3 The Nudged Elastic Band Method

Finding Steepest Decent Paths (SDPs) on a multidimensional function, $E(\mathbf{R})$, from a given point is simple by following the negative gradient (force) with a

[1] It is, of course, nearly impossible to find *all* $\mathrm{SP}_1$s associated with a basin and even more difficult to know when they have all been found. Reference [90] discusses efforts to that end.

small step size. On the other hand, finding specific SDPs that end at minima is not. The Nudged Elastic Band (NEB) algorithm is concerned with aligning a path with certain SDP paths, generally the MEP (see [71] for an exception), leading to two minima from a common $SP_1$.

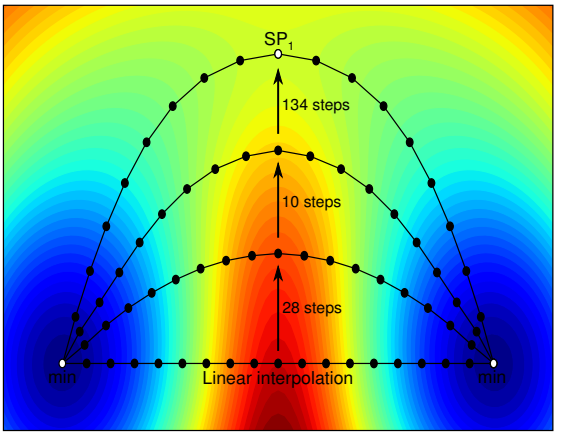


**Figure 4.3:** Snapshots from a NEB optimisation of a MEP. Each series of connected circles (the images) represents the path at a specific iteration step. The white circles are stationary points, two minima and a $SP_1$. Red and blue areas represent high and low values of the function in question, respectively.

### The Force Modification Scheme

An initial guess of the path is commonly a, discretised, linear interpolation between the minima but any guess is suitable as long as the force can be calculated. Each of the discrete points is, traditionally, referred to as an image and is simply a replica of the system in question but with different coordinates from the other images. Each image, labelled $i$, feels two separate forces. First there is the negative gradient of the function, $\mathbf{F}_i \equiv -\nabla E(\mathbf{R}_i)$, but only the component perpendicular to the path is retained,

$$\mathbf{F}_i^{\perp} = \mathbf{F}_i - (\mathbf{F}_i \cdot \hat{\boldsymbol{\tau}}_i)\hat{\boldsymbol{\tau}}_i, \tag{4.8}$$

where $\hat{\boldsymbol{\tau}}$ is the tangent to the path (see below). This reduced force is responsible for minimising the path in the perpendicular direction. Second, there is a virtual force acting purely along the tangent, which takes care of equally spacing the images along the path. There are multiple ways to implement this force, the original implementation of NEB [97] modelled a spring between each set of neighbouring images with a spring constant, $k$, tunable to keep the spring force

of a similar size as the gradient. A more recent, and successful, version of the "spring force", depends on the norms to the neighbouring images instead of the full vectors [98],

$$\mathbf{F}_i^{\mathrm{S}} = k(|\mathbf{R}_{i+1} - \mathbf{R}_i| - |\mathbf{R}_i - \mathbf{R}_{i-1}|), \tag{4.9}$$

where $k$, is still present as a stiffness parameter. By varying the stiffness parameter for each image, it is possible to increase the density of images in interesting areas, such as near the $\mathrm{SP}_1$ [99].

Combining the forces from equations 4.8 and 4.9 into an effective force, as seen in figure 4.4,

$$\mathbf{F}_i^{\mathrm{eff}} = \mathbf{F}_i^{\perp} + \mathbf{F}_i^{\mathrm{S}}, \tag{4.10}$$

will iteratively bring the path to a discretised version of the MEP, with even, or controlled, spacing, as can be seen in figure 4.3.

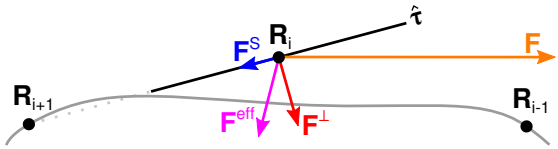


**Figure 4.4:** A schematic overview of the force components acting within the NEB method. $\mathbf{R}_{i-1}$, $\mathbf{R}_i$ and $\mathbf{R}_{i+1}$ are the positions of each image. The label $i$ is ommited from the force symbols as all of them originate at image number $i$. $\mathbf{F}$ (orange) is the gradient force, $\mathbf{F}^{\perp}$ (red) is the force perpendicular to the tangent (equation (4.8)), $\mathbf{F}^{\mathrm{S}}$ (blue) is the spring force (equation (4.9)) and $\mathbf{F}^{\mathrm{eff}}$ (purple) is the effective force (equation (4.10)). The tangent, $\hat{\boldsymbol{\tau}}$, is the unit vector pointing towards the neighboring, higher function value, image, $i+1$ (equation (4.12)).

### Tangent

Since the path must be discretisised, the tangent can not be trivially defined. Multiple possibilities for its definition are available but one that considers only the displacement to the neighboring, higher function value, image has been successful in minimising kinks in the paths [98].

Each image, $i$, will, function value wise, fit into one of four cases:

1. $E(\mathbf{R}_{i-1}) < E(\mathbf{R}_i) < E(\mathbf{R}_{e+1})$
2. $E(\mathbf{R}_{i-1}) > E(\mathbf{R}_i) > E(\mathbf{R}_{e+1})$
3. $E(\mathbf{R}_{i-1}) > E(\mathbf{R}_i) < E(\mathbf{R}_{e+1})$
4. $E(\mathbf{R}_{i-1}) < E(\mathbf{R}_i) > E(\mathbf{R}_{e+1})$

Before discussing each case it is helpful to define vectors to the neighboring images:

$$\boldsymbol{\tau}_i^+ = \mathbf{R}_{i+1} - \mathbf{R}_i \quad \text{and} \quad \boldsymbol{\tau}_i^- = \mathbf{R}_i - \mathbf{R}_{i-1}. \tag{4.11}$$

The first two cases yield simple definitions of the tangent,

$$\hat{\boldsymbol{\tau}}_i = \frac{\boldsymbol{\tau}_i^+}{\left|\boldsymbol{\tau}_i^+\right|} \quad \text{if} \quad E(\mathbf{R}_{i-1}) < E(\mathbf{R}_i) < E(\mathbf{R}_{e+1}) \tag{4.12}$$

and

$$\hat{\boldsymbol{\tau}}_i = \frac{\boldsymbol{\tau}_i^-}{\left|\boldsymbol{\tau}_i^-\right|} \quad \text{if} \quad E(\mathbf{R}_{i-1}) > E(\mathbf{R}_i) > E(\mathbf{R}_{e+1}). \tag{4.13}$$

The other two cases occur when the image is either a local maximum or a local minimum, with regards to its neighboring images. In these latter cases a weighted average — controlled by the difference in the function's value, $\Delta E = [|E(\mathbf{R}_{i+1}) - E(\mathbf{R}_i)|, |E(\mathbf{R}_{i-1}) - E(\mathbf{R}_i)|]$ — of the neighboring tangents is used, in order to avoid any artifacts due to discontinuity,

$$\hat{\boldsymbol{\tau}}_i = \frac{\boldsymbol{\tau}_i^+ \upsilon_i^\pm + \boldsymbol{\tau}_i^- \upsilon_i^\mp}{\left|\boldsymbol{\tau}_i^+ \upsilon_i^\pm + \boldsymbol{\tau}_i^- \upsilon_i^\mp\right|} \quad \text{if} \quad E(\mathbf{R}_{i\pm1}) > E(\mathbf{R}_{i\mp1}), \tag{4.14}$$

where $\upsilon_i^+ = \max(\Delta E)$ and $\upsilon_i^- = \min(\Delta E)$ are the weights.

Using such a tangent, rather than one that depends on both neighbouring images, allows for any perturbations of the path to be dealt with from the top down, independently of the images below. The tangent of the higher image remains accurate and the perturbed image is able to re-converge, as if it were hanging from the higher image. This "hanging" effect then migrates down the path until all images are converged.

### Finding the Exact Saddle Point

The force modifications described above do not guarantee that an image will be exactly at the $SP_1$ in question once converged. By decoupling the top function value image from the spring force, it becomes independant and guiding it to the $SP_1$ can be done in a manner similar to equation (4.6) with the tangent estimate functioning as the minimum mode estimate,

$$\mathbf{F}_{i_{\max}}^{\text{eff}} = \mathbf{F}_{i_{\max}} - (\mathbf{F}_{i_{\max}} \cdot \hat{\boldsymbol{\tau}}_{i_{\max}})\hat{\boldsymbol{\tau}}_{i_{\max}}, \tag{4.15}$$

where $i_{\max}$ refers to the image with the highest function value [99].

### Usage in Atomic Simulations

The NEB method was developed within the context of atomic simulations, where the function in question is the PES and the variables the spatial degrees of freedom of each atom in the system.

Beyond finding the $SP_1$ for use within TST (chapter 3), the MEP is often a good visual indication as to the reaction path and unexpected minima can be detected.

The NEB has been used extensively since its inception, late last century, and a search of the literature for interesting examples will be left as an easy exercise for the reader.

# Part III

# Research Topics

Chapter 5

# Metal Borohydrides

*This chapter describes and expands the theoretical work performed for Papers A and B while commenting on the interaction between theoretical and experimental work.*

## 5.1 Introduction

With high hydrogen density, both volumetric and gravimetric, metal borohydrides are of tremendous interest as possible mobile hydrogen storage candidates. However, they commonly exhibit poor reversibility, slow ab- and desorption kinetics and too high thermodynamic stability [34, 100, 101]. Understanding these drawbacks is an important research subject in order to solve them or discover new and better materials for hydrogen storage.

The work presented here[1] is focussed on detecting and understanding atomic scale hydrogen motion in two species, $Mg(BH_4)_2$ and $Ca(BH_4)_2$ in order to better understand structural transition and decomposition mechanisms. These have shown lower thermodynamic stability than other borohydrides [34, 101], e.g. $LiBH_4$, while still having high hydrogen density (14.9%wt and 11.5%wt, respectively) and showing partial reversibility [102–106]. Out of the possible hydrogen dynamics, rotations of borohydride groups are easily overlooked as uninteresting but they are often associated with order-disorder phase transitions in coordination compounds [22, 107]. Furthermore, longer range diffusion of hydrogen or $BH_4$ could be part of the decomposition mechanism. The work presented here is mainly focussed on detecting and understanding the rotational motion of $BH_4$ groups in the relevant metal borohydrides. Atomic level experimental data for these types of dynamics is scarce and experimental methods are limited to a handful of techniques, one of which is quasielastic Neutron Scattering (QENS), which is sensitive to hydrogen motion [108] on the range of interest.

[1] And in full detail in papers A and B

Due to the scarcity of appropriate experiments, collaboration between experimental and theoretical researchers is essential to fully interpret and understand their results. For some of the borohydrides the unit cells are very large and hard to deal with on the theoretical level. This is well illustrated by the fact that the exact structure of the cells is still in active refinement in the literature [109, 110]. The existence of multiple phases can complicate matters even further as their local geometry may be similar [111–114]. However, for the work presented here, only a single phase was present.

## 5.2 Tetragonal Symmetry

In order to discuss rotational diffusion, a brief introduction to the $BH_4$ symmetry operations is required.

The $BH_4$ unit is a tetrahedron with the hydrogen atoms at the vertices and the boron internally. If the boron is considered to be fixed and the hydrogen atoms are distinguishable, there are 24 possible permutations, thus from a given configuration, 24 symmetry operations are possible.

A common notation for symmetry operations is the one attributed to Schönflies [115] and this notation will be used for discussion of symmetry in this thesis. The relevant symmetry operations for a tetrahedron are as follow:

- $1 \times E$ : Pseudo axis which leaves the system unchanged.
- $3 \times C_2$ : Axes of 2-fold rotation, enter between each pair of vertices and exit through the opposing pair. Opposing axes give identical permutations, thus only 3 axes are considered instead of 6 (figure 5.1(a)).
- $8 \times C_3$ : Axes of 3-fold rotation, enter through each vertex and exit through the opposing plane, to which the axes are normal. Each axis has 2 operations, forward and backward rotation. Even though the permutations are unique, the empiric rotational paths are identical. Thus only 4 $C_3$ axes remain for study (figure 5.1(c)).
- $6 \times \sigma_\mathrm{d}$ : Mirror planes which lie through each pair of vertices with the opposing pair defining the normals (figure 5.1(d)).
- $6 \times S_4$ : Axes of 4-fold rotation and mirroring which lie identical to the $C_2$ axes with a mirror plane normal to themselves. Due to the 4-fold rotation, instead of 2-fold, opposing axes give unique permutations (figure 5.1(b)).

When considering only the $BH_4$ and no environmental effects, the $C$-type operations yield no barrier as the inter-atomic distances do not vary during the operation. On the other hand, when performing the mirror-type operations ($\sigma_\mathrm{d}$ and $S_4$), the inter-atomic distances change, forming a flat $BH_4$ intermediate, which is very energetically unfavourable. Due to this difference in intrinsic

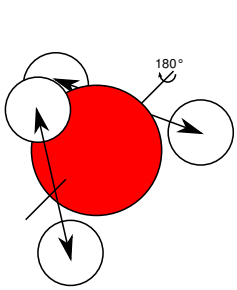


(a) $C_2$ axis: 2-fold rotation.

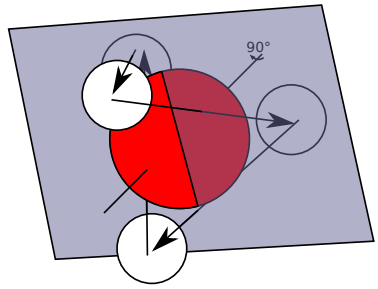


(b) $S_4$ axis: 4-fold rotation-reflection.

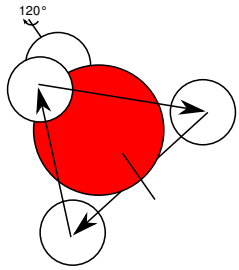


(c) $C_3$ axis: 3-fold rotation.

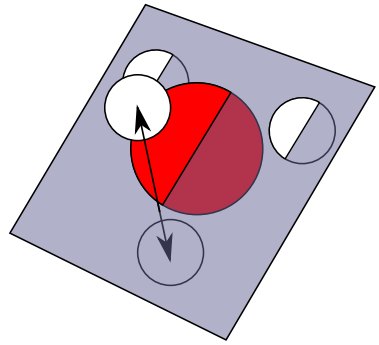

(d) $\sigma_d$ plane: Mirror plane.

**Figure 5.1:** Possible symmetry operations for a tetrahedron, such as the $BH_4$ unit.

barriers and the fact that the mirror-type operations aren't, in fact, rotations, only the $C$-type operations have to be considered when looking at the rotations of the $BH_4$ groups.

## 5.3 Calcium Borohydride [$\beta$-Ca$(BH_4)_2$]

The calculations were carried out using the Atomic Simulation Environment[2] [116] and its implementation of the relevant algorithms. The energies and forces were

[2] `https://wiki.fysik.dtu.dk/ase/`

provided by the Dacapo plane wave DFT implementation [15]. The calculational parameters can be found in the DFT Calculations section of Paper A. The calculational supercell was relaxed from the $P4_2/m$ space group (#84) [109], which contains two formula units, repeated once in each direction, totalling 176 atoms.

The bulk of the initial data from the QENS experiments indicated rotational diffusion of hydrogen, while possible high temperature long-range diffusion was also detected. The experimental data suggested three unique processes, two of which were assigned to rotational diffusion of hydrogen, while the latter was assigned to longer range diffusion. The work focused mainly on rotations around the possible symmetry axes, $C_2$ and $C_3$, of the $BH_4^-$ unit.

### Rotation of $BH_4^-$

By choosing appropriate axes, a contour plot of the rigid rotation was produced (figure 5.2(a)) in order to get an overview of the possible rotations, pure or coupled, and an estimate of their relative barrier heights.

Since the rotational system has three dimensions but the contour plot is limited to only two, the axes had to be chosen carefully as to sample all interesting events. Each $BH_4$ group has three nearest neighbour Ca atoms and each $C_2$ axis roughly lines up with one of the three, nearly equivalent, Ca-B vectors, which means that with regards to symmetry they are also all nearly equivalent. The one with maximal H-Ca distance was chosen as one of the contour axes. The choice of the $C_3$ axis had a similar goal, to minimise H-Ca interaction. This was accomplished by choosing the axis which lies closest to the plane spanned by the three nearest neighbour calcium atoms. This axis samples half of the possible $C_3$ axes when the full $C_2$ rotation is taken into account. Due to symmetrical similarity it is likely that the remaining $C_3$ axes are indirectly sampled also.

The contour plots give an important insight as to which of the possible rotations are the interesting ones and, thus, calculating the more resource intensive MEPs can be limited to the interesting processes. Figure 5.2(a) shows that a $C_3$ axis is lowest in energy and that a wobbly $C_2$ axis with a small intermediate minimum is the lowest energy $C_2$ type rotation. Using these as the starting paths for NEB calculations, the MEPs, shown overlaid in figure 5.2(a), are found and shown as energy profiles in figure 5.2(b).

Right away, the theoretical data was in good agreement with the experimental data, nevertheless, further refinement of the experimental data was possible once the theoretical data for the rotations was complete, which yielded better agreement for the rotational data and an extra point for the possible long range diffusion. This beautifully illustrates how theory and experiments complement and can be used to benefit each other.

In the end, the calculations complemented the experimental data very well, both with regards to the barrier height as well as the characteristic times which are derived from the HTST reaction rates (see Table 2 in Paper A).

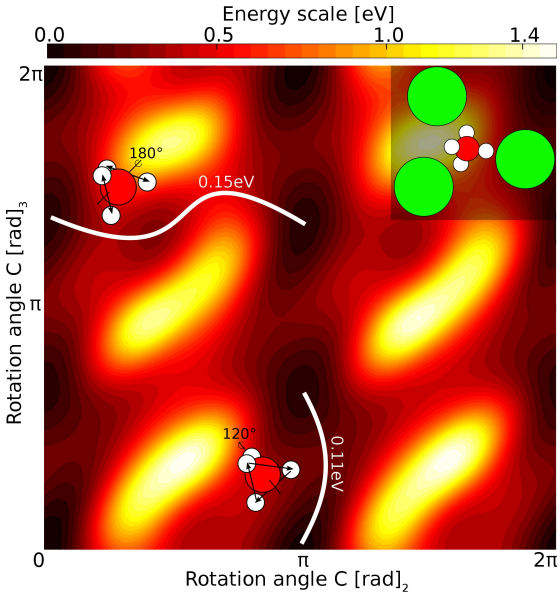


(a) Potential Energy Surface for Ca(BH$_4$)$_2$ with MEPs and the local environment overlaid.

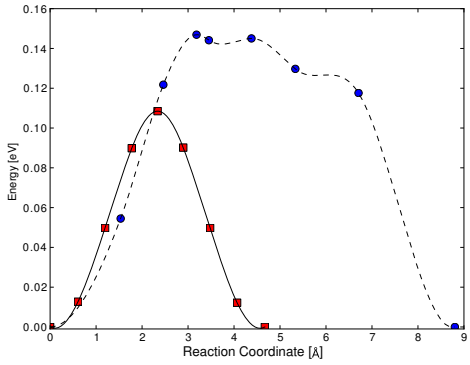


(b) Ca(BH$_4$)$_2$ energy profiles. The blue circles represent the $C_2$-type rotation and the red squares represent the $C_3$-type rotation.

**Figure 5.2:** The rotational analysis of $BH_4^-$ in Ca(BH$_4$)$_2$. It should be noted that some symmetry breaking can be seen in the PES, which is to be expected as the tetragonal symmetry is slightly broken during the minimisation, due to the environment.

### Long-range diffusion

The remaining process was assigned to that of longer range hydrogen diffusion. Multiple diffusional species and mechanisms can easily be imagined. Vacancy mediated $BH_3$, $BH_4$ and H diffusion, interstitial hydrogen, atomic and molecular, and two different interstitial waters were all investigated with NEB calculations, and their results are shown in table 3 of paper A.

The vacancies all had high formation energies (1.56 eV - 2.83 eV) and barriers (0.46 eV - 1.92 eV) while the stable interstitial defects, had lower formation energies (−0.05 eV - 0.40 eV) and barriers (0.09 eV - 0.68 eV). The H-interstitial proved to be unstable and formed an $H_2$-interstitial coupled to an H-vacancy.

The only defect that agreed to any significance with the experimental data, was the $H_2$-interstitial, with a barrier of 0.09 eV (exp. ∼0.12 eV) and diffusional length of 2.1 Å (exp. ∼2.5 Å). The characteristic times were, however, not in agreement (theoretical 0.06 ps vs. exp. 4 ps). These discrepancies might very well be due to the lack of experimental data points, since only two were available for a linear interpolation on an Arrhenius type plot (figure 10 in paper A).

## 5.4 Magnesium Borohydride [$\beta-Mg(BH_4)_2$]

The calculations were carried out using the same packages as before (section 5.3), ASE [116] and Dacapo [15]. The calculational parameters can be found in the DFT calculations section of Paper B. The calculational supercell was relaxed from the *fddd* spacegroup (#70) [111], totalling 176 atoms. The structure consists of 5 symmetry inequivalent $BH_4$ sites which all have similar local structure, being wedged between 2 Mg atoms (figure 5.3). The symmetry inequivalance stems from the fact that each $BH_4$ is slightly displaced from the Mg-Mg axis, the distance from the B to the axis, $L$, influences the barriers.

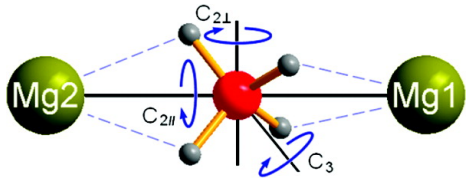


**Figure 5.3:** Schematic representation of the environment of each B atom, and how the different types of axes relate to it.

The experiments could not discern data for individual inequivalent sites but only averages for a given type of process. Three distinct (average) processes were seen, all of which correspond to rotational diffusion. Thus, the work exclusively revolved around understanding which rotations corresponded with the experiments.

For each inequivalent site a number of rigid rotation PESes were constructed[3] in order to get an overview of the interesting events and to limit computations spent on the costly MEP calculations, in a similar fashion as in section 5.3. Due to symmetry not all the axes needed to be considered.

The general result from the PESes was that rotations that maximise the H-Mg distance, $d_{H-Mg}$, had the lowest energies (figure 5.4). In this respect, two distinct types of $C_2$ axes were seen, those parallel to the Mg-Mg axis, $C_2^{\parallel}$, which maximised $d_{H-Mg}$ and those perpendicular to it, $C_2^{\perp}$, where $d_{H-Mg}$ was generally lower and had higher barriers (figure 5.3). MEP calculations for $C_2^{\perp}$ found a combination of other axes yielded the same permutation but at a much lower energy cost. The difference in relative barrier height decreased with decreasing $L$.[4]

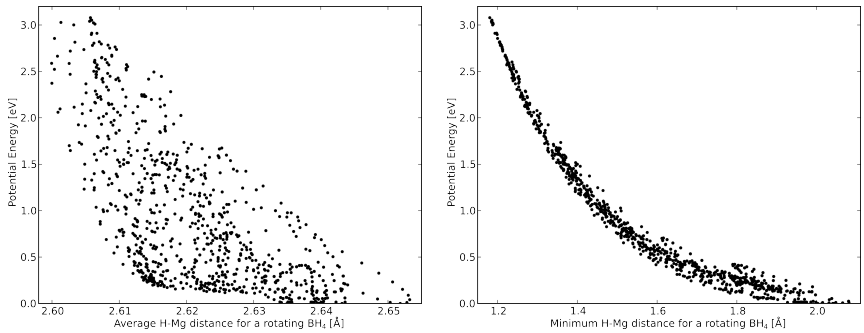


(a) Average H-Mg distance

(b) Minimum H-Mg distance

**Figure 5.4:** For each PES, the distances between the H atoms of the rotating $BH_4$ unit to the neighbouring Mg atoms are plotted. Some systematic features can be seen since the data was produced with specific rotations rather than a uniform distribution. A clear trend for lower energies with higher distances can be seen.

No such clear distinction could be made with regards to the $C_3$ axes. However, due to symmetry many of the $C_3$ axes for a given site yield a very similar PES and the rest would yield barriers that were not in any tune with the experimental results.

The rigid rotation plots are not able to give a full description of the events, neither their geometry nor their energetics. Thus MEP calculations, for each

[3] Examples of which can be seen in figures 13 and 14 of paper B.

[4] The relative difference would be non-existent for $L = 0$ (and $L = \infty$) but none of the $BH_4$ fulfil that criterion.

symmetry inequivalent $BH_4$, were performed with the lowest energy rigid rotation paths as starting positions.

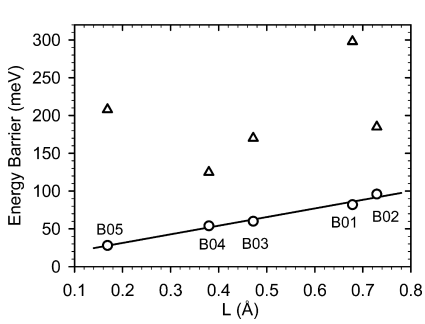


(a) The energy barriers as a function of $L$, the distance from the B to the Mg-Mg axis. The circles are the $C_2$ barriers, while the triangles are the $C_3$ axes. A clear linear relationship can be seen for the $C_2$ axes.

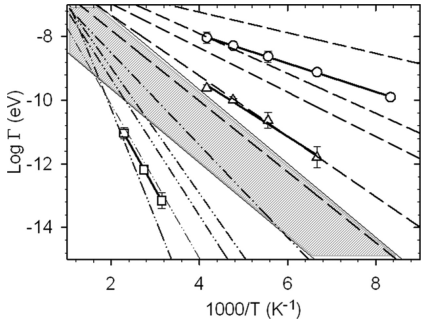


(b) Comparison of the experimental and theoretical results. Arrhenius-type behaviour, where $\Gamma = \Gamma_0 exp(-E_a/k_B T)$ and $\Gamma_0$ is the prefactor. The circles, triangles and squares represent the experimental data while the dashed and dash-dotted lines represent the theoretical data for the $C_2^{\parallel}$ and $C_3$ type rotations, respectively. The shaded area represents characteristic times of the range $0.1 - 1.0\,\mathrm{eV}$ with a barrier of $0.1\,\mathrm{eV}$.

**Figure 5.5:** The main results for $\beta$-$Mg(BH_4)_2$.

It is unsurprising to find that there is a direct relationship between $L$ and the $C_2^{\parallel}$ barrier height. In fact the relationship is linear, as can be seen in figure 5.5(a) the barrier increases with increased $L$ which is most likely due to more H-Mg interaction. Some of the $C_2$-type rotations showed a very shallow intermediate minimum ($\sim 4 \times 10^{-3}\,\mathrm{eV}$), associated with a slight stabilisation as $L$ decreased during the rotation.

Conversely, no such direct relationship can be seen for the $C_3$ axes, which were all found to be considerably higher in energy than the $C_2^{\parallel}$ axes. This is likely due to the relatively constant $d_{H-Mg}$ for the $C_2^{\parallel}$ rotation, while during the $C_3$ rotations $d_{H-Mg}$ varies more and is, generally, lower, resulting in higher potential energy (figure 5.4).

Figure 5.5(b) shows that the theoretical results (HTST reaction rates) form a distribution in which the experimental results fit rather well. The $C_3$-type rotations correspond to one of the experimentally observed events, while the $C_2$-type rotations correspond to the other two. The experimental results indicated that ~15% of the hydrogen would move at a lower temperature than the others which is consistent with the lowest theoretical barrier which applied to 12.5%

of the hydrogen (1/8th as can be seen table 1 of paper B).

## 5.5 Summary

Collaboration between experimental work and theoretical work was able to produce a convincing image of the low temperature rotational hydrogen motion in two borohydrides, $Ca(BH_4)_2$ and $Mg(BH_4)_2$ — both of which have very high hydrogen capacity — a task hindered by the scarcity of appropriate experiments. Furthermore, low temperature $H_2$ interstitial diffusion in $Ca(BH_4)_2$ is suspected to occur but the scarcity of experimental data hindered anything beyond reasonable speculations.

When considering systems of events of such a different nature, such as rotational diffusion on the one hand and long range diffusion on the other, lead to thoughts on what actually separates the similar events, in this case the rotational diffusion events. The PESes give some indication as to what sort of $SP_2$ lies in between the $SP_1$s but as with the MEPs, the rigid rotation barriers are insufficient. Thus was born the idea to find the $SP_2$ exactly, using a NEB type method, and this effort will be discussed in detail in chapter 6 and Paper C.

Chapter 6

# Ridge Mapping

*In this chapter, the methodology part of paper C is first summarised and then expanded on before offering an outlook and specific suggestions for further development.*

## 6.1 Introduction

A collection of two steepest descent paths starting infinitesimally close to a $SP_2$ and ending at two neighbouring $SP_1$s can be considered a ridge (see figure 2.3). Such a path is non-trivial to find. Some information about the curvature, the Hessian, is essential but often unavailable in a direct manner.

A given point, $\mathbf{R}$, is located on a ridge if the gradient is parallel with its tangent and the Hessian matrix for the vector space perpendicular to the tangent has a single negative eigenvalue [1].

A method for iteratively aligning a path with the ridge is presented, building on the well established NEB (section 4.3) and Dimer (section 4.2) methods. This method is then applied to the self diffusion of an adatom on the Al(100) surface in chapter 7.

After converging to the ridge, the validity of the harmonic approximation to transition state theory (HTST) is considered and an improvement to the reaction rate estimate offered.

## 6.2 Ridge Mapping

Given a function, $E$, of multiple variables, $\mathbf{R}$, its gradient, $\nabla E(\mathbf{R})$, and two $SP_1$s, the goal is to identify a path that lies close to the ridge between the $SP_1$s. The path should, in particular, lie through any intermediate $SP_2$s so that a comparison of their height with respect to the endpoints can be made. The

[1] Higher order "ridges" can be identified if the Hessian has more negative eigenvalues.

method should, furthermore, lead to the identification of previously unknown $SP_1$(s) on the ridge in between the given end points, should they exist.

### Gradient Modification

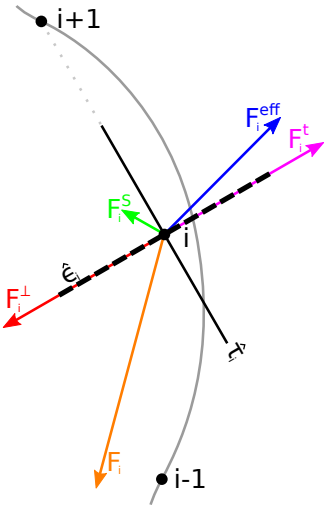


**Figure 6.1:** The construction of the effective force, $\mathbf{F}_i^{\text{eff}}$, which acts on image $i$ of the path and is used in the iterative optimisation. The solid grey line indicates the ridge, the black filled circles represent the current location of three adjacent images, the black solid line shows the tangent estimate, $\hat{\boldsymbol{\tau}}_i$ and the black dashed line shows the minimum mode estimate, $\hat{\mathbf{e}}_i$. The orange arrow shows the gradient force, $\mathbf{F}_i = -\nabla E$. The red arrow shows the transformed force, $\mathbf{F}^t$ (equation (6.3)). The purple arrow shows $\mathbf{F}_i^\perp$, the transformed force(equation (6.3)), The green arrow shows $\mathbf{F}_i^{\text{S}}$ (equation (6.5)), The blue arrow shows $\mathbf{F}_i^{\text{eff}}$ (equation (6.6)). Due to the limited dimensionality of the figure, $\mathbf{F}_i^\perp$ and $\mathbf{F}_i^{\text{t}}$ appear to be parallel to $\hat{\mathbf{e}}_i$, but this is generally not the case for real systems.

Similarly to the NEB method [97] (section 4.3), a path of $N$ discrete images, $[\mathbf{R}_0, \mathbf{R}_1, \ldots, \mathbf{R}_N]$, is iteratively aligned with the ridge by modifying the gradient or force, $\mathbf{F}_i \equiv -\nabla E(\mathbf{R}_i)$, for each one. However, unlike the NEB method, further force modifications are needed, in order to converge to a ridge rather than a MEP.

The path is at each image defined by its tangent, $\hat{\boldsymbol{\tau}}_i$, and in order for the path to be at a SDP (such as the ridge), any force components perpendicular to it,

$$\mathbf{F}_i^\perp \equiv \mathbf{F}_i - (\mathbf{F}_i \cdot \hat{\boldsymbol{\tau}}_i)\hat{\boldsymbol{\tau}}_i, \tag{6.1}$$

must be zero,

$$\mathbf{F}_{\text{ridge}}^\perp = \mathbf{0}. \tag{6.2}$$

Furthermore, one negative eigenvalue of the Hessian, perpendicular to the path, must be guaranteed. The Dimer methodology [61, 92] (section 4.2) for finding the lowest eigenvalue and the corresponding eigenvector (minimum mode) of the Hessian, $\hat{\mathbf{e}}_i$, can produce a transformed force,

$$\mathbf{F}_i^{\text{t}} = \mathbf{F}_i^\perp - 2(\mathbf{F}_i^\perp \cdot \hat{\mathbf{e}}_i)\hat{\mathbf{e}}_i, \tag{6.3}$$

that will map concave degrees of freedom to convex ones, effectively making the ridge appear as a MEP with regards to the gradient. Since eigenvectors are not necessarily perpendicular to the ridge (as can be seen in figure 1 of paper C),

the path itself must be left out of the Hessian's vector space, thus applying an orthogonality constraint on the minimum mode,

$$\hat{\boldsymbol{\tau}}_i \cdot \hat{\boldsymbol{\epsilon}}_i = 0, \tag{6.4}$$

at all times.

Similarly to the NEB method, an artificial force is employed in order to keep the images equally[2] distributed along the path. For the NEB method this force acts only along the path and is generally referred to as the spring force as it resembles springs connecting the images,

$$\mathbf{F}_i^{\mathrm{S}} = k\left[(\mathbf{R}_{i+1} - \mathbf{R}_i) - (\mathbf{R}_i - \mathbf{R}_{i-1})\right], \tag{6.5}$$

where $k$ is the spring constant, which controls the stiffness of the springs. In the NEB, only the component along the path must be included, however, for ridge calculations retention of the full spring force is necessary due to numerical instabilities which proved to be more prominent in ridge calculations than MEP calculations (see below).

Combining the above forces, $\mathbf{F}_i^{\mathrm{t}}$ and $\mathbf{F}_i^{\mathrm{S}}$, into an effective force (as shown in figure 6.1),

$$\mathbf{F}_i^{\mathrm{eff}} = \mathbf{F}_i^{\mathrm{t}} + \mathbf{F}_i^{\mathrm{S}}, \tag{6.6}$$

will allow the path to converge close to the ridge.

### Exact Convergence to the $\mathrm{SP}_2$

Beyond the problems already discussed regarding converging exactly to the $\mathrm{SP}_1$ in NEB calculations, systematic errors due to the retention of the full spring force makes it unlikely that using only equation (6.6) will yield an image at the exact $\mathrm{SP}_2$. As with the NEB method a Dimer-type solution is possible — similar to equations 4.6 and 4.15 — where the highest value image is decoupled from the springs, forming the so-called climbing image, and force components along the *two* lowest eigenvalued eigenmodes, as defined by the minimum mode and the tangent,

$$\mathbf{F}_{i_{\max}}^{\mathrm{eff}} = \mathbf{F}_{i_{\max}} - 2(\mathbf{F}_{i_{\max}} \cdot \hat{\boldsymbol{\tau}}_{i_{\max}})\hat{\boldsymbol{\tau}}_{i_{\max}} - 2(\mathbf{F}_{i_{\max}} \cdot \hat{\boldsymbol{\epsilon}}_{i_{\max}})\hat{\boldsymbol{\epsilon}}_{i_{\max}}, \tag{6.7}$$

where $i_{\max}$ refers to the image with the highest functional value.

The introduction of the climbing image ensures convergence to the highest $\mathrm{SP}_2$ along the ridge, analogous to the convergence to the $\mathrm{SP}_1$ in an NEB calculation. However, in the ridge calculation it additionally reduces the corner cutting of the path in the neighbourhood of the $\mathrm{SP}_2$. The added computational effort involved with the climbing image calculation is, therefore, not easy to measure in the case of the ridge calculation since it affects the extent to which the path

[2] Or with controlled spacing

converges to the ridge. Furthermore, this addition can not be considered optional, as it can technically for NEB, since it serves as an indirect stabilisation tool at the top of the path, where the environment is concave in 2 dimensions rather than 1 as is the case with a MEP.

### 6.2.1 Numerical Instabilities

#### The Orthogonality Constraint

Simply using the Dimer, or any other non-exact, estimate of the minimum mode introduces instabilities in the forces, as the ridge→MEP mapping can get inaccurate. This is not a problem hindering convergence, directly, since the Dimer generally has ample time to converge to the nearly exact minimum mode during the iterative convergence.

More serious seems to be the interaction between the minimum mode and the tangent, as enforced by equation (6.4). The tangent is designed to minimise numerical instabilities in the NEB [98] but not to offer a particularly good estimate of the path's tangent at any given time, however, once converged, it offers a reasonably good estimate[3] and in the limit of infinite amount of images, an exact tangent. Using a tangent that depends on both neighbouring images, the path would form kinks under minute perturbations that would not even out with more iterations. The orthogonality constraint (equation (6.4)) propagates a similar error in the minimum mode estimate under perturbations to the path. This, in turn, introduces similar instabilities as the kinks, when the ridge→MEP mapping becomes inaccurate (figure 6.2(a)). Preliminary testing showed that this is not a problem where individual degrees of freedom were decoupled (non-interacting) but for systems where all degrees of freedom interact (most systems) such instabilities are problematic and common.

In paper C, these instabilities are reduced by the inclusion of the perpendicular spring force component which yields the more systematic error of corner cutting (discussed below). Further analysis showed that enforcing the orthogonality constraint (equation (6.4)) using a tangent estimate that is focused on accuracy, rather than stability, reduces the problematic behaviour (figure 6.2(b)). The system would then have two tangent definitions co-existing, a numerically stable one for the NEB-type force scheme (equation (6.1)) and a more accurate representation of the ridge,

$$\hat{\boldsymbol{\tau}}_i^{\text{ridge}} = \frac{\mathbf{R}_{i+1} - \mathbf{R}_{i-1}}{|\mathbf{R}_{i+1} - \mathbf{R}_{i-1}|}, \tag{6.8}$$

for the projection of the Hessian (equation (6.4)). This latter scheme was neither employed in paper C nor chapter 7 and has not been tested fully. Nevertheless, the initial results are promising for the removal/reduction of corner cutting.

[3] A better estimate of the steepest descent path in question (the minimum energy path) would be a tangent pointing downwards rather than upwards.

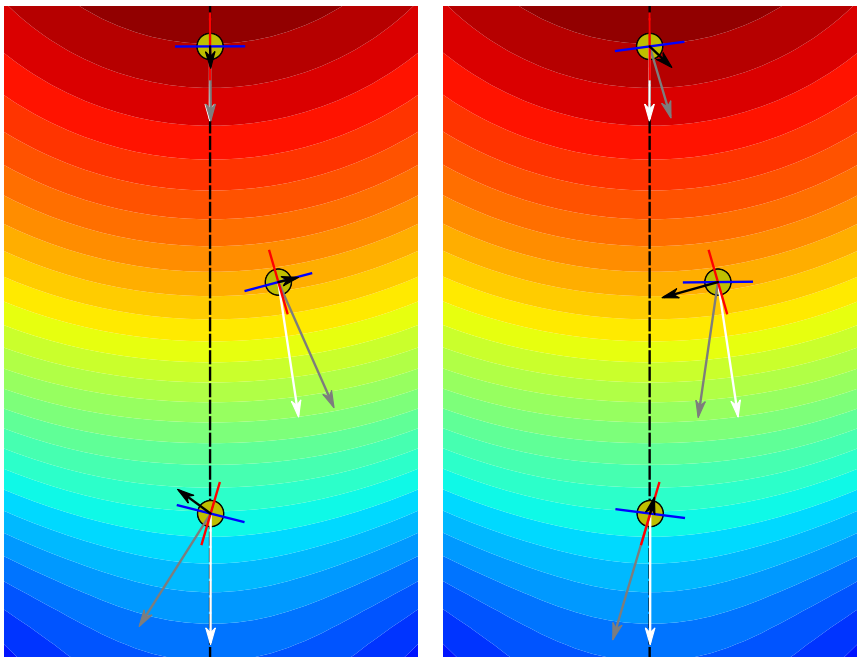

(a) The higher-image tangent is used for the orthogonality constraint of the minimum mode.

(b) A central difference tangent is used for the orthogonality constraint of the minimum mode.

**Figure 6.2:** The ridge is the black dashed line. The white arrows are the PES force, the grey arrows are the dimer transformed forces and the black arrows are the effective forces. The red line is the higher-image tangent and the blue line is the minimum mode estimate. The system is a frozen 1 layer Al(100) "slab" with a free to move Al adatom, modelled with EMT [62] and the ridge is that between two neighbouring hop $SP_1$s. The PES is created by relaxing the adatom in the direction perpendicular to the frozen layer. Shown are the in-plane components of the forces and vectors. The out-of-plane components for all are very small.

Figure 6.2 demonstrates the problem and suggested solution. However, the problem seems to be system specific and dependant on, at least, the curvature of the contour lines. In order to fully understand the root cause of these instabilities, more research on more test systems is required but using the tangent from equation (6.8) seems to be a vital step. In fact, the test cases considered would generally converge to the exact ridge without the use of the perpendicular spring force if started from a path that had been converged with the full spring

force. This was not the case for all systems test but those with only mild corner cutting would all converge.

### Non-barrier profiles

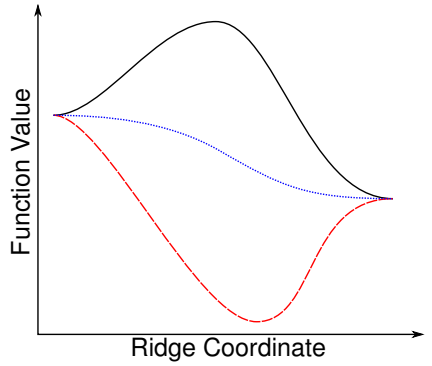


**Figure 6.3:** A schematic of some of the possible initial energy profiles of a ridge calculation. A barrier (black, solid), a monotonic decrease (blue, dotted) and an inverted barrier (red, dashed). Only the first is possible in NEB calculations.

Since the end points of the ridge are not local minima, there is no intrinsic barrier separating them, as is the case for NEB calculations. In fact, the initial profile can have any shape, including a monotonic one or even an inverted barrier, if it lies near a local minimum, which is *not* unlikely, examples of which can be seen in figure 6.3. This means that the initial environment of the path is drastically different from that of the ridge. To help bring the path nearer to the ridge, the full spring force was used. Furthermore, the usage of the climbing image becomes questionable as the immobile end images may very well be the highest ones. If using the climbing image from the outset is required, non-highest images must be used as the climbing image. Images numbered 1 and $N-1$ are partially restrained by the immobility of the endpoints, thus images even further in must be used, 2 or $N-2$.

## 6.3 Energy Ridge Mapping

In the context of atomic simulations, the function in question is often the potential energy as a function of all atomic coordinates, or the potential energy surface.

Information about energy ridges can be useful when considering reaction rates, e.g. for checking the validity of the harmonic approximation to TST (section 3.3.2). Furthermore, should HTST not be sufficient it is possible to make adjustments to the rate using information about the ridge. This move beyond harmonicity is discussed below in section 6.3.1, in chapter 7 and paper C.

### 6.3.1 Beyond Harmonicity

The reaction rate offered by the, commonly used, harmonic approximation to transition state theory (section 3.3.2), HTST, assumes two things. First, that the transition state, ‡, can be described with a hyperplane in which the relevant $SP_1$ lies and whose normal is the eigenvector corresponding to the negative eigenvalue of the Hessian at the $SP_1$. Second, that the energy profile at the ‡ and minimum can be approximated with a second degree Taylor expansion. These assumptions make the harmonic approximation faster than full TST by orders of magnitude.

The conditions under which HTST is valid are generally that the energy, $E(\mathbf{R})$, at the minimum of the reactants basin must be sufficiently lower than at the $SP_1$ and that the $SP_1$ energy must be sufficiently lower than the energy at any neighbouring $SP_2$s. The literature is unspecific as to what a sufficient difference is but a commonly used value is that $E(\mathbf{R}_{\mathrm{SP}_1}) - E(\mathbf{R}_{\mathrm{min.}}) > 5k_{\mathrm{B}}T$ [79]. It is reasonable to assume a similar criterion for $E(\mathbf{R}_{\mathrm{SP}_2}) - E(\mathbf{R}_{\mathrm{SP}_1})$.

Ridge calculations can be used to check if this criterion is fulfilled but further, they can be used to improve the reaction rate. By comparing the configurational integral of the harmonic energy profile for a given degree of freedom,

$$Z_{\ddagger}^{\mathrm{harm.}} = \int_{-\infty}^{\infty} e^{-\alpha x^2/k_{\mathrm{B}}T} dx, \tag{6.9}$$

to that of the ridge,

$$Z_{\ddagger}^{\mathrm{ridge}} = \int_{\mathrm{ridge}} e^{-E(x)/k_{\mathrm{B}}T} dx, \tag{6.10}$$

where x is the displacement along the particular degree of freedom under investigation and $\alpha$ is the corresponding Taylor coefficient, corrections can be made to the reaction rate. The ratio of the configrational integrals,

$$\Gamma = \frac{Z_{\ddagger}^{\mathrm{ridge}}}{Z_{\ddagger}^{\mathrm{harm.}}}, \tag{6.11}$$

can be used as a multiplicative correction factor to the harmonic reaction rate,

$$k_{\mathrm{HTST}}^{\mathrm{corrected}} = \Gamma k_{\mathrm{HTST}}, \tag{6.12}$$

for each investigated degree of freedom.

Since the harmonic integral has a larger range, $[-\infty, \infty]$, than the ridge integral, $[\mathrm{SP}_2^{\mathrm{A}}, \mathrm{SP}_2^{\mathrm{B}}]$, it is possible for the ratio to become larger than 1.0. Such ratios are artefacts and should not be used to increase the reaction rate. It is possible to limit the harmonic integral to the same range as the ridge integral, using the error function, to avoid this. In the tests presented in chapter 7, $\Gamma > 1.0$ was not a common nor large problem compared with the factors where $\Gamma < 1.0$ and thus the infinite limits were used.

Choosing the direction of $x$ is non-trivial. In the work presented in chapter 7, it is implicitly chosen when $\alpha$ is prepared by means of a least squares analysis of the 4 lowest energy images of the ridge. Another method would be to use the tangent of the ridge at the $SP_1$ in question to extract the corresponding vibrational frequency from the Hessian but this method was neither tried nor tested. In general, the accuracy of $\Gamma$ is not essential as it can only offer a rough correction estimate rather than a rigorous correction to HTST.

## 6.4 Corner Cutting

Should finding the exact ridge be the goal — rather than just the $SP_2$ and a ridge estimate — and the alternative tangent discussed above not be sufficient, multiple strategies can be envisioned, all of which aim at somehow reducing the perpendicular component of the spring force while avoiding or minimising the instabilities discussed above.

**What is corner cutting**

The spring force tries to keep each image as close as possible to its neighbours. Without any further influence, the images would align evenly spaced in a straight line. However, since there are other forces at work, perpendicular to the path, $\mathbf{F}^{\mathrm{t}}$, an equilibrium between the conflicting forces will be reached, when they are equal in length but with opposite direction,

$$\mathbf{F}^{\mathrm{S}\perp} = -\mathbf{F}^{\mathrm{t}}, \tag{6.13}$$

producing a systematic error which is commonly referred to as corner cutting as seen in figure 6.4. Since the goal of the whole method is to fulfil equation (6.2), such an equilibrium can be unsatisfactory.

This problem existed in the infancy of NEB calculations but was made a thing of the past with more numerically suitable tangent and spring force definitions [98]. These changes are not directly applicable to ridge calculations due to intrinsic stability issues which are dampened by the perpendicular component of the spring force. However, once the path is sufficiently well behaving and near the ridge, minimising the corner cutting could be done.

### 6.4.1 Minimise corner cutting

*After publishing paper C some effort went into finding the exact ridge instead of paths that suffer from corner cutting. The methods and ideas presented here serve more as a detailed outlook for future work than a complete study.*

In order to reduce/remove corner cutting, the perpendicular component of the spring force must be removed/reduced at each image. Then in tune with

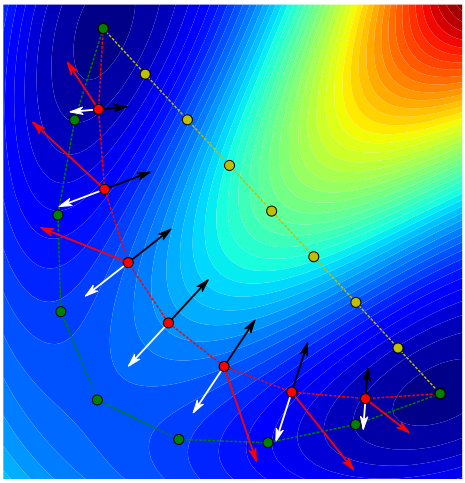

**Figure 6.4:** An example of corner cutting. The yellow path is the initial linear interpolation on which the spring forces are zero (since it is the shortest possible path) and the green path is the converged MEP without any perpendicular spring force components. The red path has converged to an equilibrium between the perpendicular components of the spring force (black arrows) and PES force (white arrows). The red arrows are the full PES force. High potential areas are red and low potential areas are blue.

the equilibrium presented in equation (6.13), equation (6.2) will be fulfilled and the exact ridge found.

Using the dual tangent scheme, presented above, it is possible to significantly reduce the numerical instabilities of the ridge calculation. In some test cases even allowing for the complete exclusion of the perpendicular spring force after turning on the climbing image. However, should this not be possible, a multiplication factor, $\xi_i \in [0, 1)$, for the perpendicular spring force,

$$\mathbf{F}_i^{\mathrm{S}\perp} = \mathbf{F}_i^{\mathrm{S}} - (\mathbf{F}_i^{\mathrm{S}} \cdot \hat{\boldsymbol{\tau}}_i)\hat{\boldsymbol{\tau}}_i, \tag{6.14}$$

can be defined,

$$\mathbf{F}_i^{\mathrm{S,\ eff.}\perp} = \xi_i \mathbf{F}_i^{\mathrm{S},\perp}, \tag{6.15}$$

to iteratively bring the effective perpendicular component, $\mathbf{F}_i^{\mathrm{S,\ eff.}\perp}$, to zero and thus converging to the exact ridge.

Multiple schemes for reducing $\xi_i$ can be envisioned. One, that initial testing showed to be successful, is reducing $\xi_i$ each time corner cutting is detected and then continuing the iterative convergence until either corner cutting is detected again or the path is fully converged to the ridge. By how much $\xi_i$ is reduced each time, could either be a fixed ratio or, preferably, dependant on the amount of corner cutting.[4] In order for the path to converge evenly, $\xi_i$ must be restricted to be of a similar magnitude as $\xi_{i-1}$ and $\xi_{i+1}$. Using a scheme such as this, the corner cutting was significantly reduced in the test systems it was applied to.

It warrants repeating that the ridge method, as presented originally in paper C, is able to find the $SP_2$ exactly without problem but if the ridge is curved, corner cutting will take place, except near the $SP_2$. While the removal of corner

[4] Only the fixed ratio scheme was tested.

cutting would present a truer picture of the ridge, the method as it stood is still of good use.

Chapter 7

# Self Diffusion of Aluminium

*In this chapter, a look at the self-diffusion barriers of Al(100) is presented. Summarising the second half of paper C.*

## 7.1 Introduction

An Al adatom on the Al(100) surface provides an interesting system to study. Several different low energy diffusion mechanisms have been found, including various concerted displacements of two or more atoms, in addition to the, more intuitive, hop mechanism [61, 86, 117]. The dimer method, on which the current implementation of ridge calculations heavily depends, has been used successfully on the system [61], using the well tuned and fast embedded atom method (section 2.4) [58, 60]. This made the system an excellent candidate for trying the newly implemented ridge method (chapter 6, paper C).

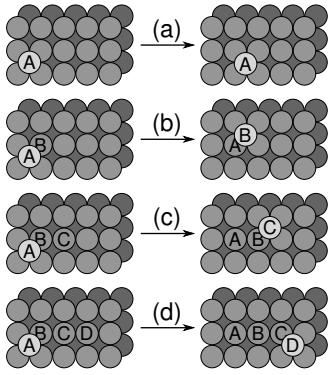


**Figure 7.1:** A schematic of the processes that are being considered. (a) is the hop over a ridge. (b) is the concerted displacement of two atoms, where the adatom, A, burrows into the surface and the surface atom, B, emerges at a different site. (c) is the concerted displacement of three atoms. Similarly to (b), A burrows into the surface but B does not emerge as it moves into the surface site of C, which in turn emerges at an even further site. (d) is the concerted displacement of four atoms. Similar to (c) but an extra surface atom, D, takes part as well and emerges still further away.

The obvious hop-over-ridge ($E_\mathrm{b} = 0.372\,\mathrm{eV}$) is not the lowest energy diffusion mechanism. Considerably lower in energy is the concerted motion of 2 atoms, where the adatom burrows into the surface to replace an atom which in turn

pops out of the surface at a neighbouring site. This mechanism has a barrier of $E_b = 0.227\,\text{eV}$. Related to the concerted 2 atom mechanism are the concerted 3 atom ($E_b = 0.426\,\text{eV}$) and concerted 4 atom ($E_b = 0.413\,\text{eV}$) mechanisms, where more surface atoms take part in the concerted mechanism. These latter diffusional mechanisms are of a noticeably longer range than the hop — and to a lesser extent the concerted 2 atom mechanism — as the surface atom that "pops" up, does so in a more distant site. All the processes under consideration are shown schematically in figure 7.1.

Of course, there is an incredible amount of mechanisms possible for the 385 atom system of 771 degrees of freedom[1]. However, only these lowest ones were considered for the current study as they are the most relevant when considering the real-world diffusion and present a challenging enough task for the ridge method. The long-range concerted mechanisms are difficult to locate due to their environment being very flat, thus investigating the ridges lying close by is an interesting subject, with a high possibility of seeing low energy $SP_2$s in the vicinity of the $SP_1$s. Furthermore, there is a clear separation in geometry between the hop mechanism on the one hand and the concerted displacements on the other, giving a similar situation as the one presented in section 5.5.

## 7.2 Energy Ridges

The energy ridges between all the lowest energy $SP_1$s were calculated. Two situations of particular interest arose. The first was the discovery of intermediate $SP_1$s, while the second concerned the HTST reaction rate, its accuracy and efforts to improve it.

### Intermediate $SP_1$s

As can be seen in figure 7.2 there is a significant energy ridge "barrier" separating the hop and concerted 2 atom $SP_1$s. More interestingly, ridge calculations between the more populous concerted $SP_1$s (3 and 4 atom) and the hop revealed that they were interspersed with the concerted 2 atom $SP_1$. This is not surprising as the concerted mechanisms are all quite similar with regards to their coordinates, while the hop mechanism is inherently different, as can be seen in insets of figures 7.2 and 7.4.

Finding the intermediate $SP_1$ is only accurate in the limit of an infinite amount of images and no corner cutting, but the lowest energy image gives a good starting guess, both for the coordinates and the minimum mode, for traditional $SP_1$ methods, such as the Dimer. It would be possible to implement a "sinking" image alteration of the effective force in a manner similar to the

[1] The calculational cell was composed of 2 frozen layers and 4 free layers of $8 \times 8$ atoms with a single adatom on top. For further calculational parameters, please refer to section 3 of paper C.

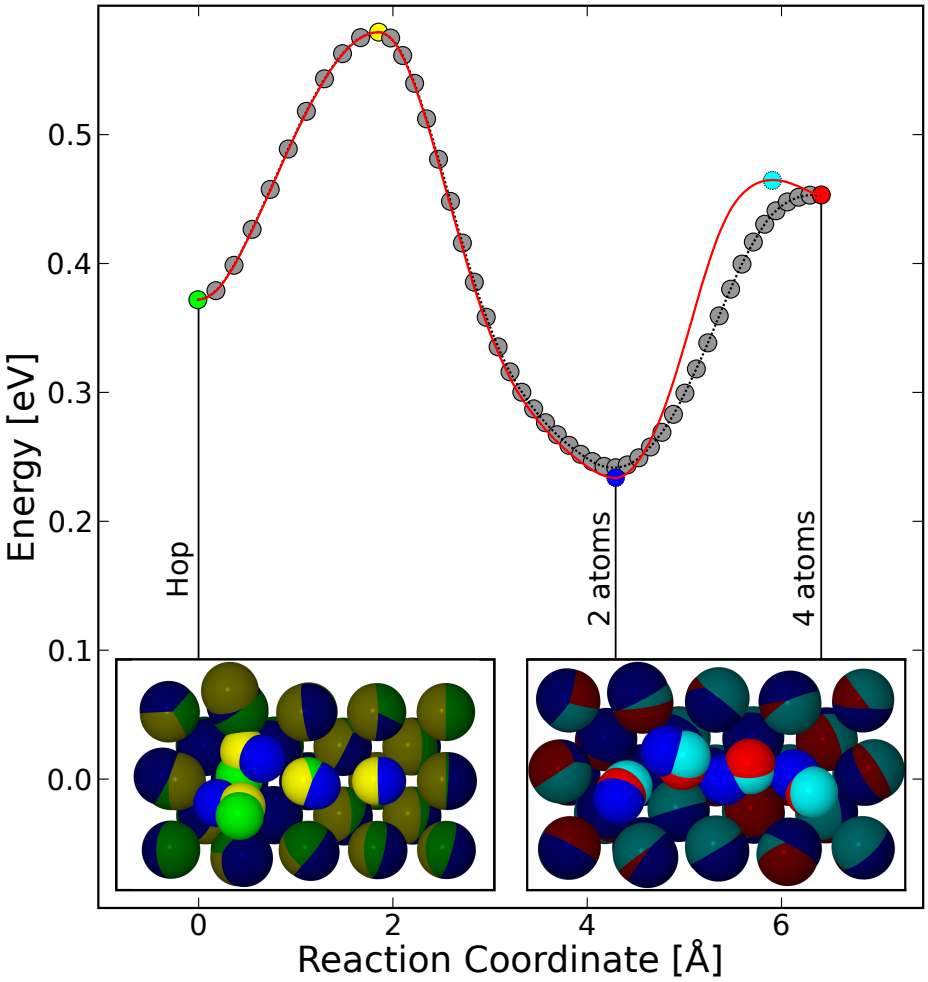


**Figure 7.2:** Calculated path at the ridge between the $SP_1$s for a hop and concerted 4-atom displacement. The circles show the position of converged images (coloured circles for $SP_1$s and $SP_2$s, but grey for the rest). These $SP_1$s turned out not to be adjacent on a ridge and the path optimisation reveals an intermediate $SP_1$, the one for the concerted 2-atom displacement. The full path is not able to accurately locate the intermediate $SP_1$ and the lower energy $SP_2$ due to finite resolution in the discretisation and corner-cutting (grey circles). The exact configuration of the $SP_1$ can be found using a $SP_1$ finding algorithm starting with the approximation obtained from the optimised path. Then, a calculation of a shorter path (red line), between the $SP_1$s of the 2-atom and 4-atom displacements, locates the intermediate $SP_2$ accurately (cyan circle). The insets show an overlay of three configurations, two adjacent $SP_1$s and the intermediate $SP_2$. The atom colours correspond to the coloured spheres of the energy ridge.

climbing image but this was not done here. Similarly, corner cutting prevents rigorous convergence to the lower energy $SP_2$. A second climbing image would converge exactly to this point but this was not done.[2] However, performing a second ridge calculation with the intermediate $SP_1$(s) as end points yields the exact $SP_1$ and, apart from the possible corner cutting, the ridge. These latter paths are displayed as red curves in figure 7.2

### Beyond Harmonicity

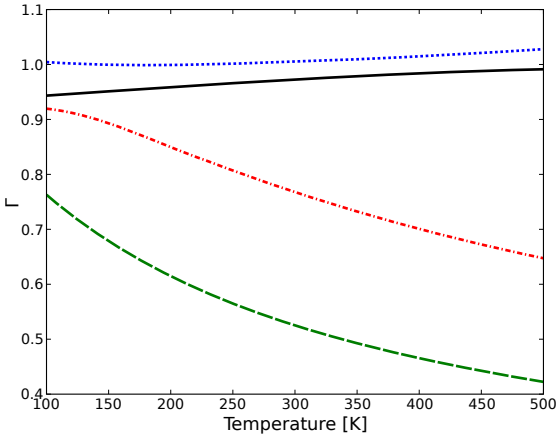


**Figure 7.3:** The harmonic correction ratio, Γ, defined in equation (6.11), between the configuration integrals of the potential energy ridge shown in figure 7.4 and the corresponding harmonic approximations. The lines represent the ratio for individual processes: concerted 2 atom (blue, dotted), 3 atom (green, dashed), 4 atom (red, dash-dotted) and the combined ratio for all the processes combined (black, solid).

The ridges between the, similar, concerted motion $SP_1$s are shown in figure 7.4. It can be clearly seen that applying HTST to the concerted 3 and 4 atom $SP_1$s is highly questionable as their neighbouring $SP_2$s are very low, ~0.005 eV and 0.012 eV, certainly lower than the $5k_BT$ rule of thumb.[3] However, applying HTST to the concerted 2 atom mechanism is more justified, by visual inspection the ridge is fairly near harmonicity up to the $5k_BT = 0.128$ eV limit at room temperature and the $SP_2$s are still higher. Figure 7.3 further shows that the concerted 2 atom rate has a correction factor, Γ, of approximately 1.0 throughout the temperature range while the concerted 3 and 4 atom mechanisms have significant correction factors at all temperatures.

It might appear wise to rigorously calculate such a correction factor for all the degrees of freedom until one considers the complexity of such an exercise. Figure 6 in paper C makes an effort to put into context the abundance of ridges on which each $SP_1$ lies but, of course, fails to do so properly due to the immense dimensionality (771 degrees of freedom) of the PES. Not only finding all the $SP_1$s leading out of a given basin but also finding all neighbouring $SP_2$s and ridges for

[2] Implementing multiple climbing or sinking images is in principle not difficult but the ramifications could be dire, e.g. in systems with rugged landscapes and a limited amount of images.

[3] At any temperature above 9 K and 28 K respectively.

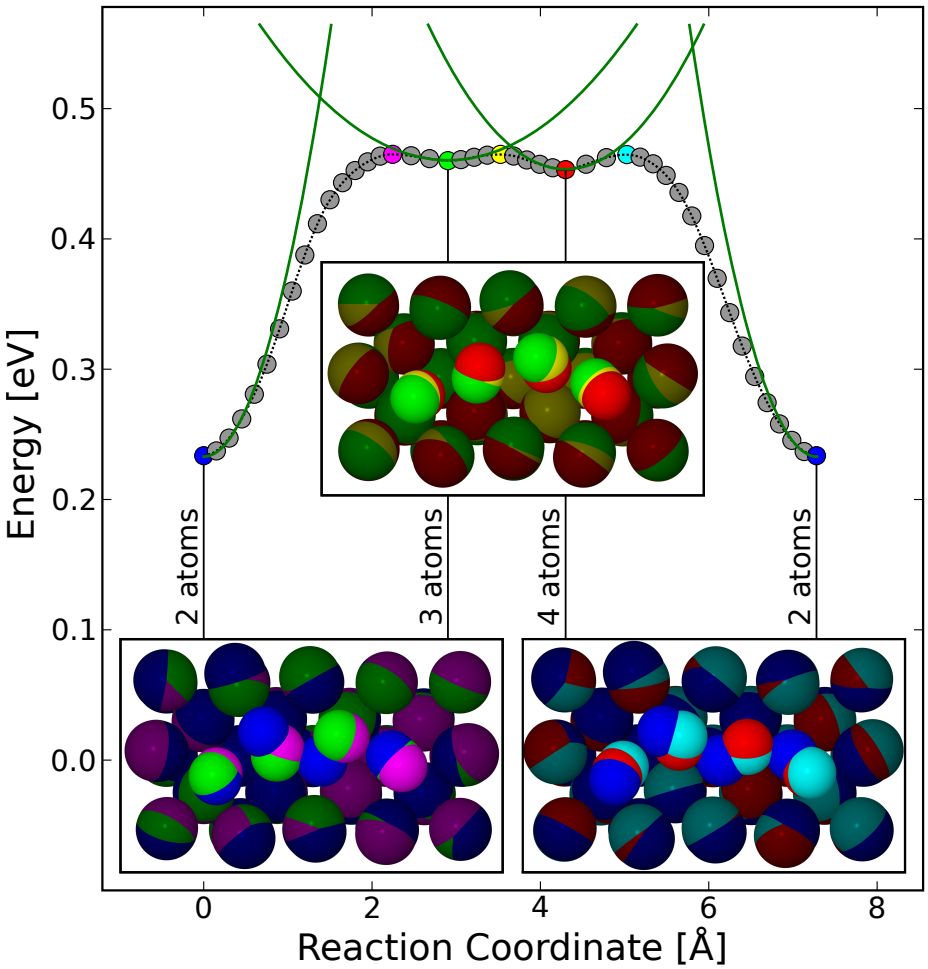


**Figure 7.4:** The energy ridge going through $SP_1$s of 2-atom, 3-atom, 4-atom and, then the same, 2-atom concerted displacement. The circles represent the position of images in the optimised paths, the $SP_1$s and the $SP_2$s being coloured differently but the rest coloured grey. The green curves represent harmonic approximations to the energy surface at each $SP_1$. The insets show an overlay of three configurations, two adjacent $SP_1$s and the intermediate $SP_2$. The atom colours correspond to the coloured spheres of the energy ridge.

each one would be folly due to the sheer amount of possible SPs. Furthermore, as stated when introducing the correction factor (equation (6.11)), $\Gamma$ is not a rigorous correction factor and should not be used as such. However, using the ridge to calculate a more precise reaction rate, outside the HTST framework, seems appropriate and will make an interesting subject for future research.

Chapter 8

# Coupled Hydrogen Defects in Perovskites

*This chapter describes the initial testing of the ridge mapping method for a complex energy landscape with DFT forces.*

## 8.1 Introduction

As a DFT test case for the ridge mapping method, the $SrTiO_3$ perovskite system was chosen, partly due to general interest in its properties and partly due to familiarity, as it was the one of the subject of a recent Ph.D. thesis [118].

Perovskites have potential in a number of fields and active research is, for example, being done on proton transport processes [119, 120] for use in solid oxide fuel cell electrolytes, that allows protons to pass[121]. Other than this, perovskites are used in a number of applications, such as electrodes, semiconductors and solar cells.

The system under study in this chapter is the newly discovered double hydrogen defect in $SrTiO_3$ [89]. It has been found that the double defect can be more stable than an isolated one and that coupled motion of the pair can be marginally faster than that of a single atom. In this chapter the system serves as a complex real-world application test of the ridge mapping method. Briefly touching on the initial efforts to apply the ridge mapping method to noisy (DFT) forces, neither a comprehensive study is presented nor a detailed look at the system in question.

As for a more detailed information to perovskites, the reader must refer to the citations in this intoduction.

## 8.2 Results and Discussion

### 8.2.1 Calculational Parameters

The GPAW [14] DFT implementation was used with the same parameters as used in [89]. Except that a tighter convergence criteria ($10^{-6}$ eV) for the electronic structure was used in order to reduce numerical noise. The calculational supercell consisted of 2x2x2 formula units of $SrTiO_3$ with a lattice constant of 3.931 Å. For further details refer to [89].

#### Dimer Parameters

The separation of the dimer images was set at $\Delta_D = 0.001$ Å and only one rotation per iteration was allowed, none if the rotational force was below 0.1 eV/Å. When determining the initial minimum modes and displacement away from minima, the defect hydrogen atoms were displaced using a Gaussian distribution with a standard deviation of 0.01 Å in each direction.

### 8.2.2 Searching for Diffusional Mechanisms

The results of [89] showed that the hydrogen atoms would move in individual steps while staying close to each other in order to minimise the elastic energy of the lattice. Two such mechanisms were discussed and both consisted of multiple iterations of two types of events. Either the transitioning hydrogen atom would "jump" from one oxygen atom to the next near a titanium atom (as seen for atom A in figure 8.1(a) and 8.2(a)) or it would "rotate" past a strontium atom while remaining near the same oxygen atom (as seen for atom B in figure 8.2(a)). Both hydrogen atoms would perform these steps — often in alternating order — while remaining in close proximity of each other, to diffuse through the system.

Dimer $SP_1$ searches were conducted, starting from the various minima suggested in [89]. Essentially, confirming the previous results, the low energy $SP_1$s were all events of the types described above. Only a handful of truly concerted events, where both hydrogen atoms would transition simultaneously, were detected but they were all higher in energy.

Some $SP_1$s were found at a slightly longer range, e.g. where the hydrogen atoms would be separated by a strontium atom. In the calculational cell used this is effectively half of its length, bringing into question any discussion on the energies as periodic effects could both over- and underestimate the stabilisation by the neighbouring hydrogen atom. Further investigation of these events might prove interesting but a larger calculational cell is required.

### 8.2.3 DFT Ridge Calculations

The same parameters were used for the dimer part of the ridge calculations as were used for the dimer searches above.

A few ridge calculations were started with some of the $SP_1$s found above as endpoints. The general results can be split into three categories.

- Successful ridge calculations, converged from a linear interpolation to a ridge in under 300 iterations.
- Unsuccessful calculations where the path would spent most of its time as an inverted barrier near the minimum energy path.
- Calculations where a soft eigenmode was followed resulting in a non-converging calculation where the lattice would distort heavily.

### Successful DFT Ridge Calculations

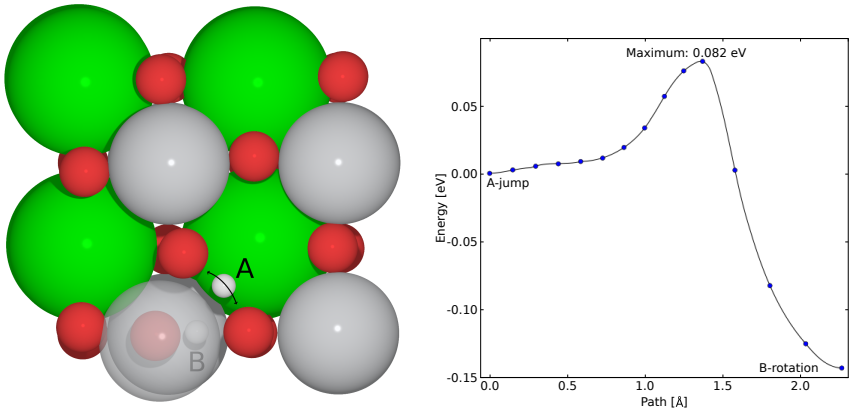


(a) The configuration of the A-jump $SP_1$. One titanium atom is semi-transparent to allow viewing of hydrogen B

(b) Energy profile of the ridge. The $SP_2$ is ~0.08 eV higher than the A-jump $SP_1$

**Figure 8.1:** $SrTiO_3$ with a double hydrogen defect. A successful DFT ridge calculation between a jump $SP_1$ for hydrogen atom A and rotation of hydrogen atom B. The hydrogen atoms are white, the titanium atoms are grey, the strontium atoms are green and the oxygen atoms are red.

The most interesting of the successful ridge calculations was one where the ridge near a jump-type $SP_1$s (figure 8.1(a)) consisted of a rather flat energy profile (figure 8.1(b)) with lattice rearrangement before a sharp rise to reach a 0.08 eV $SP_2$ on its way to a rotation-type $SP_1$ for the other hydrogen atom. A second successful calculation of the ridge near a different jump-type $SP_1$ revealed one other low energy $SP_2$ of 0.08 eV. (figure 8.2) Both the $SP_2$s are on

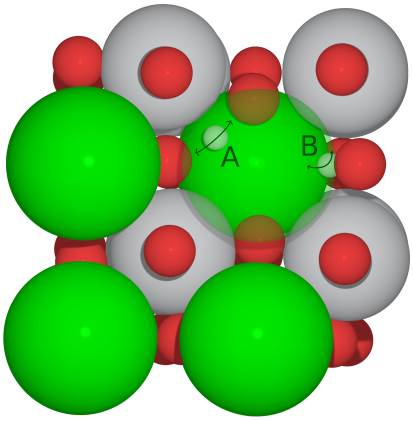


(a) The configuration of the A-jump/B-rotate $SP_2$. One strontium atom removed is semi-transparent to allow viewing of the hydrogen atoms

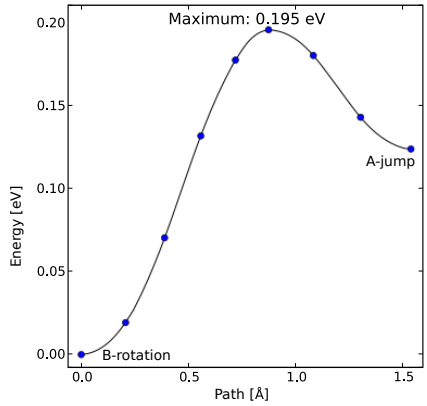


(b) Energy profile of the ridge. The $SP_2$ is ~0.08 eV higher than the A-jump $SP_1$

**Figure 8.2:** $SrTiO_3$ with a double hydrogen defect. A successful DFT ridge calculation between a jump $SP_1$ for hydrogen atom A and rotation of hydrogen atom B. The hydrogen atoms are white, the titanium atoms are grey, the strontium atoms are green and the oxygen atoms are red.

the border of the $5k_BT$ limit. Furthermore, finding multiple low energy $SP_2$s and a flat energy profile are clear warning signs, that the HTST rate could be improved.

From an informal visual inspection of the successful ridge calculations, the initial paths never lay close to a minimum. However, it was not possible to make the opposite claim for the failed calculations.

### Basin Trapped Paths

The calculations that did not reach the ridge, generally lay near the minimum energy path and were not able to escape the basin. The eigenvalue estimate would remain negative for most of the images.

It is unlikely that this minima-trapping behaviour is an artefact of the method itself as such things did not happen in the previous test cases. More likely is that the DFT parameters must be further considered. A significant eggbox effect [54] was seen when relaxing the structures. Even though the dimer searches were not affected in an obvious manner, this could affect the ridge calcualtions, due to the correlated nature of the images. Furthermore, a

rather large gridspacing, 0.2 Å, was used, further reducing the accuracy of the forces. Nevertheless, neither of these can be identified as the cause of the failed calculations without further research.

#### Soft Minimum modes

Latching on to a soft minimum mode is a concern that is always possible with dimer-type algorithms. However, this was not a significant problem in the previous tests. In this particular case, the climbing image had been turned on very early in order to avoid the basin trapping problem. After the climbing image is turned on with a soft minimum mode, the calculation is unlikely to yield an interesting result. This problem raises questions about the initial minimum modes. If a random initial minimum mode is used (as was the case in this calculation), it is likely that neighbouring minimum modes will not be similar (i.e. not find the same ridge). It is of course possible to initialise the minimum modes in a linear fashion, using the unstable modes of the end points or implement some constraint to avoid neighbouring minimum modes from from being dissimilar. In any case, this warrants further consideration.

### 8.2.4 Summary

Neither the dimer searches nor the ridge calculations found new low energy pathways beyond those suggested by [89]. In particular no directly correlated event where both hydrogen atoms moved simultaneously were found. Even though the harmonic description is questionable, it can be concluded that their picture of the diffusion is accurate. Since the low energy $SP_2$s were found near different $SP_1$ for a similar event, it is reasonable to assume that similar $SP_2$s exist near the jump event of an isolated defect. Thus, there is no reason to conclude that the ratio of mobilities is different from the reported one without further ridge calculations in both systems. A coupled defect, albeit uncorrelated, has slightly higher mobility than an isolated one.

Out of 7 ridge calculations, only 3 were successful, while 1 followed a soft minimum mode and 3 were trapped in basins. Despite the failed calculations, there were successful ones which converged to the ridge and the $SP_2$s of a highly complex DFT system. Further testing is, of course, needed to fully understand the flawed calculations.

Chapter 9

# Summary

### Metal Borohydrides

The rotational dynamics of two metal borohydrides were investigated in detail with close collaboration to experimental work. The results of which complemented the experimental results very well.

For $\beta$-$Mg(BH_4)_2$ only rotational events were detected, with roughly 15% of the $BH_4$ groups activating very low energy ($E_b = 0.03\,\text{eV}$) $C_2$-type rotations before the rest activates their $C_2$-type rotations ($E_b = 0.05 - 0.10\,\text{eV}$). This two-fold activation of the $C_2$-type rotations was found to be dependant on the distance between B and its Mg-Mg axis. The $C_3$-type rotations were considerably higher in energy ($E_b = 0.13 - 0.30\,\text{eV}$) and did not show the same dependence as the $C_2$-type rotations.

For $\beta$-$Ca(BH_4)_2$, not only rotational events were detected but also longer range diffusion of hydrogen. The rotational events have activation energies of $0.09\,\text{eV}$ and $0.15\,\text{eV}$ for the $C_3$- and $C_2$-type rotations, respectively. As for the long range diffusion, many processes were considered but the only one with any significant similarities to the, very scarce, experimental data was that of a $H_2$-interstitial.

### Ridge Mapping

In order to map ridges of functions[1] a method was developed. By transforming concave regions into convex ones, the dimer algorithm maps first order saddle points to minima and ridges to minimum energy paths[2] (MEP), with regards to the gradient. Using this transformation to iteratively converge a trial path to the ridge is then achieved using the nudged elastic band (NEB) algorithm

[1] Steepest descent paths between first and second order saddle points.
[2] Or path of least resistance.

for finding minimum energy paths. Due to numerical instabilities, an artificial method for stabilisation was added to the NEB-type part of the algorithm. This stabilisation leads to deviations in the final path — only the path, not the second order saddle point — Efforts to leave out or minimise this stabilisation part of the algorithm were discussed along with a discussion on the reduction of the numerical instabilities introduced by an inaccurate ridge→MEP mapping. However, these discussions lacked proper testing due to insufficient time and can, thus, only be considered as an extended and detailed outlook.

In the context of theoretical reaction rate chemistry, the ridge method was applied to validate the reaction rates offered by the harmonic approximation to transition state theory. Furthermore, in cases where the harmonic approximation was found lacking, a rough correction factor was offered by calculating the ratio between configurational integrals of the ridge and the harmonic energy profile.

For the Al adatom on the Al(100) surface system, the lowest energy mechanisms for diffusion were investigated, the hop over a bridge site and the non-intuitive concerted motion of several atoms, 2, 3 and 4. Calculation of the ridges between each pair showed that the harmonic approximation held its ground for the lowest energy mechanism, the concerted motion of 2 atoms, and the hop, while it was found to be severely lacking for the more populous concerted motion mechanisms. The correction factor for the latter was found to be significant. It was also found that the ridge between the 3 and 4 atom concerted saddle points on the one hand and the hop saddle point on the other, are separated by the 2 atom concerted saddle point. In this way finding novel mechanisms is possible using the ridge method, similarly to how the NEB method locates new minima.

The Al system was modelled with the embedded atom method which offers gradients that are clean from numerical noise. The dimer algorithm requires well behaved gradients since it relies heavily on finite difference methods for estimating derivatives. In order to test this dependence, DFT calculations on the $SrTiO_3$ perovskite system with a coupled hydrogen defect were performed. Due to time restrictions, only a handful of ridge calculations were attempted. Half of which were successful and found 2 low lying $SP_2$s near processes where a hydrogen defect atom would jump between neighbouring oxygen atoms. The other half of the ridge calculations were unsuccessful and the path ended up lying near MEPs instead of ridges. This behaviour is unexplained and requires further research. However, there is no reason to suspect the method itself as the culprit as these flaws were not present in the other test systems.

## 9.1 Outlook

**A More Precise Ridge** A detailed outlook as to further development of the ridge mapping algorithm was presented in chapter 6. Two efforts to reduce corner cutting on the ridge were discussed. First by implementing a dual tangent

scheme in order to minimise instabilities and remove the need for a perpendicular spring force component. A second tangent estimate is introduced, to which the minimum mode would be perpendicular at all times. This second tangent would be a more precise representation of the ridge than the previous tangent which is chosen for numerical stability of the MEP part of the algorithm. The suggested implementation was a central difference one but a more elaborate spline implementation should also be considered. The second attempt to reduce corner cutting was by iteratively removing the perpendicular component of the spring force. It is unclear if this second scheme is needed, should the dual tangent scheme be successful. Both of the schemes were tested on simple systems and showed great promise but further testing and development are needed.

**Transition State Theory** Using the energy ridges to detect anharmonicity is presented in the thesis and a correction factor is even suggested. However, a more complete transition state rate built from the energy profile of the ridge directly is a certainly a worthwhile topic. Furthermore, stitching together a transition state from hyperplanar segments, at each image, normal to the minimum mode is a natural progression. Such a transition state could even be generated in a variational way, where the number of images would serve as the variational parameter.

**DFT Ridges** DFT calculations of ridges were only moderately successful. Investigating the reasons for this is essential for application of the ridge method in production systems.

**Performance** The performance of the ridge method was not investigated in any detail. Subsequently, the performance was not optimised beyond the use of parameters that have worked well with the underlying methods. A full performance study and parameter optimisation should be performed.

**Application** Only a single application was studied in detail. In particular, studies of systems that are less known *a priori* to test the usefulness of the intermediate $SP_1$ detection.

# Bibliography


[1] R., E.; Davidson, *Journal of Computational Physics* **1975**, *17*, 87 – 94.

[2] Hestenes, M. R.; Stiefel, E. *Journal of Research of the National Bureau of Standards* **1952**, *49*, 409–436.

[3] Stillinger, F. H. *Phys. Rev. E* **1999**, *59*, 48–51.

[4] Wang, Y.; Lv, J.; Zhu, L.; Ma, Y. *Phys. Rev. B* **2010**, *82*, 094116.

[5] Wales, D. J.; Scheraga, H. A. *Science* **1999**, *285*, 1368–1372.

[6] Pickard, C. J.; Needs, R. J. *Journal of Physics: Condensed Matter* **2011**, *23*, 053201.

[7] Oganov, A. R.; Glass, C. W. *Journal of Physics: Condensed Matter* **2008**, *20*, 064210.

[8] Kirkpatrick, S.; Gelatt, C. D.; Vecchi, M. P. *Science* **1983**, *220*, 671–680.

[9] Johnston, R. L. *Dalton Transactions* **2003**, *1*, 4193.

[10] Fischer, C. C.; Tibbetts, K. J.; Morgan, D.; Ceder, G. *Nat Mater* **2006**, *5*, 641–646.

[11] Newton, I. *Philosophiae Naturalis Principia Mathematica*; Edmund Halley: London, 1687; Vol. 1; pp 15–44.

[12] Schrödinger, E. *Phys. Rev.* **1926**, *28*, 1049–1070.

[13] Hohenberg, P. and Kohn, W., *Phys. Rev.* **1964**, *136*, B864–B871.

[14] Enkovaara, J. et al. *Journal of Physics: Condensed Matter* **2010**, *22*, 253202.

[15] Hammer, B.; Hansen, L. B.; Nørskov, J. K. *Phys. Rev. B* **1999**, *59*, 7413–7421.

[16] Bai, Z.; Demmel, J.; Dongarra, J.; Ruhe, A.; Van Der Vorst, H. *Templates for the solution of algebraic eigenvalue problems: A Practical Guide*; SIAM, 2000.

[17] Sebastian, K. L. *The Journal of Chemical Physics* **1989**, *90*, 5056–5067.

[18] Carloni, P.; Rothlisberger, U.; Parrinello, M. *Accounts of Chemical Research* **2002**, *35*, 455–464.

[19] Schiøtz, J.; Jacobsen, K. W. *Science* **2003**, *301*, 1357–1359.

[20] Hummelshoj, J. S. et al. *The Journal of Chemical Physics* **2009**, *131*, 014101.

[21] Skúlason, E.; Karlberg, G. S.; Rossmeisl, J.; Bligaard, T.; Greeley, J.; Jónsson, H.; Nørskov, J. K. *Phys. Chem. Chem. Phys.* **2007**, *9*, –.

[22] Tekin, A.; Hummelshoj, J. S.; Jacobsen, H. S.; Sveinbjörnsson, D.; Blanchard, D.; Norskov, J. K.; Vegge, T. *Energy Environ. Sci.* **2010**, *3*, 448–456.

[23] Eyring, H. *The Journal of Chemical Physics* **1935**, *3*, 107–115.

[24] Evans, M. G.; Polanyi, M. *Trans. Faraday Soc.* **1935**, *31*, 875–894.

[25] Wigner, E. *Trans. Faraday Soc.* **1938**, *34*, 678–685.

[26] Wert, C.; Zener, C. *Phys. Rev.* **1949**, *76*, 1169–1175.

[27] Vineyard, G. H. *Journal of Physics and Chemistry of Solids* **1957**, *3*, 121 – 127.

[28] Hänggi, P.; Talkner, P.; Borkovec, M. *Rev. Mod. Phys.* **1990**, *62*, 251–341.

[29] Born, M.; Oppenheimer, R. *Annalen der Physik* **1927**, *389*, 457–484.

[30] Kohn, W. *Rev. Mod. Phys.* **1999**, *71*, 1253–1266.

[31] Mattusch, C. In *The Oxford Handbook of Engineering and Technology in the Classical World*; Oleson, J. P., Ed.; Oxford University Press, 2008; pp 418–438.

[32] Hubbert, M. K. *Drilling and Production Practice* **1956**, *95*, 1–40.

[33] Solomon, S., Qin, D., Manning, M., Chen, Z., Marquis, M., Averyt, K. B., Tignor, M., Miller, H. L., Eds. *Climate Change 2007: The Physical Science Basis*; Cambridge University Press, 2007; p 996.

[34] Nakamori, Y.; Miwa, K.; Ninomiya, A.; Li, H.; Ohba, N.; Towata, S.-i.; Züttel, A.; Orimo, S.-i. *Phys. Rev. B* **2006**, *74*, 045126.

[35] Pople, J. A. *Rev. Mod. Phys.* **1999**, *71*, 1267–1274.

[36] Thomas, L. H. *Mathematical Proceedings of the Cambridge Philosophical Society* **1927**, *23*, 542–548.

[37] Fermi, E. *Rend Accad Naz Lincei* **1927**, *6*, 602–607.

[38] Rayleigh, J. W. *Phil Trans* **1870**, *161*, 77.

[39] Ritz, W. *Journal für die Reine und Angewandte Mathematik (Crelle's Journal)* **1909**, *135*, 1–61.

[40] Kohn, W.; Sham, L. J. *Phys. Rev.* **1965**, *140*, A1133–A1138.

[41] Hartree, D. R. *Mathematical Proceedings of the Cambridge Philosophical Society* **1928**, *24*, 89–110.

[42] Ceperley, D. M.; Alder, B. J. *Phys. Rev. Lett.* **1980**, *45*, 566–569.

[43] Kobayashi, K.; Kurita, N.; Kumahora, H.; Tago, K. *Phys. Rev. A* **1991**, *43*, 5810–5813.

[44] Kobayashi, K.; Kurita, N.; Kumahora, H.; Tago, K.; Ozawa, K. *Phys. Rev. B* **1992**, *45*, 13690–13693.

[45] Perdew, J. P.; Yue, W. *Phys. Rev. B* **1986**, *33*, 8800–8802.

[46] Perdew, J. P.; Burke, K.; Ernzerhof, M. *Phys. Rev. Lett.* **1996**, *77*, 3865–3868.

[47] Becke, A. D. *The Journal of Chemical Physics* **1993**, *98*, 1372–1377.

[48] Kurth, S.; Perdew, J. P.; Blaha, P. *International Journal of Quantum Chemistry* **1999**, *75*, 889–909.

[49] Perdew, J. P.; Schmidt, K. *AIP Conference Proceedings* **2001**, *577*, 1–20.

[50] Tao, J.; Perdew, J. P.; Staroverov, V. N.; Scuseria, G. E. *Phys. Rev. Lett.* **2003**, *91*, 146401.

[51] Perdew, J. P.; Ernzerhof, M.; Burke, K. *The Journal of Chemical Physics* **1996**, *105*, 9982–9985.

[52] Vanderbilt, D. *Phys. Rev. B* **1990**, *41*, 7892–7895.

[53] Blöchl, P. E. *Phys. Rev. B* **1994**, *50*, 17953–17979.

[54] Mortensen, J. J.; Hansen, L. B.; Jacobsen, K. W. *Phys. Rev. B* **2005**, *71*, 035109.

[55] Perdew, J. P.; Wang, Y. *Phys. Rev. B* **1992**, *45*, 13244–13249.

[56] Stillinger, F. H.; Weber, T. A. *Phys. Rev. B* **1985**, *31*, 5262–5271.

[57] Jacobsen, K. W.; Nørskov, J. K.; Puska, M. J. *Phys. Rev. B* **1987**, *35*, 7423–7442.

[58] Daw, M. S.; Baskes, M. I. *Phys. Rev. Lett.* **1983**, *50*, 1285–1288.

[59] Pedersen, A.; Henkelman, G.; Schiøtz, J.; Jónsson, H. *New Journal of Physics* **2009**, *11*, 073034.

[60] Voter, A. F.; Chen, S. P. Accurate Interatomic Potentials for Ni, Al and $Ni_3Al$. 1986.

[61] Henkelman, G.; Jónsson, H. *The Journal of Chemical Physics* **1999**, *111*, 7010–7022.

[62] Jacobsen, K. W.; Stoltze, P.; Nørskov, J. K. *Surface Science* **1996**, *366*, 394 – 402.

[63] Pauli, W. *Die allgemeinen prinzipien der wellenmechanik*; Handbuch der Physik; Springer: Berlin, 1933; Vol. 24; p 162.

[64] Güttinger, P. *Zeitschrift für Physik A Hadrons and Nuclei* **1932**, *73*, 169–184, 10.1007/BF01351211.

[65] Feynman, R. P. *Phys. Rev.* **1939**, *56*, 340–343.

[66] Hellmann, H. *Einführung in die Quantenchemie*; Franz Deuticke: Leipzig, 1937; p 285.

[67] Bitzek, E.; Koskinen, P.; Gähler, F.; Moseler, M.; Gumbsch, P. *Phys. Rev. Lett.* **2006**, *97*, 170201.

[68] Liu, D. C.; Nocedal, J. *Mathematical Programming* **1989**, *45*, 503–528.

[69] Hesse, L. O., *Vorlesungen über analytische geometrie des raumes, insbesondere über oberflächen zweiter ordnung*; Teubner: Leipzig, 1876.

[70] Henkelman, G.; Jóhannesson, G.; Jónsson, H. In *Theoretical Methods in Condensed Phase Chemistry*; Schwartz, S. D., Ed.; Progress in Theoretical Chemistry and Physics; Springer Netherlands, 2002; Vol. 5; pp 269–302.

[71] Sheppard, D.; Henkelman, G. *Journal of Computational Chemistry* **2011**, *32*, 1769–1771.

[72] McQuarrie, D. A. *Quantum chemistry*; Physical Chemistry Series vb. 100; University Science Books, 1983.

[73] Ryckaert, J.-P.; Ciccotti, G.; Berendsen, H. J. *Journal of Computational Physics* **1977**, *23*, 327 – 341.

[74] Andersen, H. C. *Journal of Computational Physics* **1983**, *52*, 24 – 34.

[75] Voter, A. F. *Phys. Rev. Lett.* **1997**, *78*, 3908–3911.

[76] Mills, G.; Schenter, G.; Makarov, D.; Jónsson, H. *Chemical Physics Letters* **1997**, *278*, 91–96.

[77] Mills, G.; Schenter, G. K.; Makarov, D. E.; Jónsson, H. In *Classical and Quantum Dynamics in Condensed Phase Simulations*; Berne, B. J., Ciccotti, G., Coker, D. F., Eds.; World Scientific, 1998; pp 405–421.

[78] Andersson, S.; Nyman, G.; Arnaldsson, A.; Manthe, U.; Jónsson, H. *The Journal of Physical Chemistry A* **2009**, *113*, 4468–4478.

[79] Pollak, E.; Talkner, P. *Chaos* **2005**, *15*, 026116.

[80] Horiuti, J. *Bulletin of the Chemical Society of Japan* **1938**, *13*, 210–216.

[81] Truhlar, D. G.; Garrett, B. C. *Annual Review of Physical Chemistry* **1984**, *35*, 159–189.

[82] Vanden-Eijnden, E.; Tal, F. A. *The Journal of Chemical Physics* **2005**, *123*, 184103.

[83] Keck, J. *Discuss. Faraday Soc.* **1962**, *33*, 173–182.

[84] Chandler, D. *The Journal of Chemical Physics* **1978**, *68*, 2959–2970.

[85] Bennett, C. H. In *Algorithms for Chemical Computations*; E., C. R., Ed.; The American Chemical Society, 1977; Chapter 5, pp 63–97.

[86] Jóhannesson, G. H.; Jónsson, H. *The Journal of Chemical Physics* **2001**, *115*, 9644–9656.

[87] Hoff, J. *Études de dynamique chimique*; Frederik Muller, 1884.

[88] Arrhenius, S. A. *Zeitschrift für Physik Chemique* **1889**, *4*, 226–248.

[89] Bork, N.; Bonanos, N.; Rossmeisl, J.; Vegge, T. *Phys. Chem. Chem. Phys.* **2011**, *13*, 15256–15263.

[90] Pedersen, A.; Hafstein, S. F.; Jónsson, H. *SIAM Journal on Scientific Computing* **2011**, *33*, 633–652.

[91] Heyden, A.; Bell, A. T.; Keil, F. J. *The Journal of Chemical Physics* **2005**, *123*, 224101.

[92] Olsen, R. A.; Kroes, G. J.; Henkelman, G.; Arnaldsson, A.; Jónsson, H. *The Journal of Chemical Physics* **2004**, *121*, 9776–9792.

[93] Kastner, J.; Sherwood, P. *The Journal of Chemical Physics* **2008**, *128*, 014106.

[94] Trygubenko, S. A.; Wales, D. J. *The Journal of Chemical Physics* **2004**, *120*, 2082–2094.

[95] Young, W. M.; Elcock, E. W. *Proceedings of the Physical Society* **1966**, *89*, 735.

[96] Henkelman, G.; Jónsson, H. *The Journal of Chemical Physics* **2001**, *115*, 9657–9666.

[97] Jónsson, H.; Mills, G.; Jacobsen, K. W. Nudged elastic band method for finding minimum energy paths of transitions. 1998.

[98] Henkelman, G.; Jónsson, H. *The Journal of Chemical Physics* **2000**, *113*, 9978–9985.

[99] Henkelman, G.; Uberuaga, B. P.; Jónsson, H. *The Journal of Chemical Physics* **2000**, *113*, 9901–9904.

[100] A. Züttel and S. Rentsch and P. Fischer and P. Wenger and P. Sudan and Ph. Mauron and Ch. Emmenegger, *Journal of Alloys and Compounds* **2003**, *356–357*, 515–520, Proceedings of the Eighth International Symposium on Metal-Hydrogen Systems, Fundamentals and Applications (MH2002).

[101] Miwa, K.; Aoki, M.; Noritake, T.; Ohba, N.; Nakamori, Y.; Towata, S.-i.; Züttel, A.; Orimo, S.-i. *Phys. Rev. B* **2006**, *74*, 155122.

[102] Severa, Godwin and Rönnebro, Ewa and Jensen, Craig M., *Chem. Commun.* **2010**, *46*, –.

[103] Chong, M.; Karkamkar, A.; Autrey, T.; Orimo, S.-i.; Jalisatgi, S.; Jensen, C. M. *Chem. Commun.* **2011**, *47*, 1330–1332.

[104] Rönnebro, E.; Majzoub, E. H. *The Journal of Physical Chemistry B* **2007**, *111*, 12045–12047, PMID: 17914804.

[105] Kim, J.-H.; Shim, J.-H.; Cho, Y. W. *Journal of Power Sources* **2008**, *181*, 140–143, SPECIAL SECTION Selected papers from the 1st POLISH FORUM ON FUEL CELLS AND HYDROGEN.

[106] Barkhordarian, G.; Jensen, T. R.; Doppiu, S.; Bosenberg, U.; Borgschulte, A.; Gremaud, R.; Cerenius, Y.; Dornheim, M.; Klassen, T.; Bormann, R. *The Journal of Physical Chemistry C* **2008**, *112*, 2743–2749.

[107] Łodziana, Z.; Vegge, T. *Phys. Rev. Lett.* **2006**, *97*, 119602.

[108] Bée, M. *Quasielastic Neutron Scattering: Principles and Applications in Solid State Chemistry, Biology and Materials science*; Adam Hilger: Bristol, U.K., 1988; p 437.

[109] Buchter, F. et al. *The Journal of Physical Chemistry B* **2008**, *112*, 8042–8048, PMID: 18553898.

[110] Filinchuk, Y.; Rönnebro, E.; Chandra, D. *Acta Materialia* **2009**, *57*, 732 – 738.

[111] Her, J.-H.; Stephens, P. W.; Gao, Y.; Soloveichik, G. L.; Rijssenbeek, J.; Andrus, M.; Zhao, J.-C. *Acta Crystallographica Section B* **2007**, *63*, 561–568.

[112] Černý, R.; Filinchuk, Y.; Hagemann, H.; Yvon, K. *Angewandte Chemie International Edition* **2007**, *46*, 5765–5767.

[113] Dai, B.; Sholl, D. S.; Johnson, J. K. *The Journal of Physical Chemistry C* **2008**, *112*, 4391–4395.

[114] Voss, J.; Hummelshøj, J. S.; Łodziana, Z.; Vegge, T. *Journal of Physics: Condensed Matter* **2009**, *21*, 012203.

[115] Schönflies, A. *Mathematische Annalen* **1889**, *34*, 172–203.

[116] Bahn, S. R.; Jacobsen, K. W. *Comput. Sci. Eng.* **2002**, *4*, 56–66.

[117] Feibelman, P. J. *Phys. Rev. Lett.* **1990**, *65*, 729–732.

[118] Bork, N. DFT modelling of oxide materials for hydrogen permeable membranes. Ph.D. thesis, The Technical University of Denmark, 2010.

[119] Sundell, P. G.; Björketun, M. E.; Wahnström, G. *Phys. Rev. B* **2007**, *76*, 094301.

[120] Zhang, Q.; Wahnström, G.; Björketun, M. E.; Gao, S.; Wang, E. *Phys. Rev. Lett.* **2008**, *101*, 215902.

[121] Iwahara, H.; Esaka, T.; Uchida, H.; Maeda, N. *Solid State Ionics* **1981**, *3–4*, 359 – 363.

# Part IV

# Publications

# Hydrogen Rotational and Translational Diffusion in Calcium Borohydride from Quasielastic Neutron Scattering and DFT Calculations

**D. Blanchard,*,† M. D. Riktor,‡ J. B. Maronsson,†,§ H. S. Jacobsen,† J. Kehres,† D. Sveinbjörnsson,† E. Gil Bardají,|| A. Léon,|| F. Juranyi,⊥ J. Wuttke,# B. C. Hauback,‡ M. Fichtner,|| and T. Vegge†**

*Materials Research Division, Risø National Laboratory for Sustainable Energy, Technical University of Denmark, Building 228, P.O. Box 49, DK-4000 Roskilde, Denmark, Physics Department, Institute for Energy Technology, P.O. Box 40, NO-2027 Kjeller, Norway, Center for Atomic Scale Materials Design, Technical University of Denmark, DK-2800 Lyngby, Denmark, Institute of Nanotechnology, Karlsruhe Institute of Technology (KIT), P.O. Box 3640, D-76021 Karlsruhe, Germany, Laboratory for Neutron Scattering ETH Zurich and Paul Scherrer Institut, CH- 5232 Villigen PSI, Switzerland, Forschungszentrum Jülich, JCNS at FRM II, Lichtenbergstrasse 1, 85747 Garching, Germany*

*Received: July 9, 2010; Revised Manuscript Received: October 8, 2010*

Hydrogen dynamics in crystalline calcium borohydride can be initiated by long-range diffusion or localized motion such as rotations, librations, and vibrations. Herein, the rotational and translational diffusion were studied by quasielastic neutron scattering (QENS) by using two instruments with different time scales in combination with density functional theory (DFT) calculations. Two thermally activated reorientational motions were observed, around the 2-fold ($C_2$) and 3-fold ($C_3$) axes of the $BH_4^-$ units, at temperature from 95 to 280K. The experimental energy barriers ($Ea_{C2} = 0.14$ eV and $Ea_{C3} = 0.10$ eV) and mean residence times are comparable with those obtained from DFT calculations. Long-range diffusion events, with an energy barrier of $E_{aD} = 0.12$ eV and an effective jump length of ~2.5 Å were observed at 224 and 260 K. Three vacancy-mediated diffusion events, H jumps between two neighboring $BH_4^-$, and diffusion of $BH_4^-$ and $BH_3$ groups were calculated and finally discarded because of their very high formation energies and diffusion barriers. Three interstitial diffusion processes (H, $H_2$, and $H_2O$) were also calculated. The H interstitial was found to be highly unstable, whereas the $H_2$ interstitial has a low energy of formation (0.40 eV) and diffusion barrier (0.09 eV) with a jump length (2.1 Å) that corresponds well with the experimental values. $H_2O$ interstitial has an energy of formation of −0.05 eV, and two different diffusion pathways were found. The first gives a H jump distance of 2.45 Å with a diffusion barrier of 0.68 eV, the second one, more favorable, exhibits a H jump distance of 1.08 Å with a barrier of 0.40 eV. The correlation between the QENS and DFT calculations indicates that, most probably, it is the diffusion of interstitial $H_2$ that was observed. The origin of the interstitial $H_2$ might come from the synthesis of the compound or a side reaction with trapped synthesis residue leading to the partial oxidation of the compound and hydrogen release.

## Introduction

Metal borohydrides are of interest as hydrogen storage materials because of their high volumetric and gravimetric capacity. However, like many of the complex hydrides, they are generally thermodynamically too stable and have slow absorption and desorption kinetics and poor reversibility.[1,2]

Among the borohydrides, $Mg(BH_4)_2$ and $Ca(BH_4)_2$ have more favorable thermodynamics than for example $LiBH_4$ while maintaining attractive hydrogen capacities (14.9 and 11.5 mass%, respectively).[2,3] Furthermore, they have both been shown to be partially reversible by utilizing high pressure,[4,5] and $Ca(BH_4)_2$ by utilizing additives[6] or destabilized routes.[7]

Noting the lack of knowledge about their structural transition and decomposition mechanisms, we have investigated the hydrogen dynamics in calcium borohydride by using quasielastic neutron scattering (QENS). This method is optimal to study hydrogen dynamics because of the large incoherent scattering cross section of hydrogen compared to all other scattering signals.[8] Although the dynamics in interstitial metal hydrides have been widely studied with neutron scattering,[9−12] only few published results on complex hydrides exist. As examples, the hydrogen dynamics in $NaAlH_4$ and $Na_3AlH_6$ were studied. It showed only limited hydrogen vacancy diffusion, not changed by the use of Ti additive.[13] In other work,[14,15] hydrogen rotational diffusion in $NaBH_4$ was observed, but no long-range diffusion was observed.

In $Ca(BH_4)_2$, hydrogen is covalently bound to boron, forming tetrahedral $BH_4^-$ complexes. The possible hydrogen dynamics are long-range translational diffusion and localized motions such as rotations of the $BH_4^-$ complexes along specific axes, librations of the complexes, and vibrations within the complexes. Rotational dynamics are often coupled to order−disorder phase

* Corresponding author. E-mail: dibl@risoe.dtu.dk.
† Risø National Laboratory for Sustainable Energy, Technical University of Denmark.
‡ Institute for Energy Technology.
§ Center for Atomic Scale Materials Design, Technical University of Denmark.
|| Karlsruhe Institute of Technology.
⊥ Laboratory for Neutron Scattering ETH Zurich and Paul Scherrer Institut.
# Forschungszentrum Jülich.

10.1021/jp107281v 
Published on Web 11/09/2010

**TABLE 1: $\beta$-Ca(BH$_4$)$_2$ Structural Parameters Obtained from Rietveld Refinement of PXD Pattern and DFT Calculations[a]**

| space group $P4_2/m$ (no. 84); $Z = 2$ | | | |
|---|---|---|---|
| DFT | $a = 6.849$ Å | $c = 4.367$ Å | |
| PXD | 7.021(6) | 4.417(6) | |
| ref 16 | (6.946(8))[b] | (4.366(1)) | |
| site | *x/a* | *y/b* | *z/c* |
| Ca/2c | 0.5 (0.5) | 0 (0) | 0.5 (0.5) |
| B/4j | 0.316 (0.302) | 0.209 (0.200) | 0 (0) |
| H1/4j | 0.313 (0.295) | 0.387 (0.347) | 0 (0) |
| H2/4j | 0.490 (0.468) | 0.170 (0.185) | 0 (0) |
| H3/8k | 0.234 (0.226) | 0.142 (0.161) | 0.772 (0.800) |

[a] In both cases, the starting values were taken from ref 16. During Rietveld refinements, the atomic positions were not refined. [b] Numbers in brackets: parameters from ref 16.

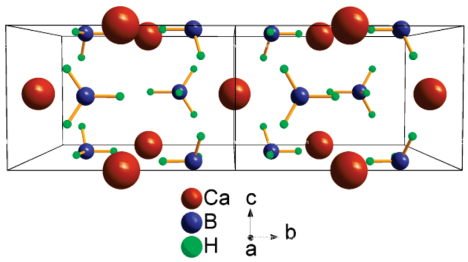


**Figure 1.** Structure of $\beta$-Ca(BH$_4$)$_2$. Space group $P4_2/m$. Large, medium, and small spheres: Ca, B, and H atoms, respectively.

transition in coordination compounds, and the borohydrides decomposition could possibly involve long-range diffusion of H and/or of the whole $BH_4^-$ complexes.

At least, two different tetragonal space groups have been proposed to describe the $\beta$-Ca(BH$_4$)$_2$: Butcher et al.[16] chose the $P4_2/m$ space group, whereas Filinchuk et al.[17] proposed $P$-4. The differences in the proposed structures reflect the degree of order of the $BH_4^-$ units. The possibility to refine the $\beta$-structure in different tetragonal space groups with different $BH_4^-$ orientations suggests that the polymorph is stabilized by static or dynamic disorder of the borohydride units like for the high-temperature polymorphic transformation of LiBH$_4$.[18−20] For the Rietveld refinement as well as for the DFT calculations, the $P4_2/m$ space group and the crystallographic data from ref 16 were used (Table 1). Ca(BH$_4$)$_2$ forms ionic crystals consisting of $Ca^{2+}$ and $BH_4^-$ ions. The $Ca^{2+}$ ions are coordinated by six $BH_4^-$ tetrahedra in a bidendate configuration. The B−H interatomic distances are in the range of 1.1 Å, and the Ca−Ca distances are about 4.35 Å (Figure 1). There are two formula units per unit cell. The Ca atoms occupy the (2c) Wyckoff positions, the B atoms occupy the (4j) positions, and the H atoms are distributed over the (4j) and (8k) sites. The $BH_4^-$ tetrahedra possess three 2-fold rotational symmetries ($C_2$) and four 3-fold rotational symmetries ($C_3$) leading to three 180° and four 120° rotations (Figure 2).

Herein, the aim was to investigate the rotational and long-range translational diffusion of H-rich species in $\beta$-Ca(BH$_4$)$_2$. Therefore, QENS combined with density functional theory (DFT) calculations have been applied.

## Material and Experimental Methods

Natural B contains 20% of $^{10}$B which has a high absorption cross section of 3837 barns. Therefore, to reduce neutron absorption, Ca(BH$_4$)$_2$ was synthesized via the metathesis reaction of eq 1 by using a $^{11}$B-enriched precursor ($5.5 \times 10^{-3}$ barns).

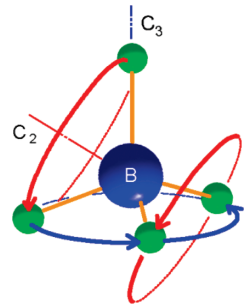


**Figure 2.** 2-fold $C_2$-axis and 3-fold $C_3$-axis of the $BH_4^-$ units. Large and small spheres: B and H atoms, respectively.

$$2Na^{11}BH_4 + CaCl_2 \rightarrow Ca(^{11}BH_4)_2 + 2NaCl \qquad (1)$$

A total of 2.40 g (0.063 mol) of $Na^{11}BH_4$ (purchased from Katchem Ltd., purity 99.8%) was first ball-milled for 4 h in a Fritsch P6 planetary mill at 600 rpm, with a ball-to-powder ratio of 25:1, and then added to 3.52 g (0.032 mol) of $CaCl_2$ (purchased from Alfa Aesar, purity 96%) in 100 mL of THF. The mixture was heated under reflux at 80 °C for 24 h. After cooling to room temperature, the suspension was filtered off, and the filtrate was evaporated under vacuum to remove the solvent. The resulting $Ca(^{11}BH_4)_2 \cdot n$ THF adduct was then dried at elevated temperature under vacuum (at 80 °C for 2 h, at 100 °C for 2 h, at 130 °C for 1 h, at 160 °C for 1 h, and at 200 °C for 16 h). The isolated yield (with respect to $CaCl_2$) was 2.0 g (90%).

Calcium borohydride crystallizes in different structure modifications depending on the synthesis conditions, and a mixture of the three structures, α-Ca(BH$_4$)$_2$, $\beta$-Ca(BH$_4$)$_2$,[16,21] and $\gamma$-Ca(BH$_4$)$_2$ may be formed. The drying procedure used during the synthesis aimed to obtain $\beta$-Ca(BH$_4$)$_2$ as a single phase.

A powder X-ray diffraction (PXD) was recorded with a BRUKER D8 diffractometer (40 kV, 40 mA, Cu radiation $K_\alpha$ =1.542 Å, Figure 3). Quantitative phase analysis based on Rietveld refinements performed by using Rietica software[22] gave a molar composition of 85% $\beta$-Ca(BH$_4$)$_2$, 6% α-Ca(BH$_4$)$_2$, 4% $CaH_2$, and 5% NaCl, and thus, ∼93% of the hydrogen in the sample belongs to $\beta$-Ca(BH$_4$)$_2$. Only the cell parameters were refined. For $CaBH_4$ (see Table 1), they are slightly larger than those in ref 16, probably because of the quality of the diffraction pattern; but they are still in reasonable agreement.

Mass spectrometry measurements (MS), obtained by using an OmniStar (GSD 320) mass spectrometer, were performed on the gas released by the sample when heated under dynamical vacuum from room temperature up to 723 K (heating ramp of 1K min$^{-1}$, Figure 4). The analysis of the measurement shows that $H_2$ accounts for ∼98.7% of the released gas, and THF accounts for ∼1.2%; the amount of $H_2O$, $B_2H_6$, and other gases such as $O_2$ are negligible (≪1%). Thus, the amount of THF left in the sample after its synthesis is very low, and the sample appears to be water free.

QENS experiments were performed with two complementary instruments, SPHERES and MARS, in order to cover a wide energy range with two different energy resolutions. SPHERES[23] is a high-resolution neutron backscattering spectrometer located

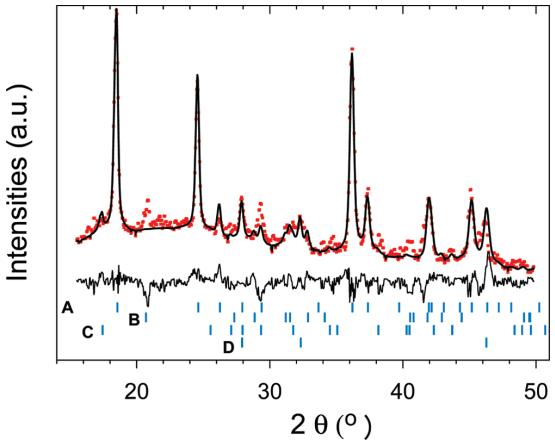


**Figure 3.** PXD pattern of the as-prepared $\beta$-$Ca(BH_4)_2$. The dots are the experimental points, the line is the refined pattern based on the Rietveld method, and the bottom line is the difference between the experimental and the refined pattern. The ticks are the position of the Bragg peaks for A: $\beta$-$Ca(BH_4)_2$, B: $CaH_2$, C: $\alpha$-$Ca(BH_4)_2$, and D: NaCl.

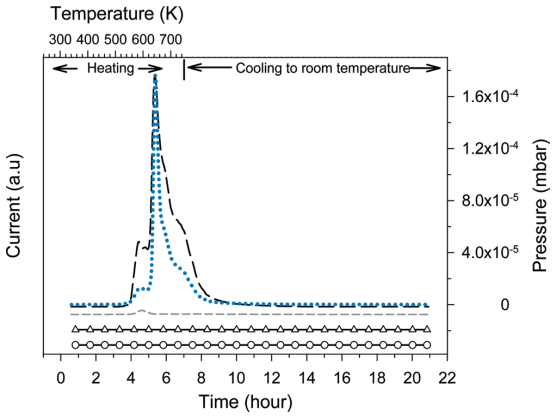


**Figure 4.** Mass spectrometry measurements. The sample was heated under dynamical vacuum from room temperature up to 723 K at a heating ramp of 1K.min$^{-1}$. Dotted line, pressure evolution; long dashed line, $H_2$ signal; short dashed line, THF signal; circles, $B_2H_6$ signal; triangles, $H_2O$ signal.

at FRM II (Forschungs-Neutronenquelle Heinz Maier-Leibnitz), Garching, Germany. MARS[24] is an inverted geometry time-of-flight spectrometer located at the Swiss Spallation Neutron Source (SINQ), Paul Scherrer Institute, Villigen, Switzerland.

The experiments at SPHERES were performed with ~0.1 g of $Ca(BH_4)_2$, which was loaded in an Al wire sealed flat 30 × 40 × 0.5 mm$^3$ Al container oriented at 135° with respect to the direct beam. Si(111) monochromator and analyzer crystals were used in a backscattering geometry, giving a final neutron wavelength of 6.271 Å and an energy resolution of 0.65 $\mu$eV with an energy-transfer range selected within ±15.8 $\mu$eV. The spectra were recorded by nine detectors corresponding to a scattering vector ranging from 0.59 to 1.66 Å$^{-1}$. The data reduction was carried out with SLAW, a neutron histogram to scattering law converter.[25]

The experiments at MARS were performed with ~0.4 g of $Ca(BH_4)_2$, from the same batch, which was loaded in a double-wall Al container with a height of 60 mm and diameters of 9 mm and 10 mm. The spectra were recorded by five detectors on both side of the instrument corresponding to a scattering vector ranging from 0.49 to 1.86 Å$^{-1}$. Mica(006) analyzers were used in a near-backscattering geometry, giving a final neutron wavelength of 6.65 Å and an energy resolution of 13 $\mu$eV. The energy-transfer window was chosen differently depending on the width of the quasielastic signal, the largest being from −0.04 to 0.43 meV. The data reduction was carried out with the data analysis and visualization environment DAVE.[25]

## DFT Calculations

Theoretical calculations were used to identify the possible dynamic events by calculating their energy barriers and prefactors. The calculations were performed by using the atomic simulation environment (ASE) package,[27] and the DACAPO plane-wave basis-set implementation[28] was used to solve the electronic structure problem within the DFT formalism.[29] The ion cores were described by ultrasoft pseudopotentials,[30] and the exchange and correlation effects were described by the PW91 functional.[31] The Kohn−Sham wave functions were expanded in a plane-wave basis set with a cutoff energy of 350 and 600 eV for the density grid cutoff. The wave functions were sampled on a (2 × 2 × 2) k-point mesh. The unit cell containing 2 $Ca(BH_4)_2$ units was the $\beta$-phase structure.[16] To eliminate any spurious periodic interactions, the calculations were carried out on a 176 atoms supercell, which consisted of the unit cell repeated once in each spatial direction. Iterative relaxation using the limited memory Broyden−Fletcher−Goldfarb−Shanno algorithm[32] was employed to obtain the zero-temperature structure and unit-cell parameters. A force convergence criterion of 0.001 eV/Å was used for the structure minimization.

The nudged elastic band (NEB) method,[33] along with the FIRE minimization algorithm,[34] was used to locate first-order saddle-point configurations, connecting two local minima, that could be used within harmonic transition state theory (hTST)[35] to determine the thermally activated reaction rates ($r(T)$) by using the barrier height ($Ea$) and the vibrational frequencies at the initial state ($\nu^{IS}$) and saddle point ($\nu^{TS}$).

$$r(T) = \frac{\prod_{i=1}^{3N} \nu_i^{IS}}{\prod_{i=1}^{3N-1} \nu_i^{TS}} e^{-\frac{Ea}{k_B T}} \qquad (2)$$

The vibrational frequencies were acquired by using a finite difference approximation of the Hessian matrix (back and forward displacements of 0.01 Å). The term outside the exponential in eq 2, often referred to as the prefactor, compares the vibrational frequencies at the initial state and saddle point. The characteristic times are the reciprocal values of these prefactors.

A force convergence criterion of 0.01 eV/Å was used for the NEB calculations that lead to vibrational frequencies calculations and 0.05 eV/Å for the NEB calculations that only considered the barriers.

The initial paths used when locating the rotational pathways were simple rigid rotations of all the hydrogen atoms in a single $BH_4^-$ unit.

To calculate diffusion, vacancies were created by removing the atom(s) in question and rerelaxing the atomic coordinates. Similarly, interstitials were created by inserting the atom(s) in question and rerelaxing the atomic coordinates. Neighboring, relaxed, defect structures were then used as end points in linearly interpolated NEB calculations.

**TABLE 2: Summary of the Experimental (QENS, Rotational and Translational Diffusion) and Computational (DFT, Rotational Diffusion) Results for $\beta$-$Ca(BH_4)_2$**

| $\tau_0{}^a$ (ps) | | $E_a{}^a$ (eV) | |
|---|---|---|---|
| MARS and SPHERES | | | |
| $C_3$ | $C_2$ | $C_3$ | $C_2$ |
| $5.0 \times 10^{-2}$ | $5.6 \times 10^{-2}$ | 0.10 | 0.14 |
| long-range diffusion | | | |
| 4 | | 0.12 | |
| DFT | | | |
| $C_3$ | $C_2$ | $C_3$ | $C_2$ |
| $1.87 \times 10^{-2}$ | $3.97 \times 10^{-2}$ | 0.11 | 0.15 |

[a] $\tau_0$ and $E_a$ experimental values obtained from the Arrhenius fits ($\tau = \tau_0 \exp(E_a/(k_bT))$) of the experimental mean resident times.

**TABLE 3: Summary of the Computational (DFT, Translational Diffusion) Results for $\beta$-$Ca(BH_4)_2$**

| defect type | formation energy (eV)[a] | $\tau_0$ (ps) | $E_{aD}$ (eV) | diffusion length (Å) |
|---|---|---|---|---|
| H vacancy | 2.09 | $8.0 \times 10^{-1}$ | 0.46 | 2.1 |
| $BH_3$ vacancy | 1.56 | $6.1 \times 10^{-2}$ | 1.92 | 3.3 |
| $BH_4$ vacancy | 2.83 | N/A[b] | 0.63 | 3.8 |
| H interstitial | 2.34[c] | N/A | N/A | N/A |
| $H_2$ interstitial | 0.40 | $5.68 \times 10^{-2}$ | 0.09 | 2.1 |
| $H_2O$ inter. flip | −0.05 | N/A | 0.40 | 1.08 |
| $H_2O$ interstitial | −0.05 | N/A | 0.68 | 2.45 |

[a] The formation energies were calculated for neutral species. [b] N/A: not calculated. [c] The H interstitial is not stable and relaxes to a $H_2$ interstitial coupled to a H vacancy.

## Results

**QENS Spectra.** Inelastic temperature scans were performed on both instruments. For each temperature, the spectra collected on each detector were summed to get one spectra. The elastic intensities were obtained by adding up the counts with an energy transfer of $|\delta E| \leq 8$ $\mu$eV and $|\delta E| \leq 0.32$ $\mu$eV for MARS and SPHERES, respectively. The inelastic intensities were deduced by summing up the counts out of the elastic regions. Figure 5 displays the evolution with temperature of the normalized elastic ($I_{N\text{-el}}$) and inelastic ($I_{N\text{-inel}}$) scattering measured at MARS and SPHERES. The sample was heated from 70 to 565 K at MARS. At 70 K, no inelastic broadening was detected because the hydrogen is frozen-in on the time scale accessible with the instrument. On heating between 70 and 120 K, $I_{N\text{-el}}$ ($|\delta E| \leq 8$ $\mu$eV) slowly decreased, whereas $I_{N\text{-inel}}$ ($|\delta E| > 8$ $\mu$eV) slowly increased; then, the same evolution is continued only faster. The maximum $I_{N\text{-inel}}$ is at 200 K followed by a decrease and then no more changes. At this temperature and above, the hydrogen motion is too fast, and the large inelastic broadening gives a flat background. When cooling from 565 to 200 K, $I_{N\text{-el}}$ is identical to that observed during heating, whereas $I_{N\text{-inel}}$ is found to be lower. At $T < 200$ K, $I_{N\text{-el}}$ is also found to be lower than on heating, indicating a loss of ~18% (weakly) bound hydrogen, that has been desorbed during heating. The MS measurement revealed a slight release of hydrogen between 520 and 565 K, corresponding to ~4% of the total hydrogen released during the measurement up to 723 K (see Figure 4). Similar observations have been made in several other published studies.[36−38] In ref 38, the sample, heated up to 603 K, was quenched and examined with high-resolution synchrotron radiation powder diffraction. Along with $\beta$-$Ca(BH_4)_2$, Bragg peaks from an unknown phase were observed, which have recently been identified and structurally resolved as an oxide of the borohydride.[39] PXD measurements made on the sample used for the temperature scans with MARS (not shown herein) also revealed the presence of this oxide phase. Thus, the hydrogen release observed during the MS measurement and temperature scan might come from a reaction of the hydride with oxygen or water. The oxygen level remains in the background level during the MS; therefore, one can exclude the existence of a leak in the experimental setup, and the only source of oxygen or water comes from the sample itself, without excluding a possible reaction with residual THF.

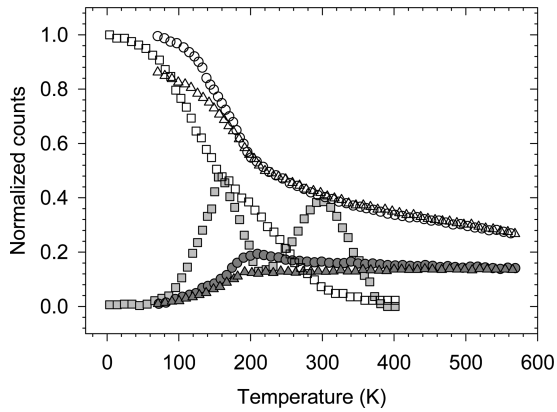


**Figure 5.** Normalized elastic and inelastic intensities ($I_{N\text{-el}}$ and $I_{N\text{-inel}}$) during temperature scans. Open and filled ○: $I_{N\text{-el}}$ and $I_{N\text{-inel}}$, respectively, with MARS on heating from 70 to 570 K. Open and filled △: $I_{N\text{-el}}$ and $I_{N\text{-inel}}$, respectively, with MARS on cooling from 570 to 70 K. Open and filled □: $I_{N\text{-el}}$ and $I_{N\text{-inel}}$, respectively, with SPHERES on heating from 3 to 400 K.

At SPHERES, the temperature scan (Figure 5) was performed only during heating. It showed almost the same features as those for the MARS measurements, but changes occurred at lower temperatures. The inelastic intensity ($|\delta E| \leq 0.32$ $\mu$eV) starts to increase at around 80 K, with the maximum at 160 K, and decreases significantly afterward. However, at 220 K, $I_{N\text{-inel}}$ ($|\delta E| > 0.32$ $\mu$eV) increases again with a maximum at 320 K followed by a decrease and then flatten out at 390 K. At this temperature, the hydrogen motion gives rise to a broadening too large for the instrument energy window. The two bumps in the inelastic signal were attributed to two different types of hydrogen dynamics, as it will be discussed below.

The temperatures to perform the measurements were selected from these scans (see Table 4). The QENS spectra were analyzed by using the curve fitting utility (PAN) included in the DAVE package. They consist of one elastic and some inelastic components. The elastic component comes from the scattering process with no change in the neutron energy, whereas the inelastic component reflects the energy transfer, gain, and loss, due to the hydrogen motions. The measured total incoherent scattering function, $S_{inc}^{tot}(Q\omega)$, is given by (see ref 8 for more details):

$$S_{inc}^{tot}(Q\omega) = R(Q\omega) \otimes (A_0(Q)\delta(\omega) + \sum_i A_i(Q)L(\Gamma_i, \omega)) + B(Q) \quad (3)$$

where $R(Q,\omega)$ is the instrumental resolution, $\delta(\omega)$ is the Dirac delta function describing the elastic scattering. $L(\Gamma_i,\omega)$ are Lorentzian functions which model the inelastic signal with $\Gamma_i$ = half width at half maximum (HWHM). The $B$ term represents

**TABLE 4: Summary of the Experimental (QENS) Results for $\beta$-$Ca(BH_4)_2$**

| | $\tau$ (ps) | |
|---|---|---|
| temp. (K) | $C_3$ | $C_2$ |
| | MARS | |
| 100 | 204 | - |
| 130 | 145 | - |
| 160 | 40 | - |
| 190 | 17 | 245 |
| 220 | 8 | 82 |
| 280 | 3 | 32 |
| | SPHERES | |
| 95 | 6582 | - |
| 116 | 429 | - |
| 143 | 141 | 7520 |
| 163 | 58 | 1755 |
| 204 | - | 131 |
| | long-range diffusion | |
| 224 | 2302 | |
| 260 | 977 | |

the inelastic background in the quasielastic region. It can originate from processes that are much faster than those observable within the time scale of the instruments used. The term $A_0(Q)$ is the elastic incoherent structure factor (EISF).[8] Its dependence on $Q$, the wave vector transfer, is important. It basically determines the static properties of the number of sites accessible to the hydrogen atoms, the locations of these sites, and the normalized probability to be at a given sites. It is a measurable quantity, evaluated from the ratio:

$$A_0(Q) = \frac{I_{el}(Q)}{I_{el}(Q) + I_{inel}(Q)} \quad (4)$$

where $I_{el}(Q)$ and $I_{inel}(Q)$ are the integrated intensities of the elastic and inelastic signal, respectively.

Herein and following eq 3, the QENS spectra were analyzed with the resolution-limited elastic peak, the delta function folded with the instrumental resolutions, and one or two Lorentzian, depending on the temperature. The instrumental resolutions were obtained from measurements at 3 K (SPHERES) and 70 K (MARS). At these temperatures, no dynamical motions were observed on the time scale of the two instruments. The centers of the delta function and of the Lorentzian were constrained to be the same. For the measurements performed at MARS, because the energy window of the resolution function was smaller than those used for the measurements at higher temperatures, a flat fixed background was used. For the measurements performed at SPHERES, a flat background was used to model the too broad Lorentzian at high temperatures. Figures 6 and 7 present typical examples of the spectra together with their fits with one or two Lorentzian. For the whole temperature range measured at MARS, and at least up to 220 K at SPHERES, the widths of the Lorentzian functions were found to be $Q$-independent over the measured $Q$ range. This indicates that the observed inelastic broadenings originate from localized hydrogen motion.[8] Figure 8 displays the values of the average HWHMs, over all the detectors, versus temperature. At SPHERES, for two temperatures above 220 K (224 and 260 K), the HWHMs were found to be $Q$-dependent (Figure 11), a signature for nonlocalized motion and possibly long-range diffusion. Unfortunately, at higher temperature, the fits of the QENS spectra are no longer reliable because of the low signal intensity combined with the too broad inelastic component at high Q values.

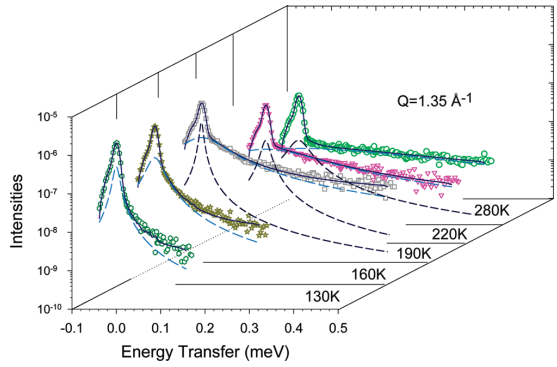


**Figure 6.** QENS of $\beta$-$Ca(BH_4)_2$ measured with MARS at different temperatures for $Q = 1.35$ Å$^{-1}$. The dots are the experimental data. The solid lines display the fits of the data, each consisting of a resolution-broadened delta function, a flat background, and one or two Lorentzian (dashed line).

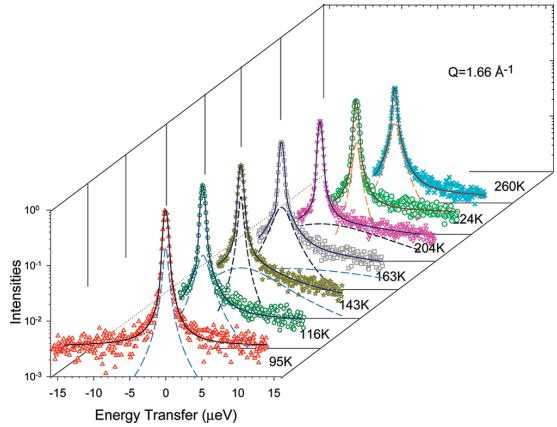


**Figure 7.** QENS of $\beta$-$Ca(BH_4)_2$ measured with SPHERES at different temperatures for $Q = 1.66$ Å$^{-1}$. The dots are the experimental data. The solid lines display the fits of the data, each consisting of a resolution-broadened delta function, one or two Lorentzian (dashed line), and a flat background for the three last temperatures (not shown on the plots).

The first obvious localized motions are the rotations around the 2-fold and 3-fold axis (Figure 2). For $BH_4^-$ rotations around the $C_2$-axis, the tetrahedral ions have two equal equilibrium orientations, and the EISF is:[8]

$$A_0(Q) = \frac{1}{2}\left(1 + j_0\left(2\frac{\sqrt{2}}{\sqrt{3}}Qd\right)\right) \quad (5)$$

where $j_0(x) = \sin(x)/x$ is the zeroth order Bessel function and $d$ is the bond length between B and H. This rotation gives rise to one Lorentzian with a $Q$-independent HWHM of

$$\Gamma_{C2} = 2\hbar\tau_2^{-1} \quad (6)$$

$\tau_2$ represents the average time that a hydrogen atom stays at a site before jumping to a new site because of reorientation around the 2-fold axis.

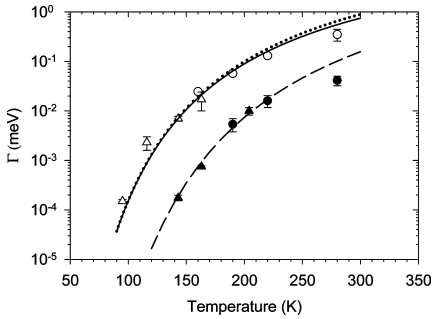


**Figure 8.** Experimental and theoretical HWHMs. The dots are the averaged, over all the detectors, experimental values. Triangles, SPHERES data; circles, MARS data. The theoretical values are calculated from eqs 9−11, with values of the characteristic times, energy barriers, and prefactors obtained from DFT. Dotted line, HWHMs calculated from eq 9; solid line, HWHMs calculated from eq 10; dashed line, HWHMs calculated from eq 11.

For $BH_4^-$ rotations around the $C_3$-axis, the tetrahedral ions have three equal equilibrium orientations, and one hydrogen atom remains immobile. The expression for the EISF is identical to the rotation around the $C_2$-axis (eq 5).[8] It gives rise to one Lorentzian with a $Q$-independent HWHM of

$$\Gamma_{C3} = \frac{3}{2}\hbar\tau_3^{-1} \tag{7}$$

$\tau_3$ represents the average time that a hydrogen atom stays at a site before jumping to a new site because of reorientation around the 3-fold axis.

In the case of combination of rotations around several $C_2$ and $C_3$-axis, with two different jump rates, the EISF is given by:[15]

$$A_0(Q) = \frac{1}{4}\left(1 + j_0\left(Q\frac{2\sqrt{2}}{\sqrt{3}}d\right)\right)\left(1 + j_0\left(Q\frac{2\sqrt{2}}{\sqrt{3}}d\right)\right) \tag{8}$$

The combination of these two rotations gives rise to three Lorentzian with the following $Q$-independent HWHMs:

$$\Gamma_1 = \hbar(2\tau_2^{-1} + \frac{3}{2}\tau_3^{-1}) \tag{9}$$

$$\Gamma_2 = \frac{3}{2}\hbar\tau_3^{-1} \tag{10}$$

$$\Gamma_3 = 2\hbar\tau_2^{-1} \tag{11}$$

with $\tau_2$ and $\tau_3$ defined above.

The experimental EISFs, extracted from the fitted QENS spectra (eq 4), and those calculated with the models described above (eqs 5 and 8) provide strong evidence about the nature of the localized motions. Figure 9 displays the EISFs. The model for one rotation (eq 5) follows the experimental data when one inelastic component was detected in the QENS spectra (95 and 204 K with SPHERES, 130 and 160 K with MARS). The model combining the two rotations ($C_2$−$C_3$, eq 8) reproduces the experimental EISFs when two Lorentzian were needed to fit the QENS spectra (116−163 K with SPHERES, 190 K and above with MARS). For both equations, the best fit was obtained for $d$ = 1.11 Å, a value in agreement with the B−H distance obtained from neutron-diffraction data.[15] The characteristic times of the localized hydrogen motion, now attributed to reorientational rotations, were calculated from the average HWHMs at a given temperature. Equations 9−11 were used. In the case of the low-temperature spectra, fitted with one Lorentzian, $\tau_2$ was considered as infinite. The results are presented in Table 4. The observed inelastic broadening follows an Arrhenius behavior, and the corresponding characteristic times can be expressed as

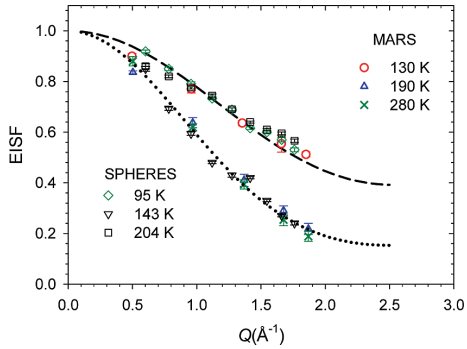


**Figure 9.** Measured and modeled EISFs. Dashed line, $C_3$ rotational diffusion model according to eq 5; dotted line, combination of $C_2$−$C_3$ rotational diffusion model according to eq 8. Not all the temperatures have been plotted in order to keep the figure clear.

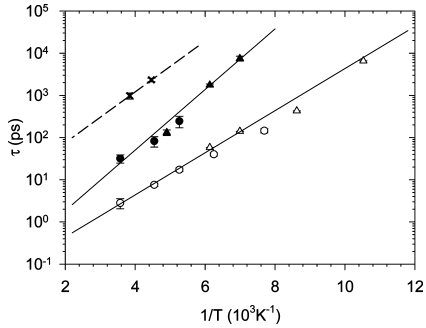


**Figure 10.** Thermally activated Arrhenius behavior of the rotational and translational diffusion of H in $\beta$-$Ca(BH_4)_2$. The triangles are the SPHERES experimental mean residence time ($\tau$) and the circles the MARS experimental values. Filled symbols: rotation around the $C_2$ axis, open symbols rotation around the $C_3$ axis. The cross symbols are the mean resident time between two diffusional jumps (data from SPHERES). $\tau$, inversely proportional to the inelastic broadening, is fitted as $\tau_0 \exp((E_a)/(k_BT))$ with $\tau_{0C2} = 5.6 \times 10^{-2}$ ps, $E_{aC2} = 0.14$ eV and $\tau_{0C3} = 5.0 \times 10^{-2}$ ps, $E_{aC3} = 0.10$ eV. The broken line is the fit for the diffusional jumps ($E_{aD} = 0.12$ eV, prefactor $\tau_{0D} = 4.7$ ps).

$$\tau = \tau_0 \exp\left(\frac{E_a}{k_BT}\right) \tag{12}$$

where the prefactor $\tau_0$ is a constant, $E_a$ is the energy barrier for the motion, $k_B$ is the Boltzmann constant, and $T$ is the temperature. Figure 10 displays the experimental characteristic times of the two thermally activated rotations together with the Arrhenius fits. The following values are obtained for the energy barriers: 0.14 and 0.10 eV for the $C_2$ and the $C_3$ rotations, respectively (see Table 4).

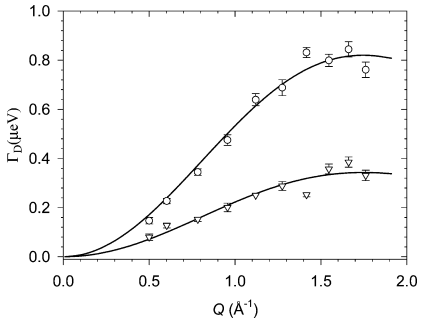


**Figure 11.** HWHM of the Lorentzian QENS component for $\beta$-$Ca(BH_4)_2$, as a function of $Q$ measured with SPHERES, at 224 K ($\nabla$) and 260 K (o). The full curves show the fits of the Chudley−Elliot model (eq 13) to the data.

For a nonlocalized motion, for example, long-range translational diffusion, the inelastic line broadening is $Q$-dependent.[8] Because hydrogen diffusion in complex hydrides can be vacancy-mediated, it must be taken into account that only the motion of the vacancy can be considered as random walk, whereas the involved atomic motions are correlated. Thus, the so-called encounter model should be used to describe the correlated jumps.[40] Nevertheless, in a zero-order approximation, that is, one atomic jump per stochastic vacancy diffusion step, the Chudley−Elliott model[41] can be used. The only effect is a rescaling of $\tau_D$, the mean time between two jumps.[40,42,43] In the Chudley−Elliot model, the $Q$-dependence of the HWHM ($\Gamma_D$) is given by[8]

$$\Gamma_D(Q) = \frac{\hbar}{\tau_D}\left(1 - \frac{\sin(QL)}{QL}\right) \qquad (13)$$

where $L$ is the effective jump length. $\tau_D$ and $L$ were extracted from the fits of the Chudley−Elliott model to the data obtained with SPHERES at 224 and 260 K (see Figure 11 and Table 4). The effective jump length was found to be about 2.5 Å (it corresponds to the shortest H−H distance between two neighboring $BH_4^-$ groups). An Arrhenius fit to the QENS data for the two available temperatures yields an energy barrier of $E_{aD} = 0.12$ eV and a prefactor of $\tau_{0D} = 4.7$ ps (see Figure 10 and Table 2).

**DFT Calculations.** The calculated structural parameters for the relaxed $\beta$-$Ca(BH_4)_2$ are displayed in Table 1. The Wyckoff positions and cell parameters are in good agreement with those from ref 16.

The results from the QENS experiments indicated localized dynamic events such as rotations of borohydride units as well as possible high-temperature diffusion. When using the Schönflies notation,[44] there are four different types of permutations possible for a single tetrahedral borohydride group. S4 axes and mirror planes can be quickly discarded because they are not rotations but rearrangements of hydrogen atoms which are much higher in energy because of the required formation of a planar $BH_4$ configuration during the rearrangement. Then, only various $C_2$ and $C_3$ axes remain. Figure 12 presents a 2D rigid rotation potential energy surface (PES) calculated by using a $C_2$-axis and a $C_3$-axis of a single $BH_4^-$ as the degrees of freedom. The starting point for the calculation is the relaxed structure, and thus, the origin of the axis represents an energy minimum. As expected from their symmetry, energy minima for the rotations around the C2-axis occur at $\pi$ and around the $C_3$-axis at $(2\pi)/3$ and $(4\pi)/3$. It shows that a slightly distorted $C_3$ rotation yields the lowest barrier and that a wobbly $C_2$-like rotation has a somewhat higher barrier (a difference of approximately 80%). The barrier heights calculated from the rigid rotation being higher than the barriers suggested by the experiments, NEB calculations were carried out with all the atoms in the supercell free to move. These calculations yielded barriers and characteristic times in good quantitative agreement with those of the experiments (see Table 2 and Figure 13). The calculated characteristic time for $C_2$ is about twice that of $C_3$. Looking at Figure 12, it can be seen that the environment of the saddle points for each rotation are quite different, and the vibrational calculations also revealed modes that involve motion of the cations, different by roughly a factor of 2. These finding are in reasonable agreement with experiments, where the prefactor for $C_2$ is found to be 10% larger than the one for $C_3$.

The theoretically expected temperature dependences of the HWHMs of the QENS spectra are plotted in Figure 8 together with the experimental values. The calculated lines were obtained

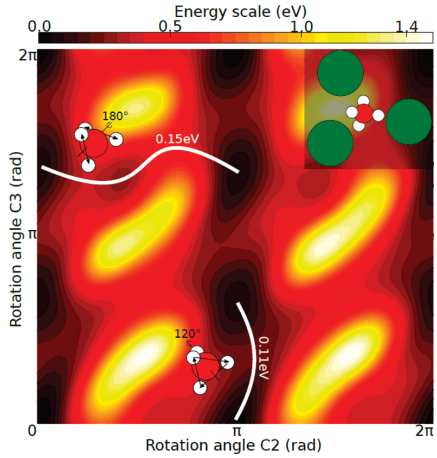


**Figure 12.** PES for $BH_4^-$ rigid rotations along the $C_2$-axis and $C_3$-axis. The marked paths represent those chosen to do the NEB calculations. Their respective NEB barrier heights are written next to each one. The inset shows the immediate environment of a $BH_4^-$ unit. Large, medium, and small spheres: Ca, B, and H atoms, respectively.

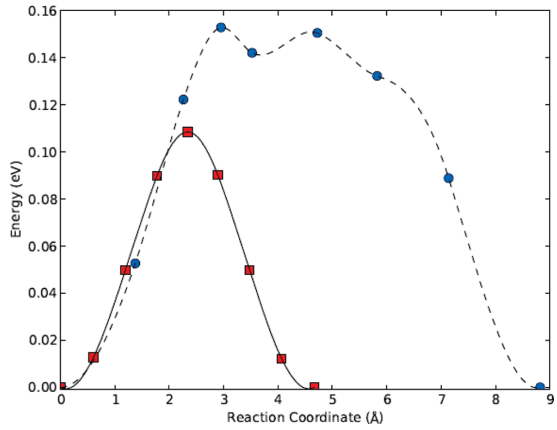


**Figure 13.** Calculated minimum energy path for the $C_2$ (blue circles) and $C_3$ (red squares) rotations. Each point is an NEB image; the lines are interpolations between them obtained by using also the forces. The reaction coordinate is the additive motion of atoms in the supercell.

by using eqs 9−11, with the characteristic times obtained by using the Arrhenius law (eq 12) and the energy barriers and prefactors from the DFT calculations. According to the experimental results, it should be noted that, although the combination of the two rotations ($C_2-C_3$) should give three Lorentzian, two have comparable HWHMs ($\Gamma_1 \approx \Gamma_2$) and can hardly be separated experimentally.

With two rotations unambiguously identified, only one dynamic event involving nonlocalized motion remained unexplained. Because further rotation could be ruled out, the diffusion process should be analyzed. Three vacancy-mediated diffusion events, H jumps between two neighboring $BH_4^-$, and diffusion of $BH_4^-$ and $BH_3$ groups, were calculated. All were found to have high formation energies of the corresponding neutral vacancies and high diffusion energy barriers (see Table 3). Subsequently, interstitial-mediated diffusion of H, $H_2$, and $H_2O$ were considered. The H interstitial is found to be unstable and formed a $H_2$ interstitial coupled to a H vacancy on a $BH_4^-$, with a very high formation energy (see Table 3). $H_2O$ and $H_2$ interstitials were found to have low formation energies, that is, −0.05 and 0.4 eV, respectively. Two pathways were identified for $H_2O$ diffusion, one involving a flip of the molecule and one giving a longer jump distance with a higher energy barrier; nevertheless, both pathways exhibit values slightly different from the experimental ones. Only interstitial $H_2$ diffusion gave a barrier and jump length which corresponds well to the experimentally observed value (Tables 2 and 3). The agreement between the calculated characteristic time for $H_2$ diffusion and the one obtained experimentally is not absolute; however it should be noted that the later was extracted from an Arrhenius fit with only two points. It is subject to caution and yields an uncharacteristically high prefactor.

All the information about the initial and final coordinates of the species to diffuse (interstitial $H_2$ and $H_2O$) are available in the Supporting Information.

## Discussion

The analysis of the QENS data obtained for $\beta$-$Ca(BH_4)_2$ has shown that, within the time scale accessible by the two instruments used, two types of thermally activated hydrogen dynamics were observable in the temperature range from 90 to 320 K. The first type is described by localized H motion, that is, reorientations of the $BH_4^-$ unit around the $C_2$-axis and $C_3$-axis. The experimental and DFT calculated energy barriers are in excellent agreement, giving $E_{aC2} = 0.14$ (0.15) eV and $E_{aC3} = 0.10$ (0.11) eV, experimental (calculated) values. The rotation about the $C_3$-axis is found to be energetically more favorable than the one around the $C_2$-axis.

The second type of hydrogen dynamics could not be described by rotational diffusion. With a Chudley−Elliot type $Q$-dependent broadening (nonlocalized event) giving a characteristic jump length of ∼2.5 Å, in agreement with the shortest H−H distance between two $BH_4^-$ groups, a likely event would thus be a hydrogen-vacancy jump between neighboring groups. Nevertheless, the DFT results for this process indicated a slightly shorter jump length 2.1 Å, with the $BH_3$ complex becoming planar, a higher energy barrier 0.46 eV, versus ∼0.12 eV experimentally, and a high energy for the formation of the vacancy (2.09 eV). All other vacancy-mediated diffusion mechanisms were also discarded because of their high energies of formation, thus interstitial H, $H_2$, and $H_2O$ diffusions were studied. $H_2$ interstitial diffusion gave results (0.09 eV, 2.1 Å) with the best agreement to the experimental one (∼0.12 eV, ∼2.5 Å). Nevertheless, this latter result was obtained from only two experimental points, and the $H_2O$ interstitial diffusion cannot be strictly discarded. A possible explanation of the origin of $H_2$ and/or $H_2O$ interstitials is that they are formed during the synthesis of the compound. The MS measurement did not show any trace of water nor of oxygen, and the small release of hydrogen below 565 K correlates with the formation of an oxide phase. Given the oxygen free environment, the oxide possibly results from a reaction of the hydride with trapped interstitial water, or even THF, forming interstitial hydrogen that subsequently desorbs.

In $LiBH_4$, motion of entire $BH_4^-$ units has been identified as the main mass transport mechanism above the melting temperature,[45,46] whereas at low temperatures, a net transport of atomic hydrogen, probed by hydrogen/deuterium exchange, was also observed, although at a very low rate.[47,48] From the results presented in this study, no such hydrogen dynamics have been detected, and it will be too speculative to conclude here that the observed translational diffusion of hydrogen is part of the mechanism for the bulk decomposition of $Ca(BH_4)_2$. The correlation between the QENS and DFT calculations indicates that, most probably, it is the diffusion of interstitial $H_2$ that was observed; but it is probably due to a side reaction with trapped synthesis residue, leading to the partial oxidation of the compound and hydrogen release.

The combined DFT−QENS approach has been shown to be very useful both in the interpretation of the data and to determine crucial quantities useful to develop new experiments including the characteristic times and the energies barriers.

**Acknowledgment.** This work is based on experiments performed at the Swiss spallation neutron source SINQ, Paul Scherrer Institute, Villigen, Switzerland and at FRMII, JCNS Garching, Germany. The authors would like to acknowledge the European Graduate School for Sustainable Energy Technology and the Nordic Center for Excellence on Hydrogen Storage Materials. The Danish Center for Scientific Computing is acknowledged for super-computer access. The Center for Atomic Materials Design (CAMD) is supported by the Lundbeck Fondation. Financial support by EU-IP NESSHY (Contract #518271) and the ERA-NET project Hy-CO is also gratefully acknowledged.

**Supporting Information Available:** Initial and final coordinates of the species (interstitials $H_2$ and $H_2O$) to diffuse together with plots of the surrounding atoms. This material is available free of charge via the Internet at http://pubs.acs.org.

## References and Notes

(1) Züttel, A.; Rentsch, S.; Fischer, P.; Wenger, P.; Sudan, P.; Mauron, P.; Emmenegger, C. *J. Alloy. Compd.* **2003**, *356−357*, 515.
(2) Nakamori, Y.; Miwa, K.; Ninomiya, A.; Li, H.; Ohba, N.; Towata, S.-I.; Züttel, A.; Orimo, S.-I. *Phys. Rev. B* **2006**, *74*, 045126−1.
(3) Miwa, K.; Aoki, M.; Noritake, T.; Ohba, N.; Nakamori, Y.; Towata, S.-I.; Züttel, A.; Orimo, S.-I. *Phys. Rev. B* **2006**, *74*, 155122–1.
(4) Severa, G.; Rönnebro, E.; Jensen, C. M. *Chem. Commun.* **2010**, *46*, 421.
(5) Rönnebro, E.; Majzoub, E. H. *J. Phys. Chem. B.* **2007**, *111*, 12045.
(6) Kim, J.-H.; Shim, J.-H.; Cho, Y. W. *J. Power Sources* **2008**, *181*, 140.
(7) Barkhordarian, G.; Jensen, T. R.; Doppiu, S.; Rösenberg, U.; Borgschulte, A.; Gremaud, R.; Cerenius, Y.; Dornheim, M.; Klassen, T.; Bormann, R. *J. Phys. Chem. C* **2008**, *112*, 2743.
(8) Bée, M. *Quasielastic Neutron Scattering*; Adam Hilger: Philadelphia, PA, 1988.
(9) Richter, D.; Hempelmann, R.; Vinhas, L. A. *J. Less Common Met.* **1982**, *88* (2), 353.
(10) Campbell, S. I.; Kemali, M.; Ross, D. K.; Bull, D. J.; Fernandez, J. F.; Johnson, M. R. *J. Alloys Compd.* **1999**, *293−295*, 351.
(11) Skripov, A. V.; Udovic, T. J.; Rush, J. J. *Phys Rev. B* **2007**, *76*, 104305–1.

(12) Skripov, A. V.; Udovic, T. J.; Cook, J. C.; Hempelmann, R.; Rempel, A. A.; Gusev, A. I. *J. Phys.: Condens. Matter* **2009**, *21*, 175410–5.

(13) Voss, J.; Shi, Q.; Jacobsen, H. S.; Lefmann, K.; Zamponi, M.; Vegge, T. *J. Phys. Chem. B.* **2007**, *111*, 3886.

(14) Remhof, A.; Łodziana, Z.; Butcher, F.; Martelli, P.; Pendollino, F.; Friedrichs, O.; Züttel, A.; Embs, J. P. *J. Phys. Chem.* **2009**, *113*, 16834.

(15) Verdal, N.; Hartman, M. R.; Jenkins, T.; DeVries, D. J.; Rush, J. J.; Udovic, T. J. *J. Phys. Chem. C* **2010**, *114*, 10027.

(16) Butcher, F.; Łodziana, Z.; Remhof, A.; Friederichs, O.; Borgschulte, A.; Mauron, P.; Züttel, A.; Sheptyakov, D.; Barkhordarian, G.; Bormann, R.; Chlopek, K.; Fichtner, M.; Sørby, M.; Riktor, M.; Hauback, B.; Orimo, S. *J. phys. Chem. B* **2008**, *112*, 8042.

(17) Filinchuk, Y.; Rönnebro, E.; Chandra, D. *Acta Mater.* **2009**, *57*, 732.

(18) Łodziana, Z.; Vegge, T. *Phys. Rev. Let.* **2004**, *93* (14), 145501.

(19) Łodziana, Z.; Vegge, T. *Phys. Rev. Let.* **2006**, *97* (11), 119602.

(20) Filinchuk, Y.; Chernyshov, D.; Cerný, R. *J. Phys. Chem. C* **2008**, *112*, 10579.

(21) Riktor, M. D.; Sørby, M. H.; Chlopek, K.; Fichtner, M.; Buchter, F.; Züttel, A.; C., H. B. *J. Mater. Chem.* **2007**, *17*, 4939.

(22) Hunter, B. *IUCR Powder Diffraction Newsletter,* **1998**, 20.

(23) Wuttke, J. To be published; http://www.jcns.info/jcns_spheres.

(24) http://sinq.web.psi.ch/sinq/instr/mars.html.

(25) Wuttke, J. http://www.messen-und-deuten.de/slaw.

(26) Azuah, R. T.; Kneller, L. R.; Qiu, Y.; Tregenna-Piggott, P. L. W.; Brown, C. M.; Copley, J. R. D.; Dimeo, R. M. *J. Res. Natl. Inst. Stan. Technol.* **2009**, *114*, 341.

(27) Bahn, S. R.; Jacobsen, K. W. *Comput. Sci. Eng.* **2002**, *4*, 56.

(28) Hammer, B.; Hansen, L. B.; Nørskov, J. K. *Phys. Rev. B* **1999**, *59*, 7413.

(29) Kohn, W.; Sham, L. J. *Phys. Rev.* **1965**, *140*, 1133.

(30) Vanderbilt, D. *Phys. Rev. B* **1990**, *41*, 7892.

(31) Perdew, J. P.; Chevary, J. A.; Vosko, S. H.; Jackson, K. A.; Pederson, M. R.; Singh, D. J.; Fiolhais, C. *Phys. Rev. B* **1992**, *46*, 6671.

(32) Liu, D. C.; Nocedal, J. *Math. Program.* **1989**, *45*, 503.

(33) Henkelman, G.; Uberuaga, B. P.; Jonsson, H. *J. Chem. Phys.* **2000**, *113*, 9901.

(34) Bitzek, E.; Koskinen, P.; Gähler, F.; Moseler, M.; Gumbsch, P. *Phys. Rev. Lett.* **2006**, *97*, 170201.

(35) Vineyard, G. H. *J. Phys. Chem. Solids* **1957**, *3*, 121.

(36) Maoa, J.; Guoa, Z.; Poha, C. K.; Ranjbara, A.; Guoc, Z.; Yuc, X.; Liua, H. *J. All. Compd.* **2010**, *500*, 200.

(37) Kim, Y.; Reed, D.; Lee, Y.-S.; Lee, J. Y.; Shim, J.-H.; Book, D.; Cho, Y. W. *J. Phys. Chem. C* **2009**, *113*, 5865.

(38) Riktor, M. D.; Sørby, M. H.; Chlopek, K.; Fichtner, M.; B.C., H. *J. Mater. Chem.* **2009**, *19*, 2754–2759.

(39) RiktorM, M. D. To be published.

(40) Levingston, R. C.; Rowe, J. M.; Rush, J. J. *J. Chem. Phys.* **1974**, *60*, 4541.

(41) Wolf, D. *Solid State Commun.* **1977**, *23*, 853.

(42) Didisheim, J. J.; Yvon, K.; Shaltiel, D.; Fischer, P. *Solid State Commun.* **1979**, *31*, 47.

(43) Dickens, M. H.; Hayes, W.; Schnabel, P.; T., Hutchings M.; Lechner, R. E.; Renker, B. *J. Phys. C: Solid State Phys.* **1983**, *16*, L1.

(44) Bender, O.; Schroeder, K. *Phys. Rev. B* **1979**, *19*, 3399.

(45) Schoenflies, A. *Math. Ann.* **1889**, *34*, 172.

(46) Shane, D. T.; Bowman, R. C.; Conradi, M. S. *J. Phys. Chem. C* **2009**, *113*, 5039.

(47) Corey, R. L.; Shane, D. T.; Bowman, R. C.; Conradi, M. S. *J. Phys. Chem. C.* **2008**, *112*, 18706.

(48) Borgschulte, A.; Züttel, A.; Hug, P.; Racu, A. M.; Schoenes, J. *J. Phys. Chem. A* **2008**, *112*, 4749.

(49) Gremaud, R.; Łodziana, Z.; Hug, P.; Willenberg, B.; Racu, A.-M.; Schoenes, J.; Ramirez-Cuesta, A. J.; Clark, S. J.; Refson, K.; Züttel, A.; Borgschulte, A. *Phys. Rev. B* **2009**, *80*, 100301–1.

JP107281V

THE JOURNAL OF PHYSICAL CHEMISTRY C

ARTICLE

pubs.acs.org/JPCC

# Hindered Rotational Energy Barriers of $BH_4^-$ Tetrahedra in $\beta$-$Mg(BH_4)_2$ from Quasielastic Neutron Scattering and DFT Calculations

D. Blanchard,[*,†] J. B. Maronsson,[†,‡] M. D. Riktor,[§] J. Kheres,[†] D. Sveinbjörnsson,[†] E. Gil Bardají,[∥] A. Léon,[∥] F. Juranyi,[⊥] J. Wuttke,[#] K. Lefmann,[▽] B. C. Hauback,[§] M. Fichtner,[∥] and T. Vegge[†]

[†]Materials Research Division, Risø National Laboratory for Sustainable Energy, Technical University of Denmark, Building 228, P.O. Box 49, DK-4000 Roskilde, Denmark

[‡]Center for Atomic Scale Materials Design, Technical University of Denmark, DK-2800 Lyngby, Denmark

[§]Physics Department, Institute for Energy Technology, P.O. Box 40, NO-2027 Kjeller, Norway

[∥]Institute of Nanotechnology, Karlsruhe Institute of Technology (KIT), P.O. Box 3640, D-76021 Karlsruhe, Germany

[⊥]Laboratory for Neutron Scattering, ETH Zurich and Paul Scherrer Institute, CH-5232 Villigen PSI, Switzerland

[#]Forschungszentrum Jülich, JCNS at FRM II, Lichtenbergstrasse 1, 85747 Garching, Germany

[▽]Nanoscience Center, Niels Bohr Institute, Universitetsparken 5, bygn. D., Dk-2100 København Ø. European Spallation Source, St. Algatan 4, 22100 Lund, Sweden

**ABSTRACT:** In this work, hindered rotations of the $BH_4^-$ tetrahedra in $Mg(BH_4)_2$ were studied by quasielastic neutron scattering, using two instruments with different energy resolution, in combination with density functional theory (DFT) calculations. Two thermally activated reorientations of the $BH_4^-$ units, around the 2-fold ($C_2$) and 3-fold ($C_3$) axes were observed at temperatures from 120 to 440 K. The experimentally obtained activation energies ($E_{aC_2}$ = 39 and 76 meV and $E_{aC_3}$ = 214 meV) and mean residence times between reorientational jumps are comparable with the energy barriers obtained from DFT calculations. A linear dependency of the energy barriers for rotations around the $C_2$ axis parallel to the Mg−Mg axis with the distance between these two axes was revealed by the DFT calculations. At the lowest temperature (120 K) only 15% of the $BH_4^-$ units undergo rotational motion and from comparison with DFT results it is expectedly the $BH_4^-$ units with the boron atom closest to the Mg−Mg axis, although dynamics related to local disorder existing at the boundary of the antiphase domains or to the presence of solvent in the sample cannot be strictly excluded. No long-range diffusion events were observed.

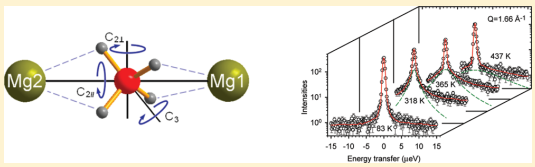


## INTRODUCTION

Metal borohydrides are of interest as hydrogen storage materials due to their high volumetric and gravimetric capacity. However, as with many of the complex hydrides, they are hampered by slow absorption and desorption kinetics and poor reversibility.[1−3]

Among the borohydrides, $Mg(BH_4)_2$ (Figure 1) and $Ca(BH_4)_2$ have more favorable thermodynamic stability than, for example, $LiBH_4$, while maintaining attractive hydrogen storage capacities (14.9 and 11.5 mass %, respectively).[2,4] Furthermore, for these two compounds, partial reversibility has been obtained by utilizing high pressure[5−7] (60%[7]−70%[6] recovery of the borohydride) and in the case of $Ca(BH_4)_2$ at more moderate conditions by addition of catalysts (60% recovery[8]). Kinetic properties have also been shown to improve by using composite materials like $Ca(BH_4)_2 + MgH_2$.[9]

Borohydrides are largely ionic compounds with a general formula $M(BH_4)_n$, consisting of metal cations $M^{n+}$, the hydrogen atoms being covalently bound to the boron, forming tetrahedral $BH_4^-$. The possible hydrogen dynamics are long-range translational diffusion and localized motions such as rotations of the $BH_4^-$ complexes along specific axes, librations of the complexes, and vibrations within the complexes. Rotational dynamics are often coupled to order−disorder phase transition in coordination compounds,[10,11] and the decomposition of borohydrides could possibly involve long-range diffusion of H and/or of the whole $BH_4^-$ complex. The first results published on the rotational reorientation of the $BH_4^-$ unit in borohydrides date back to the 1950s. At that time, researchers were interested in understanding the nature of the interactions influencing molecular reorientations in solids. To our knowledge, the first experimental study ever published, giving the energy barriers for the reorientations of $BH_4^-$ in sodium, potassium, and rubidium borohydrides, was performed using nuclear magnetic resonance (NMR) and date from 1955,[12] while a second was published on lithium, sodium, and potassium borohydrides 14 years after,

**Received:** September 8, 2011
**Revised:** November 21, 2011
**Published:** November 22, 2011

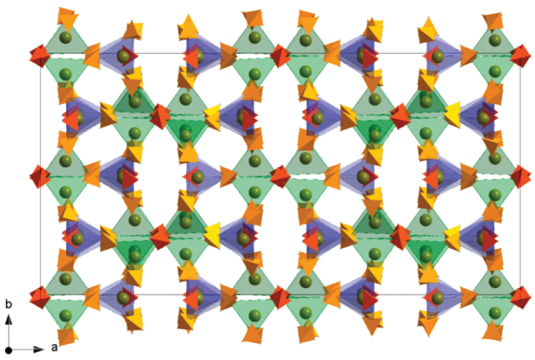


**Figure 1.** The idealized structure of $\beta$-$Mg(BH_4)_2$, space group *Fddd*,[33] viewed along the *c* axis: spheres, Mg atoms; $Mg_1$—B tetrahedra, green; $Mg_2$—B tetrahedra, blue; B0*i*—H tetrahedra (*i* = 1, 2, 4), orange; B0*j*—H tetrahedra (*j* = 3, 5) red (see Table 2).

in 1969.[13] Then, using the theoretical developments made by King,[14] the barrier heights in potential functions hindering the rotation of the borohydride group were obtained from measurement of the heat capacity of the solid phases.[15] Later on, more NMR studies were published on different compounds: $NaBH_4$,[16−18] $LiBH_4$,[19] $\alpha$-$Mg(BH_4)_2$,[20] $KBH_4$,[18] and $La(BH_4)_3$.[21] It is only recently that quasielastic neutron scattering (QENS) measurements have been performed on borohydrides and the reorientation of the $BH_4^-$ unit studied for $NaBH_4$, $LiBH_4$, $KBH_4$, and $\beta$-$Ca(BH_4)_2$.[22−28] Inelastic neutron scattering measurements have also been used to probe the librational[29,30] and rotational[29] properties of some borohydrides. The measurements conducted on $Ca(BH_4)_2$ gave evidence for librational modes as the origin of phase transformations and emphasized the importance of the contribution of the vibrational entropy to the stability of the different polymorphs.[30]

Noting, still, the lack of knowledge about the structural transition and decomposition mechanisms in borohydrides, we have investigated the hindered rotation of the $BH_4^-$ units, using QENS, in magnesium borohydride. This method is optimal to study hydrogen dynamics due to the large incoherent scattering cross section of hydrogen compared to all other scattering signals.[31]

At least two different polymorphs of unsolvated $Mg(BH_4)_2$ have been observed experimentally: a low-temperature metastable $\alpha$ phase[32,33] and a high-temperature $\beta$ phase.[33] Other polymorphs were also observed using different procedure of synthesis[34] or high static pressure.[35] Furthermore, density functional theory calculations predict the existence of other stable or metastable structures.[36−38] The $\alpha$ and $\beta$ phases can be obtained separately or as a mixture depending on the synthesis conditions. The $\alpha$ phase, metastable below 453 K, will transform into the $\beta$ phase and then decompose with hydrogen release through a multistep process.[39] The $\beta$ phase is stable up to 613 K and when cooled to room temperature.[40] It is this polymorph that has been used for the quasielastic neutron scattering measurements.

The aim of the study was to investigate the hindered rotation of the $BH_4^-$ tetrahedra. For that purpose, QENS measurement combined with density functional theory (DFT) calculations have been successfully applied, and the results are discussed in connection with the structural features of this borohydride.

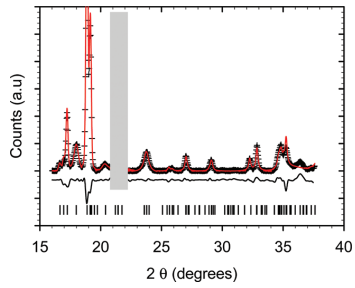


**Figure 2.** The XRD pattern of the as-prepared $\beta$-$Mg(BH_4)_2$. The dots are the experimental points, the line is the refined pattern based on the Rietveld method, and the bottom line is the difference between the experimental and the refined pattern. The ticks are the position of the Bragg peaks. The shadowed area corresponds to a broad peak due to the plastic film used to cover the sample. It is removed from the experimental data.

## MATERIAL AND EXPERIMENTAL METHODS

Natural B contains 20% $^{10}B$, which has a high absorption cross section. Therefore, to reduce neutron absorption, $Mg(BH_4)_2$ was synthesized via the metathesis reaction of eq 1 using a $^{11}B$-enriched precursor ($^{10}B$ cross section: 3837 barns versus $5.5 \times 10^{-3}$ barns for $^{11}B$).

$$2Na^{11}BH_4 + MgCl_2 \rightarrow Mg(^{11}BH_4)_2 + 2NaCl \qquad (1)$$

A 2.50 g (0.066 mol) portion of $Na^{11}BH_4$ (purchased from Katchem Ltd., purity 99.8%) was first ball-milled for 4 h in a Fritsch P6 planetary mill at 600 rpm, with a ball to powder ratio of 25:1, and then added to 2.95 g (0.031 mol) of $MgCl_2$ (purchased from Sigma Aldrich, purity 98%) in 80 mL of diethyl ether ($Et_2O$). The mixture was heated under reflux at 40 °C overnight. After cooling down to room temperature, the suspension was filtered off and the filtrate was evaporated under vacuum to remove the solvent. The resulting $Mg(^{11}BH_4)_2 \cdot n Et_2O$ adduct was then dried under vacuum at 80 °C for 12 h. The white solid was manually ground in a mortar and subsequently dried under vacuum at 180 °C for 12 h to obtain $\beta$-$Mg(BH_4)_2$ as a single phase with an isolated yield (with respect to $MgCl_2$) of 1.25 g (74%).

A powder X-ray diffraction pattern (PXD) was recorded with a BRUKER D8 diffractometer (40 kV, 40 mA, Cu radiation K$\alpha$ = 1.542 Å) (See Figure 2). The pattern consists of several broad and sharp peaks. The broad peaks correspond to the ($2n + 1$, $2n + 1$, $2n + 1$) reflections of the proposed *Fddd* structure.[33] In that structure, the crystal, an almost purely ionic system,[41] consists of corner-sharing tetrahedra with $Mg^{2+}$ ions at the center and $BH_4^-$ units at the vertices. Two boron atoms reside on the (16e, 16g) Wyckoff positions and the three others as well as the magnesium and hydrogen atoms occupy the (32h) Wyckoff general positions, resulting in five crystallographically inequivalent $BH_4^-$ groups. Each of the two Mg tetrahedra is bonded to one tetrahedron with B at the 16e or 16g sites and three tetrahedra with B at the 32h sites. The B atoms are surrounded by two Mg atoms in a planar, almost linear configuration, and the Mg—B—Mg angles and Mg—B or Mg—Mg distances depend on the B sites (Table 1). The $BH_4^-$ tetrahedra have bidentate orientations with two H atoms pointing toward Mg. To explain the broadening of the ($2n + 1$, $2n + 1$, $2n + 1$) reflections, Her et al.[33] suggested the existence of an antiphase boundary modification of

**Table 1. $\beta$-$Mg(BH_4)_2$ Structural Parameters Obtained from Rietveld Refinement of PXD Pattern and DFT Calculations[a]**

| space group *Fddd* (No. 70); $Z = 64$ | | | |
|---|---|---|---|
| DFT | $a$ = 37.231 00 Å | $b$ = 18.93 Å | $c$ = 10.937 Å |
| PXD | 37.14(6) | 18.65(6) | 10.91(6) |
| ref 33 | 37.0720(10) | 18.6476(6) | 10.9123(3) |
| site | $x/a$ | $y/b$ | $z/c$ |
| Mg1/32 h | 0.0763 (0.077)[b] | 0.2412 (0.250) | 0.5349 (0.5381) |
| Mg2/32h | 0.0538 (0.052) | 0.9299 (0.929) | 0.7565 (0.746) |
| B01/32h | 0.4439 (0.444) | 0.6372 (0.647) | 0.5663 (0.560) |
| B02/32h | 0.1074 (0.107) | 1.0025 (1.008) | 0.22306 (0.263) |
| B03/16e | 0.3133 (0.312) | 0 (0) | 0 (0) |
| B04/32h | 0.4444 (0.446) | 0.1654 (0.153) | 0.4046 (0.410) |
| B05/16g | 0 (0) | 0 (0) | 0.7275 (0.773) |
| atom | Mg−Mg (Å)[c] | Mg−B−Mg (deg)[c] | $L$ (Å)[d] |
| B01 | 4.77 | 161.87 | 0.68 |
| B02 | 4.62 | 144.33 | 0.73 |
| B03 | 4.71 | 156.86 | 0.47 |
| B04 | 4.77 | 161.93 | 0.38 |
| B05 | 4.80 | 172.52 | 0.16 |

[a] In both cases, the starting values were taken from ref 33. During Rietveld refinements, the atomic positions were not refined. [b] Numbers in brackets: parameters from ref 33. [c] Angles and distances calculated from the DFT relaxed structure. [d] Distance of the boron atom to the middle point of the Mg−Mg segment.

the *Fddd* super structure, coherent over long distances in the *bc* planes but with frequent defects in the *a* direction. These reflections were excluded for the Rietveld refinement performed with the Rietica software.[42] The final fit was then obtained from the superposition of the Rietveld fit and individual fits of the $(2n + 1, 2n + 1, 2n + 1)$ peaks with Voigt profiles (Figure 2). The atomic positions were kept fixed and only the cell parameters were refined. They are in good agreement with those found in ref 33 and those calculated by DFT for the *Fddd* structure (see Table 1). No other crystalline phases could be identified, but the presence of an unexplained broad peak (at 36.4°), together with some small mismatch in the peak intensities, is an indication of the presence of impurities in the compound.

Mass spectrometry measurements (MS), using an OmniStar (GSD 320) mass spectrometer, were performed on the gas released by the sample when heated under dynamical vacuum from room temperature up to 723 K (heating ramp of 1 K $min^{-1}$) (Figure 3). The signal for hydrogen showed several peaks in the temperature range 450−650 K, illustrating the multistep thermal decomposition process. The analysis of the measurement shows that $H_2$ accounts for ∼96% of the released gas and $Et_2O$ ∼4%, the amount of $H_2O$, $B_2H_6$, and other gases like $O_2$ being negligible (≪1%). Thus, the amount of solvent left in the sample after its synthesis is rather low, but its contribution to the total H atomic content is not negligible. The sample appeared to be water-free.

QENS experiments were performed with two complementary instruments, SPHERES and MARS, in order to cover a wide energy range thanks to the two different energy resolutions. SPHERES[43] is a high-resolution neutron backscattering spectrometer located at FRM II (Forschungs-Neutronenquelle Heinz Maier-Leibnitz),

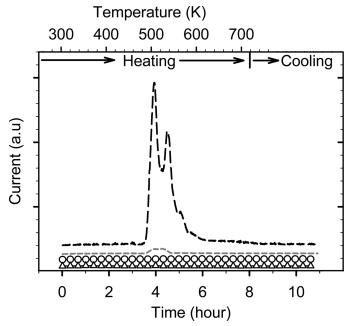


**Figure 3.** Mass spectrometry measurements. The sample was heated under dynamical vacuum from room temperature up to 723 K at a heating ramp of 1 K $min^{-1}$: (— —) $H_2$ signal, (— —) $Et_2O$ signal, (-○-) $B_2H_6$ signal, and (-△-) $H_2O$ signal.

Garching, Germany. MARS[44] is an inverted geometry time-of-flight spectrometer located at the Swiss Spallation Neutron Source (SINQ), Paul Scherrer Institute, Villigen, Switzerland.

The experiments at SPHERES were performed with ∼0.08 g of $Mg(^{11}BH_4)_2$, which was loaded in an Al-wire-sealed, flat 30 × 40 × 0.5 $mm^3$ Al container oriented at 135° with respect to the direct beam. Si(111) monochromator and analyzer crystals were used in a backscattering geometry, giving a final neutron wavelength of 6.271 Å and an energy resolution of 0.65 $\mu$eV with an energy transfer range selected of ±15.8 $\mu$eV. The spectra were recorded by nine detectors corresponding to a scattering vector ranging from 0.59 to 1.66 $Å^{-1}$. The data reduction was carried out with the SLAW package.[45]

The experiments at MARS were performed with ∼0.3 g of $Mg(^{11}BH_4)_2$, from the same batch, which was loaded in a double-walled Al container with height of 60 mm and inner and outer diameters of 9 and 10 mm, respectively. The spectra were recorded by five detectors on both sides of the instrument, corresponding to a scattering vector ranging from 0.49 to 1.86 $Å^{-1}$. Mica(006) analyzers were used in a backscattering geometry, giving a final neutron wavelength of 6.65 Å and an energy resolution of 13 $\mu$eV. The energy transfer window was chosen differently, depending on the width of the quasielastic signal, the largest being from −0.04 to 0.43 meV. The data reduction was carried out with the DAVE package.[46]

## ■ DENSITY FUNCTIONAL THEORY CALCULATIONS

Theoretical calculations were used to identify the rate of possible dynamic events by calculating their energy barriers and prefactors. The calculations were performed using the Atomic Simulation Environment (ASE) package.[47] The DACAPO plane wave basis set implementation[48] was used to solve the electronic structure problem within the density functional theory (DFT) formalism.[49] The ion cores were described by ultrasoft pseudopotentials[50] and the exchange and correlation effects were described by the PW91 functional.[51] The Kohn−Sham wave functions were expanded in a plane wave basis set with a cutoff energy of 350 and 600 eV for the density grid cutoff. The calculational cell contained 16 $Mg(BH_4)_2$ formula units, totaling 176 atoms in the $\beta$-phase structure,[33] no symmetry constraints were applied during its optimization. The wave functions were sampled using only the gamma point, which is well justified with

**Table 2. Summary of the Experimental (QENS) Results for $\beta$-$Mg(BH_4)_2$**

| | MARS | |
|---|---|---|
| | Γ (meV) | |
| temp (K) | $L_1$ | $L_2$ |
| 120 | $5 \times 10^{-3}$ | – |
| 150 | $11 \times 10^{-2}$ | $7.5 \times 10^{-3}$ |
| 180 | $18 \times 10^{-2}$ | $24 \times 10^{-3}$ |
| 210 | $25 \times 10^{-2}$ | $45 \times 10^{-3}$ |
| 240 | $32 \times 10^{-2}$ | $76 \times 10^{-3}$ |
| | SPHERES | |
| temp (K) | $L_1$ | |
| 83 | – | |
| 318 | $1.94 \times 10^{-3}$ | |
| 365 | $5.11 \times 10^{-3}$ | |
| 437 | $16.2 \times 10^{-3}$ | |

such a large cell. Iterative relaxation using the limited memory Broyden–Fletcher–Goldfarb–Shanno algorithm[52] was employed to obtain the ground state structure and unit cell parameter to a convergence of 0.001 eV/Å. The nudged elastic band (NEB) method,[53] along with the FIRE minimization algorithm,[54] was used to locate first-order saddle point configurations, to a convergence of 0.01 eV/Å, connecting two local minima. Within harmonic transition state theory (hTST),[55] these configurations are used to determine the thermally activated reaction rates $[r(T)]$, i.e., the barrier height ($E_a$) and the vibrational frequencies at the initial ($\nu^{IS}$) and saddle points ($\nu^{TS}$):

$$r(T) = \frac{\prod_{i=1}^{3N} \nu_i^{IS}}{\prod_{i=1}^{3N-1} \nu_i^{TS}} e^{-E_a/k_B T} \quad (2)$$

The vibrational frequencies were acquired using a finite difference approximation of the Hessian matrix (back and forward displacements of 0.01 Å). The term outside the exponential in eq 2, often referred as the prefactor, compares the vibrational frequencies at the initial state and saddle point. The characteristic times displayed in Table 3 are the reciprocal values of these prefactors.

## RESULTS

**Quasielastic Neutron Scattering Spectra.** Quasielastic temperature scans were performed with the two instruments. For each temperature, the spectra collected on each detector were summed to get one spectrum. The elastic intensities were obtained by adding up the counts with an energy transfer of $|\delta E| \leq 8\ \mu$eV (MARS) and $\leq 0.32\ \mu$eV (SPHERES). The quasielastic intensities were deduced by summing up the counts outside the elastic regions. Figure 4 displays the evolution with temperature of the normalized elastic ($I_{N\text{-el}}$) and quasielastic ($I_{N\text{-qel}}$) scattering measured at MARS and SPHERES.

At MARS, the sample was heated from 70 to 520 K and at 70 K no quasielastic broadening was detected since the hydrogen is "frozen in" on the time scale accessible with the instrument. On heating between 70 and 220 K, $I_{N\text{-el}}$ ($|\delta E| \leq 8\ \mu$eV) decreased

**Table 3. Summary of the Experimental (QENS) and Computational (DFT) Results for $\beta$-$Mg(BH_4)_2$**

| | | $\tau_0$ ($\times 100$ ps)[a] | | $^aE_a$ (meV)[a] | |
|---|---|---|---|---|---|
| | | $C_2$ | $C_3$ | $C_2$ | $C_3$ |
| MARS | | $61 \pm 0.3$ | – | $39 \pm 0.5$ | – |
| | | $46 \pm 0.15$ | – | $76 \pm 5$ | – |
| SPHERES | | – | $21 \pm 0.3$ | – | $214 \pm 4$ |
| DFT | B01 | 15 | 1 | 82 | 298 |
| | B02 | 26 | 5 | 96 | 185 |
| | B03 | 17 | 3 | 60 | 170 |
| | B04 | 14 | 6 | 54 | 125 |
| | B05 | 25 | 4 | **28** | 208 |

[a] $\tau_0$ and $E_a$ experimental values were calculated from the Arrhenius fits $[\Gamma = \Gamma_0 \exp(-E_a/k_B T)]$ of the experimental Lorentzian broadening and using eqs 6 and 7.

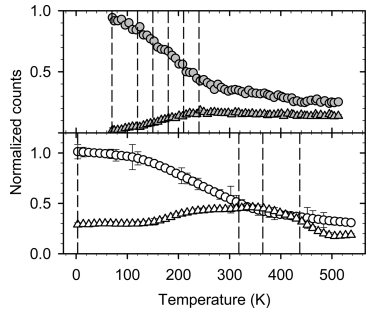


**Figure 4.** The normalized elastic and quasielastic intensities ($I_{N\text{-el}}$ and $I_{N\text{-qel}}$) during temperature scans: circles, $I_{N\text{-el}}$; triangles, $I_{N\text{-qel}}$; filled symbols, MARS intensities on heating from 70 to 520 K; open symbols, SPHERES intensities on heating from 3 to 540 K. The vertical lines are the temperatures at which the QENS spectra were measured.

while $I_{N\text{-qel}}$ ($|\delta E| > 8\ \mu$eV) slowly increased. The maximum $I_{N\text{-qel}}$ is at 220 K, followed by a plateau upon heating to the highest temperature. After the maximum, the hydrogen motion is too fast and the quasielastic broadening too large and thus partly falling outside the energy window chosen for MARS. The same intensity evolutions were observed when the sample was cooled back to 70 K, with a full recovery of the elastic intensity indicating no hydrogen desorption.

At SPHERES, the temperature scan from 10 to 540 K (Figure 4) was only performed during heating. In the temperature range from 10 to 120 K, the elastic intensity ($|\delta E| \leq 0.32\ \mu$eV) decreased slowly while the quasielastic one ($|\delta E| > 0.32\ \mu$eV) remained constant (measure of the background). At around 120 K, $I_{N\text{-el}}$ decreased faster while $I_{N\text{-qel}}$ started to increase with a maximum at 350 K and a decrease afterward. It then flattened out at around 500 K. At this temperature, the hydrogen motion gives rise to too large broadening for the instrument energy window. The temperatures to perform the detailed measurements were selected from these scans (see Table 2).

The QENS spectra were analyzed by using the curve fitting utility (PAN) included in the DAVE package. They consist of one elastic and some quasielastic components. The elastic component comes from the scattering process with no change in the

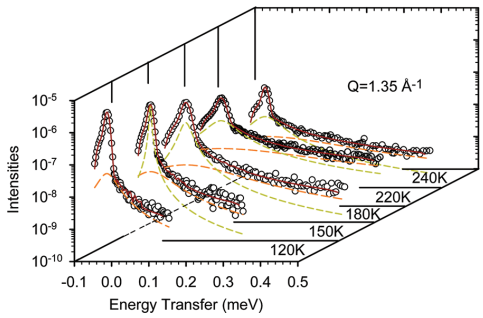


**Figure 5.** The QENS spectra of $\beta$-$Mg(BH_4)_2$ measured with MARS at different temperatures for $Q = 1.35$ Å$^{-1}$. The dots are the experimental data. The solid brown lines display the fits of the data, each consisting of a resolution broadened delta function, one or two Lorentzians (dashed light green and orange lines), and a flat background (not shown on the plots).

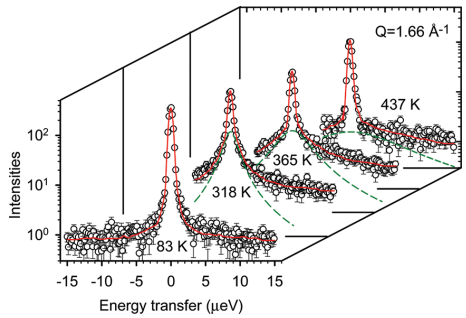


**Figure 6.** The QENS spectra of $\beta$-$Mg(BH_4)_2$ measured with SPHERES at different temperatures for $Q = 1.66$ Å$^{-1}$. The dots are the experimental data. The solid red lines display the fits of the data, each consisting of a resolution broadened delta function, a Lorentzian (dashed green lines), and a flat background (not shown on the plots).

neutron energy, while the quasielastic component reflects the energy transfer, gain and loss, due to the hydrogen motions. The measured total incoherent scattering function, $S_{inc}^{tot}(Q,\omega)$, is given by (see e.g. ref 31 for more details)

$$S_{inc}^{tot}(Q,\omega) = R(Q,\omega) \otimes \left( A_0(Q)\,\delta(\omega) + \sum_i A_i(Q)\,L(\Gamma_i,\omega) \right) + B(Q) \quad (3)$$

where $R(Q,\omega)$ is the instrumental resolution and $\delta(\omega)$ is the Dirac delta function describing the elastic scattering. $L(\Gamma_i,\omega)$ are Lorentzian functions that model the quasielastic signal with $\Gamma_i$ = hwhm (half-width at half-maximum). The $B$ term represents the inelastic background in the quasielastic region. It can originate from processes that are much faster than those observable within the time scale of the instrument used. The term $A_0(Q)$ is the elastic incoherent structure factor (EISF)[31] and its dependence on $Q$, the wave vector transfer, is important, since it basically determines the static properties of the number of sites accessible to the hydrogen atoms, the locations of these sites, and the normalized probability to be at a given site. It is a measurable

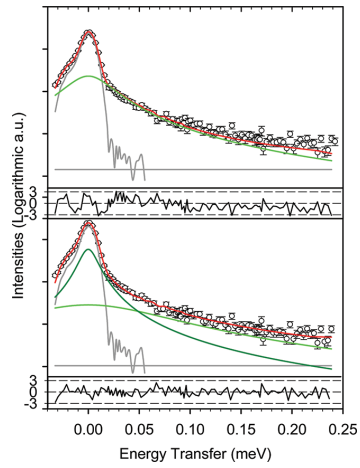


**Figure 7.** One QENS spectrum of $\beta$-$Mg(BH_4)_2$ measured with MARS at 180 K for $Q = 1.35$ Å$^{-1}$. The circles are the experimental data. The gray lines are the resolution function and the flat background, the green lines are the Lorentzian, and the red lines are the modeled spectra. The residuals of the fit are plotted below the spectra. The fit with one Lorentzian gives $\chi^2 = 2.8$ (upper plot), the fit with two Lorentzians ($L_1$: light green, $L_2$: dark green with $\Gamma_1 > \Gamma_2$) gives $\chi^2 = 1.7$ (lower plot).

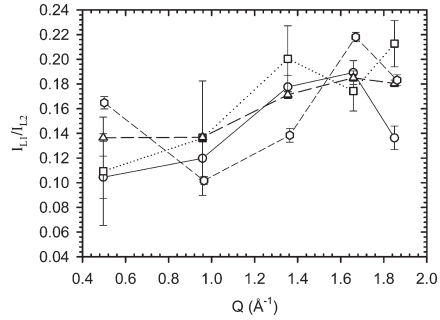


**Figure 8.** Ratio ($I_{L_1}/I_{L_2}$ with $\Gamma_1 > \Gamma_2$) versus the wave vector transfer $Q$ of the two Lorentzian intensities used to fit the spectrum measured with Mars at (○) 150 K, (□) 180 K, (△) 210 K, and (⬡) 240 K.

quantity, evaluated from the ratio

$$A_0(Q) = \frac{I_{el}(Q)}{I_{el}(Q) + I_{qel}(Q)} \quad (4)$$

where $I_{el}(Q)$ and $I_{qel}(Q)$ are the integrated intensities of the elastic and quasielastic signal, respectively.

Herein and following eq 3, the QENS spectra were analyzed with the resolution-limited elastic peak, the delta function folded with the instrumental resolutions, and one or two Lorentzians, although the existence of five different crystallographic sites for the boron atoms should formally require the use of five Lorentzian. This approach was used since any attempt to fit the spectrum with more than two quasielastic components led to numerical instabilities or unrealistic results. The instrumental resolutions were obtained from measurements at 3 K (SPHERES) and 70 K (MARS).

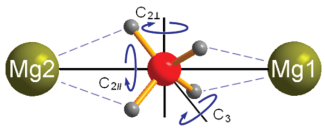


**Figure 9.** Schematic representation of the coordination environment, with the 2-fold $C_{2\parallel}$- and $C_{2\perp}$-axes and a 3-fold $C_3$-axis, of a $BH_4$ unit. From large to small size spheres: Mg, B, and H atoms. $C_{2\parallel}$ is the 2-fold axis in the direction of the Mg1−Mg2 axis, $C_{2\perp}$ is one of the axis perpendicular to the Mg1−Mg2 axis. The dashed lines represent the Mg−H bonds.

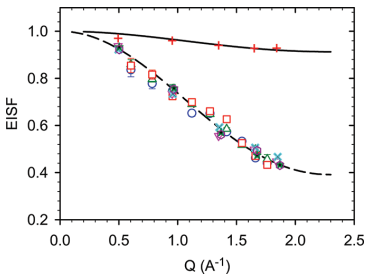


**Figure 10.** The measured and modeled EISFs: (---) $C_{2\parallel}$ (MARS data) and $C_3$ (SPHERES data) rotational diffusion model according to eq 5 and (—) according to eq 8. MARS: (red plus) 120 K, (blue x) 150 K, (red triangle) 180 K, (green asterisk) 210 K, and (black hexagon) 240 K. SPHERES: (red square) 318 K, (green triangle) 365 K, and (blue circle) 473 K.

At these temperatures no dynamical motion was observed on the time scale of the two instruments. The centers of the delta function and of the Lorentzian were constrained to be the same while their intensities were set free to adjust during the fitting procedure. For the measurements performed at MARS, since the energy window of the resolution function was smaller than those used for the measurements at higher temperatures, a flat fixed background was used. For the measurements performed with SPHERES, a flat background was used to model the too broad Lorentzian at high temperatures. Figures 5 and Figure 6 present typical examples of the spectra together with their fits with one or two Lorentzians. One Lorentzian was used to satisfactorily fit the spectra obtained with Mars at 120 K and SPHERES at 318, 365, and 437 K (typically with $\chi^2 < 2$). At higher temperatures, two Lorentzian ($L_1$ and $L_2$ with $\Gamma_1 > \Gamma_2$) were needed to fit the spectra obtained with Mars. Figure 7 displays a spectrum, for $Q = 1.35$ Å$^{-1}$, taken with MARS at 180 K. It emphasizes the need of two Lorentzians to obtain the best fit: with one Lorentzian, $\chi^2 = 2.8$ and with two, $\chi^2 = 1.7$. The analysis of the residual plots also confirms this latter point. In Figure 8 is plotted the ratio of the intensities of the two Lorentzians used to fit the spectra ($I_{L_1}/I_{L_2}$ versus $Q$). For the four temperatures, the ratio can be considered as constant with only a slight increase with $Q$ (from 0.14 to 0.18 on averages). A value of $0.16 \pm 0.02$ is obtained when averaging over all the values.

For all the temperatures, the widths of the Lorentzian functions were found to be $Q$-independent over the measured $Q$-range. This indicates that the observed quasielastic broadenings originated from localized hydrogen motion.[31] The first obvious localized motions are the rotations around the three 2-fold and four 3-fold axes of the $BH_4^-$ units. To simplify the description, taking a linear configuration for the Mg−B−Mg, the 2-fold axis having the direction of the Mg−Mg axis will be noted $C_{2\parallel}$, while the two perpendicular ones will be noted $C_{2\perp}$ (see Figure 9).

For $BH_4^-$ rotations around the $C_2$-axes, the tetrahedral ions have two equal equilibrium orientations and the EISF is thus given by[31]

$$A_0(Q) = \frac{1}{2}\left(1 + j_0\left(2\frac{\sqrt{2}}{\sqrt{3}}Qd\right)\right) \quad (5)$$

where $j_0(x) = \sin(x)/x$ is the zeroth-order spherical Bessel function and $d$ is the bond length between B and H. This rotation gives rise to one Lorentzian with a $Q$-independent hwhm of

$$\Gamma_{C_2} = 2\hbar\tau_2^{-1} \quad (6)$$

$\tau_2$ is the average time between two successive reorientational jumps around the $C_2$-axis, i.e., the average resident time of a hydrogen atom at a given site before jumping to a new site; thus its reciprocal value is the rotational frequency.

For $BH_4^-$ rotations around the $C_3$-axis, the tetrahedral ions have three equal equilibrium orientations and one hydrogen atom remains immobile. The expression for the EISF is identical to the rotation around the $C_2$-axes (eq 5).[31] It gives rise to one Lorentzian with a $Q$-independent hwhm of

$$\Gamma_{C_3} = \frac{3}{2}\hbar\tau_3^{-1} \quad (7)$$

$\tau_3$ represents the average resident time for the reorientation around the 3-fold axes; its reciprocal value is the rotational frequency.

In the case where not all of the tetrahedra participate in the $C_2$ or $C_3$ rotations, i.e., only a fraction $p$ of them undergoes the rotation, the EISF is expressed as

$$A_0(Q) = 1 - p + \frac{1}{2}p\left(1 + j_0\left(2\frac{\sqrt{2}}{\sqrt{3}}Qd\right)\right) \quad (8)$$

The experimental EISFs, extracted from the fitted QENS spectra (eq 4) provide strong evidence of the nature of the localized motion. Figure 10 displays the experimental and fitted EISFs. The model for the $C_2$ or $C_3$ hindered rotations (eq 5) follows the experimental data collected with MARS at 150, 180, 210, and 240 K and with SPHERES at 318, 365, and 437 K. The values for the best fits give $d = 1.22$ Å, which agrees with the average B−H distance obtained from DFT calculations. The model of eq 8 is used for the EISF of the measurement performed with MARS at 120 K, taking for granted that the dynamic events observed are also hindered rotation. In that case, only one Lorentzian was needed to fit the spectra. The B−H bond length, $d$, was kept constant ($d = 1.22$ Å) and the fitting parameter was $p$. A value of $p = 0.15$ is obtained; it is equivalent to say that, at this temperature, only 15% of the $BH_4^-$ tetrahedra undergo hindered $C_2$ or $C_3$ rotation detectable with the MARS instrument, the other tetrahedra being seen as immobile.

Figure 11 displays the averaged, over all detectors, hwhm values versus the temperatures, together with the fits of the Arrhenius expression

$$\Gamma = \Gamma_0 \exp\left(\frac{-E_a}{k_B T}\right) \quad (9)$$

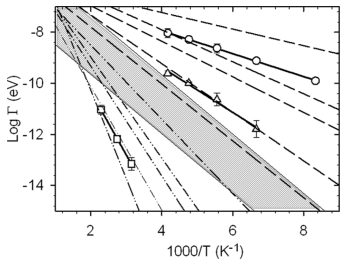


**Figure 11.** The thermally activated Arrhenius behavior of the hindered rotation of the $BH_4^-$ units in $\beta$-$Mg(BH_4)_2$. The squares are the SPHERES experimental averaged hwhm values. The triangles and circles are the MARS experimental averaged hwhm's. The averaged hwhm's are fitted as $\Gamma = \Gamma_0 \exp(-E_a/k_BT)$ with (○) $\Gamma_0$ = 2.14 meV, $E_a$ = 39 ± 0.5 meV and (Δ) $\Gamma_0$ = 2.86 meV, $E_a$ = 76 ± 5 meV attributed to $C_{2\|}$ rotations and (□) $\Gamma_0$ = 4.68 meV, $E_a$ = 214 ± 4 meV attributed to $C_3$ rotations. The dashed lines are the theoretical values calculated for the five different crystallographic sites of the B atoms taking the energy barriers and prefactors obtained from DFT; (– · · –) hwhm's calculated for the $C_3$ rotations, (– – –) hwhm's calculated for the $C_{2\|}$ rotations. The shaded area represents the broadening that will give a process having typical resident times of 0.1−1 ps and $E_a$ = 100 meV.

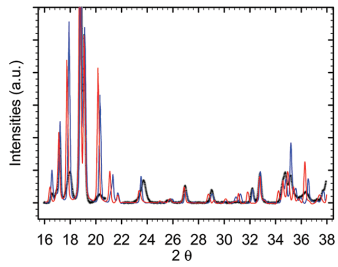


**Figure 12.** Gray line, experimental PXD pattern; red line, simulated X-ray pattern using the DFT relaxed structure; blue line, simulated X-ray pattern using the structure from ref 33.

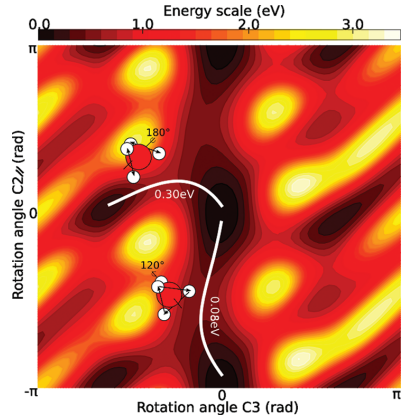


**Figure 13.** Potential energy surface for $B01H_4^-$ rigid rotations along the $C_{2\|}$- and $C_3$-axes. The marked paths represent those chosen to do the NEB calculations. Their respective NEB barrier heights are written next to each one.

where the prefactor $\Gamma_0$ is a constant, $E_a$ is the activation energy for the hindered rotation, $k_B$ is the Boltzmann constant, and $T$ the temperature. At 0 K, the activation energies equal the height of the potentials or energy barriers for hindered rotations, the contributions from the zero point energy (ZPE) being less than 20% of their magnitudes. To treat rates at final temperatures, where ZPE cannot just simply be added, the DFT calculated barrier heights are used and compared to the experimental activation energies.[56,57] Straight lines for the thermally activated rotations were obtained with the following activation energies: MARS, 39 ± 0.5 and 76 ± 5 meV; SPHERES, 214 ± 4 meV (See Table 2 and Figure 11). Figure 11 also shows the hwhm values calculated using the DFT results (see the paragraph below).

**DFT Calculations.** The calculated structural parameters for the relaxed $\beta$-$Mg(BH_4)_2$ are displayed in Table 1. The atoms coordinates and cell parameters are in good agreement with those from ref 33 and the ones obtained from the Rietveld refinement of the diffraction pattern.

Her et al. performed the refinement of the structural parameters restricting the orientation of the two $BH_4^-$ tetrahedron, with boron atoms at B03 (16g) and B05 (16e), to accommodate the $C_{2\|}$ axis. During the DFT calculations, both the orientation of the tetrahedra and the positions of the boron were free to relax. While the orientations of the tetrahedra accommodate the $C_{2\|}$-axis, all the boron atoms, including B03 and B05, move out of the Mg−Mg axis. The Mg−B−Mg angles, Mg−Mg distances, and the length ($L$) of the median of the Mg−B−Mg triangle, measuring the distance of the boron atom to the middle point of the Mg−Mg segment, can be found in Table 1. Figure 12 displays the experimental PXD pattern together with those simulated using the DFT calculated structure and those proposed by Her et al. At low angles, both patterns reproduce the experimental data. Only translation of the peak positions exist because of the different cell parameters, the ones obtained from DFT being slightly larger. Note that every $(2n + 1, 2n + 1, 2n + 1)$ simulated reflection gives a sharp peak because the antiphase boundary is not modeled due to size limitations. At high angles, the discrepancy between the two simulated patterns is more pronounced and the one obtained from Her's structure is closer to the experimental one. The discrepancy, at high angles, between the DFT calculated pattern with the other ones might be due to the overestimated local disorder of the calculated structure.

The results from the QENS experiments showed localized dynamic events expected to originate from hindered rotations of borohydride units. Using the Schönflies notation[58] there are four different types of permutations possible for a single tetrahedral borohydride group. $S_4$ axes and mirror planes can be quickly discarded, as they are not rotations but rearrangements of hydrogen atoms that are much higher in energy, due to the required formation of planar $BH_4^-$ configuration during the rearrangement. Then only various $C_2$- and $C_3$-axes remain. Since the boron positions are not equivalent, investigations of the hindered rotations using the NEB method had to be conducted for the five different positions, the three $C_2$- and four $C_3$-axes. Rapidly, the hindered rotations around the $C_{2\perp}$-axes were discarded as leading to combinations with rotation around the $C_3$-axes. For the rotation around the $C_3$-axes, only a single axis of rotation per boron atom was retained, the others giving too high energy compared with those obtained experimentally.

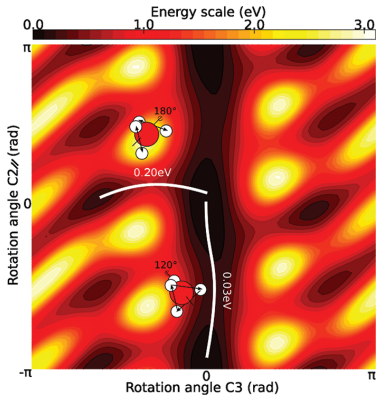


**Figure 14.** Potential energy surface for $B05H_4^-$ rigid rotations along the $C_{2||}$- and $C_3$-axes. The marked paths represent those chosen to do the NEB calculations. Their respective NEB barrier heights are written next to each one.

Figures 13 and 14 present 2D rigid rotation potential energy surfaces (PES) for two of the symmetry-inequivalent $BH_4^-$ units, B01 and B05, respectively, calculated using the $C_{2||}$-axis and a $C_3$-axis as the degrees of freedom. The starting point for the calculation is the relaxed structure, and thus, the origin of the axis represents an energy minimum. As expected from their symmetry, energy minima for the rotations around the $C_{2||}$-axis occur at $\pi$ and around the $C_3$-axis at $2\pi/3$ and $4\pi/3$. Furthermore, some intermediate minima were found, but further calculations showed that they were very shallow once fully relaxed with energy barriers of low values compared to those obtained experimentally. It can be seen from these figures that the rotations around the $C_{2||}$-axis require lower energy than the one around the $C_3$-axis, and this was true for all the inequivalent boron sites. The barrier heights calculated from the rigid rotation being higher than the barriers suggested by the experiments, NEB calculations were carried out with all the atoms in the supercell free to move. Figure 15 displays, as an example, the energy profile of these calculations for the B05 atom. A very shallow intermediate state ($4 \times 10^{-3}$ eV) is located at the top of the $C_{2||}$ rotation. NEB calculations yielded barriers and quasielastic broadenings in good quantitative agreement with those of the experiments. The different energy barriers and prefactors can be found in Table 3. Figure 11 displays, together with the experimental values, the values of the hwhm calculated for the five different crystallographic sites of the B atoms using the energy barriers and prefactors obtained from the DFT calculations and eq 9. Figure 16 shows the QENS spectra measured with SPHERES, for $Q = 1.42$ Å$^{-1}$, together with the calculated spectra consisting of the sum of the resolution function and five Lorentzian of widths calculated using the energy barriers and prefactors obtained from the DFT calculation and eq 9. On this figure, the relative intensities of the Lorentzian and resolution function were set to comply with the EISF for the $C_3$ rotation (eq 5). At $Q = 1.42$ Å$^{-1}$, EISF = 0.5 thus $I_{el} = I_{qel}$ with $I_{qel} = 1/5\Sigma_5 I_{L_i}$. Without any kind of adjustment or fitted parameters, the experimental data are fairly well described; nevertheless, the values for $\chi^2$ ranging from 4.78 to 9.75 are larger than the one obtained when performing the fits with one or two Lorentzian plus background ($\chi^2 < 2$).

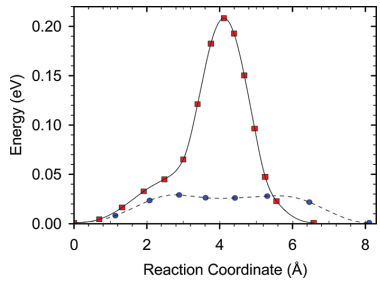


**Figure 15.** The calculated minimum energy path for the $C_{2||}$ (blue/circles) and $C_3$ (red/squares) rotations of $B05H_4^-$. Each point is an NEB image; the lines are interpolations between them using also the forces. The reaction coordinate is the additive motion of atoms in the supercell.

A linear relationship exists between the energy barriers calculated for the hindered rotation around the $C_{2||}$-axis and the distance $L$ of the boron atoms to the middle point of the Mg−Mg segments (See Figure 15). The simple correlation of $L$ with the $C_3$ barriers does not hold, so other criteria have to be taken into account.

## DISCUSSION

$\beta$-Mg($^{11}BH_4$)$_2$ presents a structure with five different crystallographically distinct $BH_4^-$ anions, so one should expect a distribution of the activation energies and rotational barriers and thus a distribution of the rotational frequencies and quasielastic broadenings. Herein the analysis of the QENS spectra was performed with a maximum of two Lorentzians for two main reasons. First, any attempt to fit the QENS spectrum with five Lorentzians, even with their relative intensities or hwhm's fixed, led to unrealistic results. Second, the quality of the outcomes, with a limited number of Lorentzians, is satisfactory not to use other models. Indeed if particular temperature dependence of the width of the quasielastic component, due to their distribution, were found, one should have considered using the formalism developed by Chahid et al.[59] for example. The method used herein leads to the overestimation of the low-frequency reorientational events with the one Lorentzian (SPHERES) or the sharper one (MARS) reproducing the main feature of the QENS spectra, i.e., the quasielastic broadening close to the resolution function while the high-frequency events are taken into account by the flat background. For that reason, the experimental values obtained for the reorientational frequencies have to be considered as semiquantitative, while the values for the activation energies should represent average values for the distribution.

The analysis of the QENS data obtained for $\beta$-Mg($^{11}BH_4$)$_2$ has shown that, within the time scale accessible by the two instruments used, two different types of thermally activated hindered rotations of the $BH_4^-$ unit were observed in the temperature range from 120 to 437 K. From the comparison of the experimental results to the DFT calculations, it is established that these rotations occur around the $C_{2||}$- and $C_3$-axes. The experimental activation energy and the DFT calculated energy barriers are in good agreement with $E_{aC_{2||}} = 39 \pm 0.5$ and $76 \pm 5$ meV determined experimentally to be compared with DFT values ranging from 28 to 82 meV and $E_{aC_3} = 214 \pm 4$ meV with DFT values ranging from 177 to 298 meV. The calculated prefactors

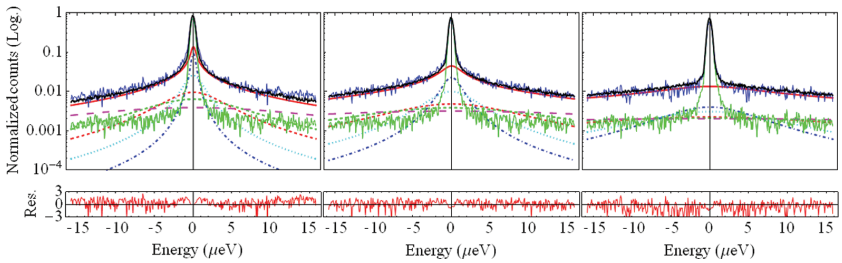


**Figure 16.** The QENS spectra of $\beta$-$Mg(BH_4)_2$ measured with SPHERES at different temperatures (from left to right, 318, 365, 437 K) for $Q = 1.42$ Å$^{-1}$. The blue lines are the experimental data. The black lines are the calculated spectra consisting of the sum of the resolution function (green lines) and five Lorentzian (dashed lines). The red lines represent the sum of the five Lorentzian. The widths of the Lorentzian are calculated using the DFT calculated energy barriers and prefactors and eq 9. The relative intensities of the Lorentzian and resolution function are set to comply with the EISF for the $C_3$ rotations (eq 5): $I_{resolution}(Q)/[I_{resolution}(Q) + 1/5\Sigma_1^5 I_{resolution}(Q)] = 1/2[1 + j_0[2(\sqrt{2}/\sqrt{3})Qd]]$. From left to right, $\chi^2 = 4.78$, 3.22, 9.75, respectively.

are somewhat smaller than the experimental values but still within the accuracy of the calculations and experiment. Together with the calculated energy barriers, good quantitative agreement with the experimental rotational frequencies at any given temperatures is obtained (see Table 3 and Figure 11). DFT calculation shows that even if all the Mg−B−Mg units are close to linear and the $BH_4^-$ have bidendate orientations corresponding to the $C_{2\|}$-axis, small variations of the distance $L$ (length of the median of the Mg−B−Mg triangle) lead to noticeable differences in the energy barriers. With MARS, two distinct values were obtained. At the lowest temperature, the observed hydrogen dynamic, treated as hindered rotation, gave that ∼15% of the hydrogen atoms are moving. This dynamic was also observed at higher temperatures, and when two Lorentzians were used, their relative intensities remained constant for all $Q$ and temperatures with a ratio of $I_{L_1}/I_{L_2} = 0.16 \pm 0.02$. An activation energy of 39 meV was found for this dynamic. When compared to the DFT results it could correspond to the rotation around the $C_{2//}$-axis of the tetrahedron with B05 as centers which account for 12.5% of the $BH_4^-$ (calculated energy barrier: 28 meV) and would give $I_{L_1}/I_{L_2} = 0.143$. This result is further supported by the agreement between the theoretical and experimental EISF, the latter being calculated by adding up the two contributions from the two Lorentzians for the evaluation of $I_{qel}$. Nevertheless and despite these proofs other arguments could be found to contradict this analysis. Second, local disorders and amorphous regions might exist at the antiphase boundary domains and it cannot be discarded that the low energy barrier events observed take place at these boundaries. Finally, the presence of $Et_2O$ in the sample has to be considered with the reorientations of the methyl and ethyl group and other vibrational modes. The activation energies for the reorientations of the methyl or ethyl group are found to be around 100 meV.[60] Taking as prefactor typical Debye−Waller frequencies of $10^{12}$−$10^{13}$ Hz leads to the shadowed area drawn in Figure 11, with no overlap with the measured quasielastic broadenings. Thus, it is unlikely that the reorientation associated with $Et_2O$ appeared in the measured QENS data; however, this cannot be strictly rejected, and measurement with a solvent-free sample should be performed to definitively answer the question.

More generally, the rotations about the $C_{2\|}$-axis were found to be energetically more favorable than those around the $C_3$-axis. This can be easily explained, as suggested in ref 20, by looking at the schematic representation of the local environment of the $BH_4^-$ tetrahedra (Figure 9). With the bidentate orientation,

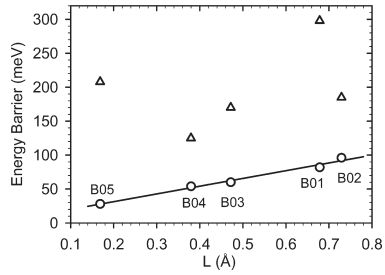


**Figure 17.** DFT calculated energy barriers for the hindered rotations versus $L$ (length of the median of the Mg−B−Mg triangle): (Δ) energy barriers for the rotations around a $C_3$-axis and (○) energy barriers for the rotations around a $C_{2\|}$-axis.

no Mg−H bond is broken during rotation around the $C_{2\|}$-axis, while the rotations around the $C_3$-axis induce two bonds breaking and the one around the $C_{2\perp}$-axis, four bond breakings.

In ref 20, the authors performed NMR measurements of the $^1H$ and $^{11}B$ spin−lattice relaxation rates in the low-temperature $\alpha$ phase of $Mg(BH_4)_2$ over the temperature range from 82 to 443 K. They observed three hydrogen dynamics with different activation energies and attributed them to reorientational motion of the $BH_4^-$ unit. The averaged activation energies associated with those three processes were $116 \pm 6$, $192 \pm 12$, and $362 \pm 5$ meV, for the fastest to the slowest process, respectively, the fastest one "being characterized by a certain distribution of activation energy". $\alpha$-$Mg(BH_4)_2$ crystallizes in the $P6_122$ space group.[61] It has six inequivalent crystallographic $BH_4^-$ groups, each surrounded by two Mg atoms in a nearly linear configuration similar to the one existing in $\beta$-$Mg(BH_4)_2$. The authors suggested that the three observed processes originate from rotations around the $C_{2\|}$-axis, inducing no bond breaking, the $C_3$-axis, with two bond breaking, and the $C_{2\perp}$-axis, with four bond breaking, the magnitude of the activation energies being correlated with the number of broken bonds.

The Mg−B and Mg−Mg distances are almost identical for the $\alpha$ and $\beta$ structures (Mg−B ∼ 2.4 Å and Mg−Mg ∼ 4.8 Å), but the distance $L$ is smaller for the $\alpha$ structure (from 0.025 to 0.16 Å) and the Mg−B−Mg angles vary from ∼147° to 170°. From the linear dependency of $E_{aC_2\|}$ with $L$, obtained from the DFT results for the $\beta$ structure (Figure 17), and with the value of $\overline{L} = 6.15 \times 10^{-2}$ Å, we obtain $E_{aC_2\|} = 15.6$ meV, which is an order of


dx.doi.org/10.1021/jp208670v | J. Phys. Chem. C 2012, 116, 2013–2023

magnitude smaller than the value 116 ± 6 meV attributed to this motion in ref 20. NMR and QENS results are consistent; see for example refs 19 and 25. Then two possible explanations exist, one being that the linear relationship found for the $\beta$ phase does not hold in the case of the $\alpha$ structure and the other being that the observed dynamics were wrongly attributed.

In order to better understand the borohydrides and more generally complex hydrides used as hydrogen storage media, more knowledge has to be gathered about their decomposition mechanisms with atomic level information on the hydrogen dynamics. In $LiBH_4$, motion of entire $BH_4^-$ units has been identified as the main mass transport mechanism above the melting temperature,[62,63] while at low temperatures a net transport of atomic hydrogen, probed by hydrogen/deuterium exchange, was also observed, although at a very low rate.[64,65] Together with hindered rotation, long-range diffusion was observed for $Ca(BH_4)_2$,[27] but this was most probably due to the presence of trapped $H_2O$ or $H_2$ in the compound. The hydrogen dynamics in $NaAlH_4$ and $Na_3AlH_6$ were also studied using quasielastic neutron scattering. One study showed only limited hydrogen vacancy diffusion, not influenced by the use of Ti additive,[23] while in another one quasielastic signal could be attributed to internal rotations and the possible combination of jumps with similar frequencies but different jump lengths.[66] This later study furthermore opens up new perspectives for time-resolved neutron backscattering studies and investigations of reaction kinetics. In other works,[25,24,26] the rotational reorientation of the $BH_4^-$ unit in $MBH_4$ (M = Na, Li, and K) was observed but no long-range diffusion. From the results presented in this study, no long-range hydrogen dynamics have been detected and only hindered rotations of the $BH_4^-$ tetrahedra were observed. Part of the measurements, not shown herein, consisted of exposing for long period of time the samples to temperatures close to the decomposition temperature (500 K), aiming at monitoring any possible long-range diffusion of hydrogen at temperatures close to the thermal decomposition of the borohydride. During this measurement, the elastic intensity decreased, a sign that more and more hydrogen moved and probably left the sample, while the quasielastic intensity remained constant basically as a flat background. Thus, if any hydrogen diffusion events occurred, they were either too fast or too slow to be probed with the instruments used herein. For further investigations of diffusion events, one should consider using spin−echo or direct geometry time-of-flight spectrometers, allowing the observations of slower and faster motions respectively and the use of different neutron energies.

The combined DFT-QENS approach has been shown to be very useful both in the interpretation of the data and to determine crucial quantities useful to develop new experiments, including the characteristic times and the energies barriers.

In the time between the acceptation for the publication of this manuscript and its proof reading, a study on in-situ neutron diffraction of the deuteration of isotopic $Mg^{11}B_2$ has been published.[67] In this study, the *Fddd* structure is retained but with slightly different positions for the D atoms when compared to the positions of the H atoms in ref 33. Furthermore, the (2n+1, 2n+2, 2n+1) broad reflections are attributed to microstructural features rather than anti-phase boundaries, and quantitative phase analysis of the isotopic sample indicated that ca. 10% of B atoms are in a non-crystalline state with the possible existence of amorphous $Mg(BD_4)_2$.

## AUTHOR INFORMATION

**Corresponding Author**
*E-mail: dibl@risoe.dtu.dk.

## ACKNOWLEDGMENT

This work is based on experiments performed at the Swiss spallation neutron source SINQ, Paul Scherrer Institute, Villigen, Switzerland, and at FRMII, JCNS Garching, Germany. It has been supported by the Danish Council for independent Research through DANSCATT. The authors acknowledge the European Graduate School for Sustainable Energy Technology and the Nordic Center for Excellence on Hydrogen Storage Materials. The Danish Center for Scientific Computing is acknowledged for supercomputer access. The Center for Atomic Materials Design (CAMD) is supported by the Lundbeck Fondation. Financial support by EU-IP NESSHY (contract #518271) and the ERA-NET project "Hy-CO" is also gratefully acknowledged.

## REFERENCES

(1) Züttel, A.; Rentsch, S.; Fischer, P.; Wenger, P.; Sudan, P.; Mauron, P.; Emmenegger, C. *J. Alloys Compd.* **2003**, *356*−*357*, 515.
(2) Nakamori, Y.; Miwa, K.; Ninomiya, A.; Li, H.; Ohba, N.; Towata, S.-I.; Züttel, A.; Orimo, S.-I. *Phys. Rev. B* **2006**, *74*, 045126-0451-9.
(3) Hummelshøj, J. S.; et al. *J. Chem. Phys.* **2009**, *131*, 014101.
(4) Miwa, K.; Aoki, M.; Noritake, T.; Ohba, N.; Nakamori, Y.; Towata, S.-I.; Züttel, A.; Orimo, S.-I. *Phys. Rev. B* **2006**, *74*, 155122–1551−5.
(5) Chong, M.; Karkamkar, A.; Autrey, T.; Orimo, S.-I.; Jalisatgid, S.; Jensen, C. M. *Chem. Commun.* **2011**, *47*, 1330.
(6) Severa, G.; Rönnebro, E.; Jensen, C. M. *Chem. Commun.* **2010**, *46*, 421.
(7) Rönnebro, E.; Majzoub, E. H. *J. Phys. Chem. B* **2007**, *111* (No. 42), 12045.
(8) Kim, J.-H.; Shim, J.-H.; Cho, Y. W. *J. Power Sources* **2008**, *181* (1), 140.
(9) Barkhordarian, G.; Jensen, T. R.; Doppiu, S.; Rösenberg, U.; Borgschulte, A.; Gremaud, R.; Cerenius, Y.; Dornheim, M.; Klassen, T.; Bormann, R. *J. Phys. Chem. C* **2008**, *112*, 2743.
(10) Lodziana, Z.; Vegge, T. *Phys. Rev. Lett.* **2006**, *97* (11), 119602.
(11) Tekin, A.; Hummelshøj, J. S.; Jacobsen, H. J.; Sveinbjörnsson, D.; Blanchard, D.; Nørskov, J. K.; Vegge, T. *Energy Envirn. Sci.* **2010**, *3*, 448.
(12) Ford, P. T.; Richards, R. *Discuss. Faraday Soc.* **1955**, No. 19, 230.
(13) Tsang, T.; Farrar, T. C. *J. Chem. Phys.* **1969**, *50* (8), 3498.
(14) King, H. F.; Hornig, D. F. *J. Chem. Phys.* **1966**, *44*, 4520.
(15) Smith, D. *J. Chem. Phys.* **1974**, *60* (3), 958.
(16) Trokiner, A.; Theveneau, H.; Papon, P. *J. Chem. Phys.* **1977**, *69* (2), 742.
(17) Tarasov, V. P.; Bakum, S. I.; Privalov, V. I.; Shamov, A. A. *Russ. J. Inorg. Chem.* **1990**, *35*, 2096.
(18) Babanova, O. A.; Soloninin, A. V.; Stepanov, A. P.; Skripov, A. V.; Filinchuk, Y. *J. Phys. Chem. C* **2010**, *114*, 3712.
(19) Skripov, A. V.; Soloninin, A. V.; Filinchuk, Y.; Chernyshov, D. *J. Phys. Chem. C* **2008**, *112*, 18701.
(20) Skripov, A. V.; Soloninin, A. V.; Babanova, O. A.; Hagemann, H.; Filinchuk, A. *J. Phys. Chem. C* **2010**, *114*, 12370.
(21) Volkov, V.; Khikmatov, M.; Mirsaidov, U.; Gabuda, S.; Kozlova, S. G. *J. Struc. Chem.* **1988**, *29* (1), 58.
(22) Butcher, F.; Łodziana, Z.; Remhof, A.; Friederichs, O.; Borgschulte, A.; Mauron, P.; Züttel, A.; Sheptyakov, D.; Barkhordarian, G.; Bormann, R.; Chlopek, K.; Fichtner, M.; Sørby, M.; Riktor, M.; Hauback, B.; Orimo, S. *J. Phys. Chem. B* **2008**, *112*, 8042.

(23) Shi, Q.; Voss, J.; Jacobsen, H. S.; Lefmann, K.; Zampomi, M.; Vegge, T. *J. Alloys Compd.* **2007**, *446*−*447*, 469.
(24) Remhof, A.; Łodziana, Z.; Butcher, F.; Martelli, P.; Pendollino, F.; Friedrichs, O.; Züttel, A.; Embs, J. P. *J. Phys. Chem. C* **2009**, *113*, 16834.
(25) Remhof, A.; Łodziana, Z.; Martelli, P.; Friedrichs, O.; Züttel, A.; Skripov, A. V.; Embs, P. J.; Strässle, T. *Phys. Rev. B* **2010**, *81*, 214304.
(26) Verdal, N.; Hartman, M. R.; Jenkins, T.; DeVries, D. J.; Rush, J. J.; Udovic, T. J. *J. Phys. Chem. C* **2010**, *114*, 10027.
(27) Blanchard, D.; Riktor, M. D.; Maronsson, J. B.; Jacobsen, H. S.; Kehres, J.; Sveinbjornsson, D.; Bardaji, E.-G.; Léon, A.; Juranyi, F.; Wuttke, J.; Hauback, B. C.; Fichtner, M.; Vegge, T. *J. Phys. Chem. C* **2011**, *114*, 479.
(28) Martelli, P.; Remhof, A.; Borgschulte, A.; Ackermann, R.; Strässle, T.; Embs, J. P.; Ernst, M.; Matsuo, M.; Orimo, S.-I.; Züttel, A. *J. Phys. Chem. A* **2011**, *115*, 5329.
(29) Tomkinson, J.; Waddington, T. C. *J. Chem. Soc. Faraday* **1976**, *72*, 528.
(30) Borgschulte, A.; Gremaud, R.; Zuttel, A.; Martelli, P.; Ramirez-Cuesta, A. J.; Refson, K.; Bardaji, E. G.; Lohstroh, W.; Fichtner, M.; Hagemann, H.; Ernst, M. *Phys. Rev. B* **2011**, *83*, 024102–024101.
(31) Bée, M. *Quasielastic Neutron Scattering*; Adam Hilger: Bristol, UK, 1988.
(32) Cerny, R.; Filinchuk, Y.; Hagemann, H.; Yvon, K. *Angew. Chem., Int. Ed.* **2007**, *46*, 5765.
(33) Her, J.-H.; Stephens, P. W.; Gao, Y.; Soloveichick, G. L.; Rijssenbeek, J.; Andrus, M.; Zhao, J.-C. *Acta Crystallogr.* **2007**, *B63*, 561.
(34) Konoplev, V. N.; Bakulina, V. M. *Bull. Acad. Sci. USSR Div. Chem. Sci. (Engl. Transl.)* **1971**, *20*, 136.
(35) George, L.; Drozd, V.; Saxena, S. K. *J. Phys. Chem. C* **2009**, *113*, 15087.
(36) Dai, B.; Sholl, D. S.; Johnson, J. K. *J. Phys. Chem. C* **2008**, *112*, 4391.
(37) Voss, J.; Hummelshøj, J. S.; Łodziana, Z.; Vegge, T. *J. Phys.: Condens. Matter* **2009**, *21*, 012203.
(38) Bil, A.; Kolb, B.; Atkinson, R.; Pettifor, D. G.; Thonhauser, T.; Kolmogorov, A. N. *Phys. Rev. B* **2011**, *83*, 224103.
(39) Yang, J.; Zhang, X.; Zheng, J.; Songa, P.; Li, X. *Scr. Mat.* **2011**, *64*, 225.
(40) Chlopeck, K.; Frommen, C.; Léon, A.; Zabara, O.; Fichtner, M. *J. Mater. Chem.* **2007**, *17*, 3496.
(41) Łodziana, Z.; Van Setten, M. *J. Phys. Rev. B* **2010**, *81* (2), 024117.
(42) Hunter, B. *IUCR Powder Diffraction Newsletter*; No. 20, 1998.
(43) Wuttke, J. *Spheres Online Manual*; http://www.jcns.info/jcns_spheres.
(44) http://sinq.web.psi.ch/sinq/instr/mars.html.
(45) Wuttke, J. *Slaw: Neutron Scattering Histograms to Scattering Law Converter*; http://www.messen-und-deuten.de/slaw.
(46) Azuah, R. T.; Kneller, L. R.; Qiu, Y.; Tregenna-Piggott, P. L. W.; Brown, C. M.; Copley, J. R. D.; Dimeo, R. M. *J. Res. Natl. Inst. Stand. Technol.* **2009**, *114*, 341.
(47) Bahn, S. R.; Jacobsen, K. W. *Comput. Sci. Eng.* **2002**, *4*, 56.
(48) Hammer, B.; Hansen, L. B.; Nørskov, J. K. *Phys. Rev. B* **1999**, No. 59, 7413.
(49) Kohn, W.; Sham, L. J. *Phys. Rev.* **1965**, *140* (4A), 1133–1138.
(50) Vanderbilt, D. *Phys. Rev. B* **1990**, *41* (11), 7892–7895.
(51) Perdew, J. P.; Chevary, J. A.; Vosko, S. H.; Jackson, K. A.; Pederson, M. R.; Singh, D. J.; Fiolhais, C. *Phys. Rev. B* **1992**, *46* (11), 6671.
(52) Liu, D. C.; Nocedal, J. *Math. Program.* **1989**, *45* (3), 503–528.
(53) Henkelman, G.; Uberuaga, B. P.; Jonsson, H. *J. Chem. Phys.* **2000**, *113* (22), 9901.
(54) Bitzek, E.; Koskinen, P.; Gähler, F.; Moseler, M.; Gumbsch, P. *Phys. Rev. Lett.* **2006**, *97* (17), 170201.
(55) Vineyard, G. H. *J. Phys. Chem. Solids* **1957**, 3 (1−2), 121–127.
(56) Ericsson, A.; Kowalewski, J. *J. Mag. Reson.* **1980**, *38*, 9.
(57) Bernassau, J. M.; Fetizon, M.; Pinheiro, J. A. *J. Phys. Chem.* **1986**, *90*, 1051.
(58) Schoenflies, A. *Math. Ann.* **1889**, *34*, 172–203.
(59) Chahid, A.; Alegría, A.; Colmenero, J. *Macromolecules* **1994**, *27*, 3282.
(60) Senent, M. L.; Ruiz, R.; Villa, M.; Domínguez-Gómez, R. *J. Chem. Phys.* **2009**, *130*, 064101.
(61) Filinchuk, Y.; Cerny, R.; Hagemann, H. *Chem. Mater.* **2009**, *21*, 925.
(62) Shane, D. T.; Bowman, R. C.; Conradi, M. S. *J. Phys. Chem. C* **2009**, *113* (42), 5039.
(63) Corey, R. L.; Shane, D. T.; Bowman, R. C.; Conradi, M. S. *J. Phys. Chem. C.* **2008**, *112* (47), 18706.
(64) Borgschulte, A.; Zuttel, A.; Hug, P.; Racu, A. M.; Schoenes, J. *J. Phys. Chem. A* **2008**, *112* (21), 4749.
(65) Gremaud, R.; Łodziana, Z.; Hug, P.; Willenberg, B.; Racu, A.-M.; Schoenes, J.; Ramirez-Cuesta, A. J.; Clark, S. J.; Refson, K.; Züttel, A.; Borgschulte, A. *Phys. Rev. B* **2009**, *80*, 100301–1001−4.
(66) Léon, A.; Wuttke, J. *J. Phys.: Condens. Matter* **2011**, *23*, 254214.
(67) Pitt, M.; Webb, C.; Paskevicius, M.; Sheptyakov, D.; Buckley, C.; Gray, E. *J. Phys. Chem. C* **2011**, *115* (45), 22669.

PCCP

Dynamic Article Links

Cite this: *Phys. Chem. Chem. Phys.*, 2012, **14**, 2884–2891

www.rsc.org/pccp

**PAPER**

# A method for finding the ridge between saddle points applied to rare event rate estimates†

**Jón Bergmann Maronsson,[a] Hannes Jónsson[b] and Tejs Vegge*[a]**

***Received 30th October 2011, Accepted 22nd December 2011***
**DOI: 10.1039/c2cp23421a**

A method is presented for finding the ridge between first order saddle points on a multidimensional surface. For atomic scale systems, such saddle points on the energy surface correspond to atomic rearrangement mechanisms. Information about the ridge can be used to test the validity of the harmonic approximation to transition state theory, in particular to verify that second order saddle points—maxima along the ridge—are high enough compared to the first order saddle points. New minima along the ridge can also be identified during the path optimisation, thereby revealing additional transition mechanisms. The method is based on a string of discretisation points along a path between the first order saddle points and using an iterative optimisation which requires only the force acting on the atoms. At each iteration during the optimisation, the force is inverted along an unstable eigenmode perpendicular to the path. The method is applied to Al adatom diffusion on the Al(100) surface to find the ridge between 2-, 3- and 4-atom concerted displacements and hop mechanisms. A correction to the harmonic approximation of transition state theory was estimated by direct evaluation of the configuration integral along the ridge.

## 1. Introduction

The rate of rare events in a system coupled to a heat bath can be estimated by evaluating the free energy barriers for the transitions. Transition state theory (TST)[1–5] is the foundation for this approach. In atomic scale systems, for example, the rate of thermally activated rearrangements of the atoms, which, typically, are several orders of magnitude slower than atomic vibrations, can be estimated from the free energy of a dividing surface separating atomic configurations corresponding to the initial state from the atomic configurations corresponding to all final states. Due to the large difference in time scale between atomic vibrations and typical thermally induced processes such as chemical reactions or diffusion, it would require immense computational power to directly simulate dynamical trajectories sufficiently long to include these rare events. TST makes it possible to focus on the rare events and neglect the details of the fast vibrational motion. It provides an approximation which eliminates the time scale problem, while dynamical information and an exact rate constant can be obtained by applying dynamical corrections based on trajectories started at the dividing surface.[6] The greatest challenge in the implementation of TST is to determine and represent a good dividing surface. The better the choice of the dividing surface, the better the estimate of the rate will be (TST gives a variational upper bound) and easier to subsequently evaluate the dynamical corrections.

Given a dividing surface (transition state), ‡, the reaction rate, $k^{\mathrm{TST}}$, out of the initial state, I, can be calculated as the thermally averaged probability of being at the transition state times the average velocity, $v_\perp$, perpendicular to the dividing surface in the direction away from the initial state

$$k^{\mathrm{TST}} = \tfrac{1}{2}\langle|v_\perp|\delta(\mathbf{R}-\mathbf{R}^\ddagger)\rangle. \quad (1)$$

A hyperplane is a commonly used choice for a dividing surface. The expression for the rate constant then becomes

$$k^{\mathrm{TST}} = \sqrt{\frac{k_\mathrm{B}T}{2\pi\mu}}\frac{Z_\ddagger}{Z_I}, \quad (2)$$

$$Z_S = \int_S \mathrm{e}^{-E(\mathbf{R})/k_\mathrm{B}T}\,\mathrm{d}\mathbf{R}. \quad (3)$$

where $Z_S$ denotes a configuration integral over a subspace $S$ in configuration space. Here, $E(\mathbf{R})$ is the energy of configuration $\mathbf{R}$, $k_\mathrm{B}$ is the Boltzmann constant, $T$ the temperature and $\mu$ the effective mass for motion along the hyperplane normal.

The task of finding and representing a transition state is simplified greatly in the harmonic approximation to TST[7,8] (HTST),

[a] *Department of Energy Conversion and Storage, Technical University of Denmark, Risø Campus, 4000 Roskilde, Denmark. E-mail: jber@risoe.dtu.dk, teve@risoe.dtu.dk*
[b] *Science Institute and Faculty of Science, VR-III, University of Iceland, 107 Reykjavík, Iceland. E-mail: hj@hi.is*
† Electronic supplementary information (ESI) available. See DOI: 10.1039/c2cp23421a

where the transition state is represented as a collection of hyperplanar segments placed at first order saddle points ($SP_1$s) on the potential energy rim surrounding the initial state and having a normal pointing along the unstable vibrational mode (see, for example ref. 9). The potential energy function is then approximated by a second order Taylor expansion around the $SP_1$s for the transition state and around the potential energy minimum at the initial state. Each saddle point represents a particular transition mechanism and the energy of the saddle point minus the energy of the initial state minimum gives the corresponding energy barrier, $E_b = E^{\ddagger} - E^{I}$. The expression for the reaction rate constant at this level of approximation becomes

$$k^{\mathrm{HTST}} = \frac{\prod_{i}^{3N} \nu_i^{\mathrm{I}}}{\prod_{i}^{3N-1} \nu_i^{\ddagger}} e^{-E_b/k_B T}, \quad (4)$$

where $N$ is the number of atoms in the system, $\nu^{\ddagger}$ denotes frequency of vibrational normal modes at the saddle point and $\nu^{I}$ at the initial state minimum. HTST is much less computationally demanding than full TST, typically by several orders of magnitude and is therefore frequently used, especially for transitions in solids. It, however, does not apply to soft matter systems where a multitude of saddle points with low energy tend to be present. It is important to identify under what conditions HTST is accurate enough and when full TST is needed.

Finding a $SP_1$ is challenging especially if the transition mechanism is not known *a priori*. Several methods have been developed for this task, which can be divided into two categories: those where knowledge about only the initial state is input and those where knowledge about both the initial and a final state is input. An example of the first category are minimum mode following methods[10,11] which involves inverting the force component along the eigenmode corresponding to the lowest eigenvalue of the Hessian matrix to locally transform $SP_1$s into minima. The latter involves finding a minimum energy path (MEP) between the two states, a path for which the component of the gradient in directions perpendicular to the path is zero and corresponding eigenvalues are positive. Any maximum along a MEP is a $SP_1$ and the highest one gives the best estimate of the energy barrier that needs to be overcome. The nudged elastic band (NEB) method[12–14] is frequently used in this context, where an initial path is discretised by images of the system which are then optimised until each image has converged onto a path with zero perpendicular gradient. Frequently, a NEB calculation finds additional minima along the MEP, thereby revealing possible states of the system that may not have been known beforehand, see for example ref. 15. A review of several $SP_1$ finding algorithms is presented in ref. 16.

Both methods mentioned above only require the evaluation of the first derivative of the energy surface, even though they are used to find points that are identified by the curvature, *i.e.* properties related to the second derivatives. It is desirable to avoid having to evaluate second derivatives because they usually require a large computational effort. In plane wave based density functional theory calculations, for example, the first derivative of the energy can be obtained without much extra computational effort beyond the potential energy, while the evaluation of the second derivatives, and thus the Hessian matrix, is much more difficult and costly.

As mentioned above, the harmonic approximation only applies to certain types of systems. The multi-dimensional parabolas need to be accurate enough approximations to the energy surface in the statistically relevant regions near the minimum and near the $SP_1$ at the temperature of interest. In particular, HTST only applies if the $SP_1$ is sufficiently higher in energy than the initial state (a commonly used rule of thumb is $E_b > 5k_BT$),[5] and sufficiently lower than surrounding second order saddle points, $SP_2$s (at an $N$th order saddle point the Hessian matrix has $N$ negative eigenvalues). Checking these criteria is non-trivial but important. If they are not met, the HTST estimate of the rate may not be satisfactory.

The presence of low energy $SP_2$s or irregularities in the potential energy ridge near $SP_1$s can be seen as warning signs that the harmonic approach is inadequate. Furthermore, a rough correction factor for the reaction rate can be evaluated by comparing the configuration integral, $Z_{\ddagger}$, with and without the harmonic approximation.

Characterizing potential energy ridges can also be useful when ensuring that all relevant $SP_1$s have been found, as the ridge between two $SP_1$s that are not adjacent on the ridge will go through any intermediate $SP_1$. This can be helpful when analysing complex systems where it is hard to predict the most efficient transition mechanism.

Finding $SP_2$s and energy ridges is inherently more difficult than finding $SP_1$s as maxima along a MEPs. As more constraints need to be applied during the optimisation, several new challenges emerge, as discussed below.

Most rigorously, the energy ridge can be identified by running steepest descent trajectories and finding the boundary between starting points in configuration space that converge to different local minima.[17] Such a procedure is, however, far too computationally tedious for all but the simplest, low dimensional systems.

In the vicinity of a $SP_1$, the Hessian matrix has one negative eigenvalue, $\lambda$, and at any point on the ridge, the gradient of the energy has no component in the direction of the corresponding eigenvector, $\hat{\boldsymbol{\varepsilon}}$,[18]

$$\hat{\boldsymbol{\varepsilon}} \cdot \nabla E = 0 \text{ and } \lambda < 0. \quad (5)$$

As discussed below, this condition does not hold near a $SP_2$, where the Hessian matrix has two negative eigenvalues.

In this article, we present a method for estimating the location of an energy ridge between two $SP_1$s, going through one or more $SP_2$s. It combines elements from the two categories of algorithms for finding $SP_1$ mentioned above. After presenting the method in the next section, we describe an application to a study of the diffusion of an Al adatom on an Al(100) surface. The results show that some of the low energy processes are not well described by the harmonic approximation even at rather low temperatures and a correction factor for HTST is estimated by evaluating the configuration integral along the ridge.

## 2. Methodology: finding the ridge

Given an energy surface, $E(\mathbf{R})$, its gradient, $\nabla E(\mathbf{R})$, and two $SP_1$s, the goal is to identify a path that lies close to the energy

ridge between the two $SP_1$s. The path should, in particular, lie through any intermediate $SP_2$ so that a comparison of the height of $SP_2$s with respect to the $SP_1$s can be made. The method should, furthermore, lead to the identification of previously unknown $SP_1$(s) on the ridge in between the given end points, should they exist.

The path is at each point characterised by its tangent, $\hat{\boldsymbol{\tau}}$. When the path lies along the ridge, the component of the gradient or, equivalently, the force, $\mathbf{F} \equiv -\nabla E(\mathbf{R})$, that is perpendicular to the tangent,

$$\mathbf{F}^{\perp} \equiv \mathbf{F} - (\mathbf{F}\cdot\hat{\boldsymbol{\tau}})\hat{\boldsymbol{\tau}}, \tag{6}$$

must vanish at each point along the path,

$$\mathbf{F}^{\perp}_{\text{ridge}} = \mathbf{0}. \tag{7}$$

For a given estimate of the path, the optimisation task involves iteratively adjusting its shape and location until $\mathbf{F}^{\perp}$ vanishes, but in order for the path to lie along a ridge rather than a MEP, it is necessary that the energy has a maximum at the path along a perpendicular direction. Close to a $SP_1$, this direction is given by the eigenmode corresponding to the smallest eigenvalue of the Hessian matrix as illustrated in Fig. 1. Close to a $SP_2$, however, the Hessian matrix has two negative eigenvalues and the eigenmode corresponding to the lower one may be parallel to the tangent of the ridge and the direction at which a point on the ridge is a maximum corresponding to the second lowest eigenvalue. This is also illustrated in Fig. 1. There can, furthermore, be regions where neither of the two eigenmodes corresponding to negative eigenvalues are perpendicular to the tangent of the ridge as seen in Fig. 1. The latter regions can pose significant stability issues during the optimisation if not properly constrained.

The reduced Hessian matrix for the subspace excluding the tangent vector has at each point on the ridge one and only one negative eigenvalue whose corresponding eigenmode, $\hat{\boldsymbol{\varepsilon}}$, is necessarily orthogonal to the ridge. The ridge can be located by maximizing the energy along this direction while minimizing in all other directions perpendicular to the ridge. By transforming the force, $\mathbf{F}^{\perp}$, in such a way that it locally, near the ridge, corresponds to that of a MEP

$$\mathbf{F}^{\text{t}} = \mathbf{F}^{\perp} - 2(\mathbf{F}^{\perp}\cdot\hat{\boldsymbol{\varepsilon}})\hat{\boldsymbol{\varepsilon}}, \tag{8}$$

an iterative displacement of the path in the direction of $\mathbf{F}^{\text{t}}$, *i.e.* a minimisation, can be used to locate the ridge. This mapping of the force makes it possible to employ a method that is similar to a NEB search for a MEP, but by using the transformed force, $\mathbf{F}^{\text{t}}$, the path converges on a ridge instead.

A numerical implementation of the path optimisation requires the introduction of discretisation. The path is represented by a discrete set of configurations, a set of images of the system, with coordinates $[\mathbf{R}_0, \mathbf{R}_1, \ldots, \mathbf{R}_{N-1}, \mathbf{R}_N]$. The energy of each image, $i$, is $E_i \equiv E(\mathbf{R}_i)$. Since a discrete representation of the path is used, the path's tangent needs to be approximated at each image. In NEB calculations, it has been found to be important, for numerical stability, to use the vector displacement to the higher energy neighbouring image, so as to minimise the formation of kinks in the path.[14] This same tangent estimation was used in the calculations presented here.

In order to perform the force transformation described in eqn (8), it is necessary to be able to find the eigenmode associated with the lowest eigenvalue (hereafter referred to as the minimum mode) of the reduced Hessian matrix. For this purpose we use the dimer method[10,11] since it gives the minimum mode using only the force as input. It is also possible to use the Lanczos method for this purpose.[11] For clarity, we rewrite eqn (8) for each image, $i$

$$\mathbf{F}^{\text{t}}_i = \mathbf{F}^{\perp}_i - 2(\mathbf{F}^{\perp}_i\cdot\hat{\boldsymbol{\varepsilon}}_i)\hat{\boldsymbol{\varepsilon}}_i, \tag{9}$$

which is applied after the dimer has been rotated subject to a constraint $\hat{\boldsymbol{\varepsilon}}_i\cdot\hat{\boldsymbol{\tau}}_i = 0$, to find the minimum mode of the reduced Hessian matrix.

In order to ensure an even distribution of the images along the path, a spring force, $\mathbf{F}^{\text{S}}_i$, between adjacent images is introduced. The force exerted on image $i$ by the springs is

$$\mathbf{F}^{\text{S}}_i = k[(\mathbf{R}_{i+1} - \mathbf{R}_i) - (\mathbf{R}_i - \mathbf{R}_{i-1})], \tag{10}$$

where $k$ is the spring constant which can be chosen to fit the energy landscape. For numerical convergence, it is best to choose $k$ in such a way that the spring force is of roughly the same magnitude as the force derived from the energy surface, but a wide range of values can be used. Here, the same value of $k$ is used for all pairs of adjacent images, but unequal values can be chosen if an unequal distribution of the images along the ridge is desired, analogous to NEB calculations.[13]

The effective force, $\mathbf{F}^{\text{eff}}_i$, acting on each image can now be written as

$$\mathbf{F}^{\text{eff}}_i = \mathbf{F}^{\text{t}}_i + \mathbf{F}^{\text{S}}_i, \tag{11}$$

where the first term is the transformed force from eqn (9) and the second term is the spring force from eqn (10) that controls the distribution of the images along the path and increases

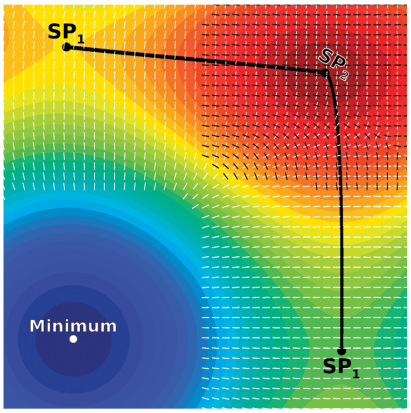


**Fig. 1** A schematic, two-dimensional, energy surface illustrating an energy ridge between two $SP_1$s through a $SP_2$. The ridge is shown with a black line, which is the dividing surface between starting points of steepest descent paths that lead to different minima (only one of the minima is shown). The directions of eigenmodes corresponding to negative eigenvalues of the Hessian matrix are shown with short line segments, white indicating the one corresponding to the lower eigenvalue and the black corresponding to the higher one.

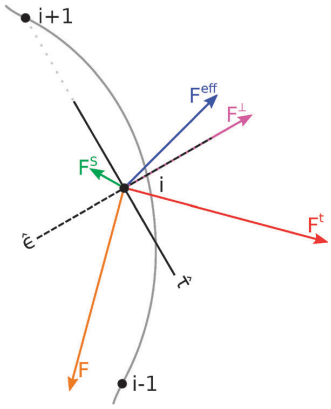


**Fig. 2** The construction of the effective force, $\mathbf{F}^{\mathrm{eff}}$, which acts on image $i$ of the path and is used in the iterative optimisation. The solid grey line indicates the ridge, the black filled circles represent the current location of three adjacent images, the black solid line shows the tangent estimate, $\hat{\boldsymbol{\tau}}$ and the black dashed line shows the minimum mode estimate, $\hat{\boldsymbol{\varepsilon}}$, at image $i$. The orange arrow shows the original force, $\mathbf{F} = -\nabla E$. The red arrow shows the transformed force, $\mathbf{F}^{\mathrm{t}}$, obtained by inverting $\mathbf{F}$ in the direction of the minimum mode, $\hat{\boldsymbol{\varepsilon}}$ (see eqn (9)). The purple arrow shows $\mathbf{F}^{\perp}$, the component of the transformed force that is perpendicular to the tangent. The green arrow shows $\mathbf{F}^{\mathrm{S}}$, the spring force given by eqn (10). The blue arrow shows $\mathbf{F}^{\mathrm{eff}}$, as given by eqn (11).

numerical stability. The construction of the effective force is illustrated in Fig. 2.

If the ridge is curved, the spring force tends to shorten the path by allowing the component perpendicular to the path to pull it off the ridge. The position of the images, then, converges to an equilibrium between the components of the spring force and the transformed force, that are perpendicular to the tangent,

$$\mathbf{F}_i^{\mathrm{t}} - (\mathbf{F}_i^{\mathrm{t}}\cdot\hat{\boldsymbol{\tau}}_i)\hat{\boldsymbol{\tau}}_i = -(\mathbf{F}_i^{\mathrm{S}} - (\mathbf{F}_i^{\mathrm{S}}\cdot\hat{\boldsymbol{\tau}}_i)\hat{\boldsymbol{\tau}}_i). \qquad (12)$$

This equilibrium position will systematically be slightly of the ridge. Equivalently, this is referred to as corner-cutting (see, for example ref. 12). The perpendicular component of the spring force can be projected out, as is often done in the NEB method, but here it is retained in order to improve the stability of the iterative optimisation.

The climbing image algorithm[13] can be used on the highest energy image of the path to ensure exact convergence to the highest energy $\mathrm{SP}_2$ along the ridge. This is accomplished by decoupling the highest energy image from the springs and inverting the force along the tangent and the minimum mode in a manner similar to eqn (9),

$$\mathbf{F}_{i_{\max}}^{\mathrm{eff}} = \mathbf{F}_{i_{\max}} - 2(\mathbf{F}_{i_{\max}}\cdot\hat{\boldsymbol{\tau}}_{i_{\max}})\hat{\boldsymbol{\tau}}_{i_{\max}} - 2(\mathbf{F}_{i_{\max}}\cdot\hat{\boldsymbol{\varepsilon}}_{i_{\max}})\hat{\boldsymbol{\varepsilon}}_{i_{\max}}, \quad (13)$$

where $i_{\max}$ refers to the image with the highest energy. This decoupling achieves two things. It allows the highest energy image to converge onto the $\mathrm{SP}_2$ exactly without significant increase in computational power and it allows the highest energy image to be decoupled from the spring force which, in turn, will allow it to overcome any tendency for corner-cutting.

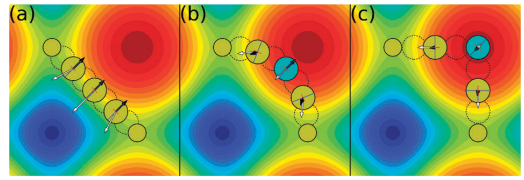


**Fig. 3** Snapshots from an optimisation of a path between two neighbouring adatom hop $\mathrm{SP}_1$s on a 2 × 2 × 1 Al(100) slab. An animation is included in the ESI.† For simplicity, the Al atoms in the slab are kept fixed in this illustrative test problem. The energy surface is generated by minimizing the energy of the adatom along the normal to the surface plane but keeping the in-plane coordinates fixed. The circles represent images of the path. The cyan circle is the climbing image. For clarity, less information is shown for the dotted circles. The arrows represent the in-plane force acting on each image. (white) The force derived from the energy surface, $-\nabla E$. (black) The effective force, given by eqn (11) or (13), which is used in the iterative optimisation. The red lines represent the tangent and the blue lines represent the minimum mode estimate. The red areas of the surface represent high potential energy and the blue areas low potential energy. The immobile substrate atoms are located at the centre of the high potential areas. (a) Initial, straight line interpolation between the $\mathrm{SP}_1$s, (b) after 19 optimisation steps, converged to 0.05 eV $\mathrm{\AA}^{-1}$, without climbing image, (c) after 70 steps, converged to 0.001 eV $\mathrm{\AA}^{-1}$ with the climbing image algorithm.

The ridge calculations are different from MEP calculations in that the energy may not have a maximum along the path during the optimisation. The variation of the energy along the path can be monotonic or even an inverted barrier, *e.g.* when the initial path lies close to a minimum. This can lead to instability in the iterative optimisation and in order to increase the stability, the full spring force is used. Furthermore, complications can arise when turning on the climbing image algorithm as either of the immobile end points might, in fact, have the highest energy. In such cases it may prove beneficial for convergence to assign an image that is not the highest energy one as the climbing image. The images closest to the end images are partially constrained by the immobility of the end images, thus an image even further in, $\mathbf{R}_2$ or $\mathbf{R}_{N-2}$, is a better choice for the climbing image. When the path is near the ridge, the energy will have a maximum along the path and the highest energy image can be used as the climbing image. The lack of an intrinsic barrier makes climbing image ridge calculations risky to run from the initial interpolation. It is, therefore, better to, first, carry out enough iterations without the climbing image for an energy maximum to appear along the path and then turn on the climbing image (Fig. 3).

The method described here has been implemented and tested using the Atomic Simulation Environment (ASE)[19,20] using both analytical potential energy functions and density functional theory (DFT) to evaluate the atomic force.

## 3. Application: Al adatom diffusion on an Al(100) surface

An Al adatom on the Al(100) surface provides an interesting system to study because several different diffusion mechanisms have been found, including various concerted displacements of

two or more atoms, in addition to the, more intuitive, hop mechanism.[10,21,22] An embedded atom method potential (EAM)[23] is used here since it has been shown to accurately describe the system and requires much less computational effort than DFT calculations. The simulated cell was a slab of 6 layers, each of which was 8 × 8 atoms, with one adatom, totalling 385 atoms. The two bottom layers were kept fixed at bulk positions with a lattice parameter of 4.038 Å. Initially, traditional NEB calculations were carried out to find the relevant $SP_1$s which were then used as end points in the ridge calculations. The spring constant was set at $k = 5.0$ eV Å$^{-1}$. The two images in the dimer had a fixed separation of 0.0001 Å and were allowed to rotate only once for each iteration in the path optimisation. The initial minimum mode guesses were taken from a Gaussian distribution. The convergence criteria for the maximum effective force component were set at 0.01 eV Å$^{-1}$ and 0.001 eV Å$^{-1}$ for the regular and climbing image calculations respectively. The FIRE algorithm[24] was used for the path optimisation.

Several low energy transition mechanisms for adatom diffusion on this surface have been found previously using the dimer method.[10] The mechanism with the lowest energy barrier is a two atoms concerted displacement, $E_b = 0.227$ eV. The second lowest is the simple hop of the adatom from one site to an adjacent site, $E_b = 0.372$ eV, but then three and four atoms concerted displacements are only slightly higher in energy $E_b = 0.426$ eV and $E_b = 0.413$ eV.

The potential energy ridges and $SP_2$s were calculated between each pair of $SP_1$s and the results are shown in Fig. 4 for the three concerted displacement mechanisms. Low energy $SP_2$s were found near the concerted 3- and 4-atom displacement $SP_1$s, with energies ~0.005 eV and ~0.012 eV. The energy of these $SP_2$s is less than thermal energy at room temperature, $k_BT = 0.025$ eV, over the adjacent $SP_1$s, which means that HTST is likely not a good approximation for these mechanisms.

In principle, knowledge of the ridge and the $SP_2$s can be used to improve on the HTST approximation. Here, a rough estimate of a correction factor, $\Gamma$, will be evaluated by calculating the ratio of the configuration integrals of the harmonic approximation to that calculated from the potential energy along the ridge,

$$\Gamma = \frac{Z_{\ddagger}^{\text{ridge}}}{Z_{\ddagger}^{\text{harm.}}} = \frac{\int_{\text{ridge}} \exp[-E(x)/k_BT]\,dx}{\int_{-\infty}^{\infty} \exp[-\alpha x^2/k_BT]\,dx}, \qquad (14)$$

where $x$ is the displacement along the ridge and $\alpha$ is the curvature of the one-dimensional parabola obtained by performing least squares analysis of the 4 images closest to the $SP_1$s. The ratios obtained with eqn (14) are shown as a function of temperature in Fig. 5. As expected, the harmonic approximation works well for the concerted 2-atom process as the $SP_1$ is much lower in energy than the adjacent $SP_2$s in that case. On the other hand the concerted 3- and 4-atom displacements have a significant correction factor (~0.5 for the concerted 4-atom process at 350 K) as can be seen from the figure. It should be noted that the ratio increases with temperature due to the limited range of the ridge integral as compared with the infinite limits of the harmonic one. This is particularly

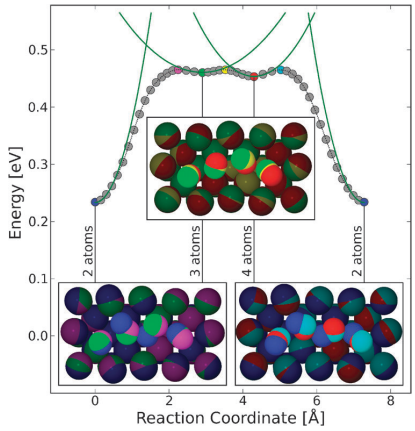


**Fig. 4** The energy ridge going through the $SP_1$s of 2-atom, 3-atom, 4-atom and, then the same, 2-atom concerted displacement for an Al adatom on an Al(100) surface. The circles represent the position of images in the optimised paths, the $SP_1$s and the $SP_2$s being coloured differently but the rest coloured grey. The green curves represent harmonic approximations to the energy surface at each $SP_1$. The insets show an overlay of three configurations, two adjacent $SP_1$s and the intermediate $SP_2$. The atom colours correspond to the coloured circles of the energy ridge. The $SP_2$s adjacent to the 3-atom and 4-atom concerted displacements are low and the harmonic approximation to TST is less accurate for these mechanisms than the 2-atom concerted displacement.

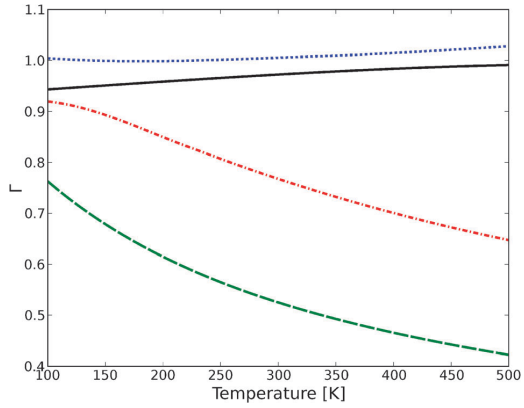


**Fig. 5** The ratio, $\Gamma$, defined in eqn (14), between the configuration integrals of the potential energy ridge shown in Fig. 4 and the corresponding harmonic approximations. The black, solid, line is the ratio for the full integral, including all three concerted displacement processes. The blue, dotted, line is the ratio when only considering the 2-atom concerted displacement. The green, dashed, line is the ratio when only considering the 3-atom concerted displacement. The red, dash-dotted, line is the ratio when only considering the 4-atom concerted displacement. For the individual processes, the end points of the ridge integral are the adjacent $SP_2$s, while the full integral is done for the whole ridge. While the harmonic approximation gives a good approximation for the total configuration integral over the whole temperature range shown, because it is dominated by the 2-atom displacement, the estimate for each of the 3-atom and 4-atom displacements is poor unless the temperature is very low.

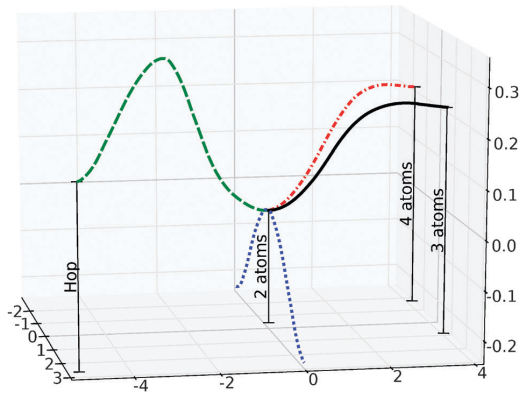


**Fig. 6** A schematic view (due to the high dimensionality of the system) of some of the ridges lying through the $SP_1$ for 2-atom concerted displacement (the MEP is shown with blue dotted line). The three ridges shown connect to the $SP_1$s of the hop and the 2-atom and 3-atom displacement mechanisms. The vertical bars represent the height of each of the $SP_1$s. The figure illustrates that a $SP_1$ typically lies on several energy ridges for a complex system.

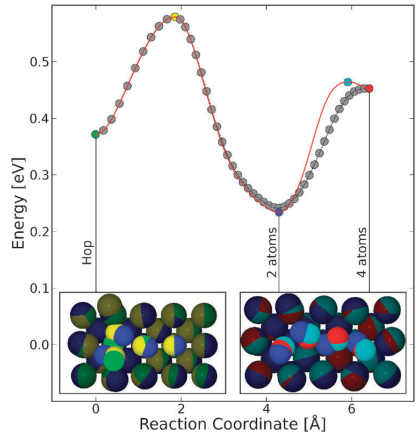


**Fig. 7** Calculated path at the ridge between the $SP_1$s for a hop and concerted 4-atom displacement. The circles show the position of converged images (coloured circles for $SP_1$s and $SP_2$s, but gray for the rest). These $SP_1$s turned out not to be adjacent on a ridge and the path optimisation reveals an intermediate $SP_1$, the one for the concerted 2-atom displacement. This illustrates how a ridge calculation could reveal new and possibly unknown transition mechanisms. The long path is not able to accurately locate the intermediate $SP_1$ and the lower energy $SP_2$ due to finite resolution in the discretisation and corner-cutting. The exact configuration of the $SP_1$ can be found using a $SP_1$ finding algorithm starting with the approximation obtained from the optimised path. Then, a calculation of a shorter path, between the $SP_1$s of the 2-atom and 4-atom displacements, locates the intermediate $SP_2$ accurately (cyan circle). The insets show an overlay of three configurations, two adjacent $SP_1$s and the intermediate $SP_2$. The atom colours correspond to the coloured circles of the energy ridge.

prominent for the 2-atom concerted displacement where the ratio even goes above 1.0. In high dimensional systems, $SP_1$s lie on multiple ridges, as can be seen in Fig. 6, where 3 of the different ridges in which the concerted 2-atom displacement $SP_1$ lies on, are shown. Thus it may be necessary to perform corrections such as those above for more than one ridge for any given $SP_1$.

In the insets of Fig. 4, a comparison of the atom coordinates at two adjacent $SP_1$ and the intermediate $SP_2$ can be seen. In particular, the difference between the concerted 3- and 4-atom $SP_1$s is shown. The coordinates of the two left-most atoms only change slightly while the two right-most coordinates change more, as is to be expected as the atom furthest to the right is not directly involved in the concerted 3-atom process. The similarities in coordinates and the small $SP_2$s separating the 3- and 4-atom displacement processes indicate that a trajectory passing through the vicinity of either $SP_1$ could easily end up in the product state corresponding to the other. Dynamical trajectories started at the ridge would be needed to determine the probability of each of the product states.

When finding the ridge between the concerted 4-atom displacement and the hop $SP_1$s, shown in Fig. 7, it became apparent that a ridge does not directly connect the two. Instead, the ridge passes through the concerted 2-atom displacement $SP_1$. The path passes exactly through the highest $SP_2$, as can be verified from the calculated force, given that the climbing image algorithm is employed. However, due to the possible corner cutting, there is no guarantee that other, lower energy, $SP_2$s along the ridge will be found exactly. Nevertheless, if a sufficient number of images is used, the path will give good approximation for any $SP_1$ and $SP_2$ along the ridge. Here, the image closest to the concerted 2-atom displacement $SP_1$ is found to be at a distance of 0.004 Å per atom from the exact $SP_1$. Using these coordinates in a $SP_1$ searching algorithm quickly yields the exact $SP_1$. As for the lower $SP_2$, a second ridge calculation can be performed with the adjacent $SP_1$s as endpoints to focus on a shorter segment of the ridge with only one intermediate $SP_2$, thereby enabling the climbing image to converge exactly on the lower $SP_2$. This is shown in Fig. 7, where the discovered $SP_1$ is used as an endpoint in a subsequent optimisation of a shorter path and, thus, the lower $SP_2$ is found accurately.

### 3.1. Performance

Convergence depends on a number of factors; the accuracy of the forces, the number of atoms in the system, the number of images in the calculation and the algorithm used for optimisation. Furthermore, the specific parameters of the minimum mode algorithm, the stiffness of the springs and the criterion for non-climbing image convergence influence the ridge convergence. Although no comprehensive convergence study for the plethora of parameters was performed, Table 1 shows convergence data for the processes presented here. In order to avoid any spurious complication during the path optimisation, the simple, but robust, FIRE algorithm[24] was used to converge each 29 image path until the maximum effective force component was smaller than 0.01 eV $Å^{-1}$ and 0.001 eV $Å^{-1}$ for the regular and climbing image calculations respectively. The spring constant was set at 5.0 eV $Å^{-1}$ and the dimer was allowed to rotate only once per optimisation step.

**Table 1** Performance of ridge calculations. The average number of optimisation steps, force calculations and a comparison with the NEB calculations of the endpoints (and corresponding MEPs), of 50 path optimisations for each of the concerted multiple atom diffusion mechanisms using 29 images. Where applicable the exact same parameters were used for both the MEP and ridge calculations. It should be noted that the $SP_2$ is generally found much faster than the ridge in full

| | Optimisation steps | | Force evaluations | |
|---|---|---|---|---|
| Diffusion mechanism | Ridge | Ridge/MEP | Ridge | Ridge/MEP |
| Concerted 2 ↔ 3 atom | 398 | 2.5 | 23 456 | 5.5 |
| Concerted 2 ↔ 4 atom | 400 | 2.5 | 23 558 | 5.4 |
| Concerted 3 ↔ 4 atom | 132 | 0.8 | 6709 | 1.6 |

The concerted 3 and 4 atom mechanisms are rather hard for the NEB to find as they correspond to shallow minima along the energy ridge. As a result, the ridge calculations can take fewer optimisation steps than the corresponding NEB calculations. On the other hand, ridge calculations have difficulty in converging the paths which have a $SP_2$ close to one $SP_1$ but far from the other, such as the ridges between the concerted 2 and 3 and concerted 2 and 4 atom mechanisms. Near these $SP_2$s, the dimer will sometimes find a soft eigenmode, *e.g.* rearrangements of the full system, which can result in failed optimisations or ones that are not useful.

A general comparison of the efficiency of NEB and ridge calculations is not feasible as the methods are used for different types of paths. The data in Table 1, nevertheless, give some indication of the resources required to perform a ridge calculation.

## 4. Summary

A method for finding an energy ridge and second order saddle points between first order saddle points is presented and used to assess the applicability of the harmonic approximation to transition state theory in a test system involving the diffusion of an Al adatom on an Al(100) surface. The method is based on locally transforming the gradient near an energy ridge to that of a MEP using an inversion of the gradient along the direction of the minimum mode perpendicular to the path. The method can be regarded as an extension of the nudged elastic band method to find an energy ridge instead of a MEP.

The application of the method to an Al adatom diffusion on an Al(100) surface shows that the harmonic approximation can be expected to perform well over a wide range of temperature for the lowest energy process, the concerted 2-atom displacement. On the other hand, for the 3-atom and 4-atom concerted displacement mechanisms, the harmonic approximation is not accurate because the $SP_2$s adjacent to the $SP_1$s for these processes are comparatively low in energy. After the energy ridge has been located, it is possible to estimate a correction factor for the reaction rate given by HTST by comparing the configuration integrals of the ridge and the harmonic approximations. Finally, calculation of the ridge between $SP_1$s that are not adjacent can reveal additional, intermediate, $SP_1$s on the ridge. This can be useful when dealing with complicated energy landscapes.

In the implementation described here, we have included the full spring force that distributes images along the path in order to improve stability of the optimisation. This can lead to corner-cutting in the path where it does not follow the ridge exactly. However, by using the climbing image algorithm, an exact convergence to the highest $SP_2$ can be ensured.

The ability to identify energy ridges and second order saddle points could become a valuable tool in computational materials design. One example is the study of catalytic selectivity in heterogeneous or electro-catalytic processes such as methane *vs.* higher alcohol formation in electrochemical $CO_2$ fixation[25] or ammonia *vs.* hydrogen formation in electrochemical $N_2$ fixation.[26] The method could, thereby, help estimate Faradaic losses in electrochemical processes.

While the discussion here has focused on a classical, over-the-barrier description of the transition mechanism, similar considerations can apply to transitions where quantum mechanical tunnelling takes place. A harmonic quantum transition state theory can be applied in such cases (see for example ref. 27–29) and similar considerations about the height of $SP_2$s over $SP_1$s on an extended, quantum mechanical energy surface, describing the energy of closed Feynman paths, may apply. The energy ridge of the extended energy surface could in principle be found by an extension of the method presented here.

Even though the main focus here is on the application to rate theory and atomic simulations, the method can be used to find ridges and $SP_2$s for any function of multiple variables where the first derivative is readily available. In fact, the method can easily be extended to find saddle points of order $N$, $SP_N$s, by ensuring that there are $N - 1$ negative eigenvalues for the reduced Hessian. This can be accomplished by having $N - 1$ constrained eigenmode searchers perpendicular to each other and the tangent of the path and applying eqn (8) to each one.

## Acknowledgements

The authors would like to acknowledge support from the European Graduate School on Sustainable Energy Technology, the Icelandic Science Foundation and Danish Center for Scientific Computing for supercomputer access. The Center for Atomic Scale Material Design (CAMD) is funded by the Lundbeck foundation and the Catalysis for Sustainable Energy (CASE) initiative is funded by the Danish Ministry of Science, Technology and Innovation.

## References

1 E. Wigner, *Trans. Faraday Soc*., 1938, **34**, 29.
2 H. Eyring, *J. Chem. Phys*., 1935, **3**, 107.
3 M. G. Evans and M. Polanyi, *Trans. Faraday Soc*., 1935, **31**, 875.
4 P. Hänggi, P. Talkner and M. Borkovec, *Rev. Mod. Phys*., 1990, **62**, 251.
5 E. Pollack and P. Talkner, *Chaos*, 2005, **15**, 026116.
6 J. C. Keck, *J. Chem. Phys*., 1967, **13**, 85.
7 C. Wert and C. Zener, *Phys. Rev*., 1949, **76**, 1169.
8 G. H. Vineyard, *J. Phys. Chem. Solids*, 1957, **3**, 121.
9 H. Jónsson, *Proc. Natl. Acad. Sci. U. S. A*., 2011, **108**, 944.
10 G. Henkelman and H. Jónsson, *J. Chem. Phys*., 1999, **111**, 7010.
11 R. A. Olsen, G. J. Kroes, G. Henkelman, A. Arnaldsson and H. Jónsson, *J. Chem. Phys*., 2004, **121**, 9776.
12 H. Jónsson, G. Mills and K. W. Jacobsen, in *Classical and Quantum Dynamics in Condensed Phase Simulations*, ed. B. J. Berne, G. Ciccotti and D. F. Coker, World Scientific, 1998, p. 385.

 

13 G. Henkelman, B. P. Uberuaga and H. Jónsson, *J. Chem. Phys.*, 2000, **113**, 9901.
14 G. Henkelman and H. Jónsson, *J. Chem. Phys.*, 2000, **113**, 9978.
15 G. Henkelman, A. Arnaldsson and H. Jónsson, *J. Chem. Phys.*, 2006, **124**, 044706.
16 G. Henkelman, G. Jóhannesson and H. Jónsson, in *Theoretical Methods in Condensed Phase Chemistry*, vol. 5 *Progress in Theoretical Chemistry and Physics*, ed. Steven D. Schwartz, Springer, Netherlands, 2002, p. 269.
17 J.-Q. Sun and K. Ruedenberg, *J. Chem. Phys.*, 1993, **98**, 9707.
18 E. M. Sevick, A. T. Bell and D. N. Theodorou, *J. Chem. Phys.*, 1993, **98**, 3196.
19 S. R. Bahn and K. W. Jacobsen, *Comput. Sci. Eng.*, 2002, **4**, 56.
20 https://wiki.fysik.dtu.dk/ase.
21 P. J. Feibelman, *Phys. Rev. Lett.*, 1990, **65**, 729.
22 G. Jóhannesson and H. Jónsson, *J. Chem. Phys.*, 2001, **115**, 9644.
23 A. F. Voter and S. P. Chen, *MRS Proceedings of 'Symposium I Characterization of Defects in Materials'*, 1986, **82**, 175.
24 E. Bitzek, P. Koskinen, F. Gähler, M. Moseler and P. Gumbsch, *Phys. Rev. Lett.*, 2006, **97**, 170201.
25 A. Peterson, F. Abild-Pedersen, F. Studt, J. Rossmeisl and J. Nørskov, *Energy Environ. Sci.*, 2010, **3**, 1311.
26 E. Skúlason, T. Bligaard, S. Gumundsdóttir, F. Studt, J. Rossmeisl, F. Abild-Pedersen, T. Vegge, H. Jónsson and J. K. Nørskov, *Phys. Chem. Chem. Phys.*, 2012, **14**, 1235–1245.
27 S. Andersson, G. Nyman, A. Arnaldsson, U. Manthe and H. Jónsson, *J. Phys. Chem. A*, 2009, **113**, 4468.
28 G. Mills, G. K. Schenter, D. Makarov and H. Jónsson, *Chem. Phys. Lett.*, 1997, **278**, 91.
29 G. Mills, G. K. Schenter, D. Makarov and H. Jónsson, *RAW Quantum Transition State Theory*, in *Classical and Quantum Dynamics in Condensed Phase Simulations*, ed. B. J. Berne, G. Ciccotti and D. F. Coker, World Scientific, 1998, p. 405.